1966

Pulse height and transient response of semiconductor radiation detectors to fission fragments.

Krulisch, Alan H.

Princeton University

http://hdl.handle.net/10945/9619

PULSE HEIGHT AND TRANSIENT RESPONSE OF SEMICONDUCTOR RADIATION DETECTORS TO FISSION FRAGMENTS

Alan H. Krulisch

DEI SUB NUMINE VIGET

VET. TES MEN NOV. TA TUM

PRINCETON UNIVERSITY

PULSE HEIGHT AND TRANSIENT RESPONSE OF SEMICONDUCTOR RADIATION DETECTORS TO FISSION FRAGMENTS

Alan H. Krulisch

A DISSERTATION
PRESENTED TO THE
FACULTY OF PRINCETON UNIVERSITY
IN CANDIDACY FOR THE DEGREE
OF DOCTOR OF PHILOSOPHY

RECOMMENDED FOR ACCEPTANCE BY THE
DEPARTMENT OF
ELECTRICAL ENGINEERING

December, 1966

ABSTRACT

The pulse height response of silicon surface barrier detectors was measured as a function of energy for median light and heavy fission fragments of Cf^{252} over an energy range of $100 \geq E \geq 7$MeV. The results demonstrated that the calibration procedure proposed by Schmitt, et al for undegraded fission fragments is actually valid over an energy range of $100 \geq E \geq 25$ MeV. Comparison of the pulse height response to fission fragments with the response to alpha particles yielded the pulse height defect as a function of energy. The magnitude and shape of the curve were found to be in disagreement with a calculation by Haines and Whitehead based on the unified range theory of Lindhard and co-workers.

The transient response of silicon surface barrier detectors was measured as a function of the energy of incident Cf^{252} fission fragments. The effect of the plasma formed by the incident fission fragment on the collection time was determined. The time to disperse the plasma was found to be proportional to $E^{1/m}$ where $2 \leq m \leq 3$ and E is the incident particle energy. A simple model was proposed for the plasma effect and found to give agreement with experiment.

ACKNOWLEDGMENTS

The author owes sincere thanks to Professor R. C. Axtmann for guidance and support extended to this project and to Professor F. K. Manasse for his encouragement and valuable suggestions.

Thanks are also due to Professor T. D.Thomas who made it all possible by lending the Cf^{252} sources, to Mr. W. McKee who aided with design and construction of the counting cell, to Dr. P. Mulás who left behind a vacuum system and to Mr. R. Persing and Mr. R. Whitley who aided in tuning up the electronic system.

Grateful acknowledgment is made of the financial assistance provided by the U.S. Atomic Energy Commission (Contract AT - (30-1) - 2807). A National Science Foundation Grant (GP - 579) to the Computer Center of Princeton University made available an IBM 7094 computer for data analysis.

The author also acknowledges the patient and total support of the United States Navy over the period of this work. Many thanks to the author's friends at the N.S.AC. who added vigor to the daily routine.

TABLE OF CONTENTS

	Page
I. INTRODUCTION	1
II. EXPERIMENTAL	6
A. Apparatus	6
1. Counting Cell and Vacuum System	6
2. The Detectors	9
3. Electronic System	10
(a) Time-of-Flight	10
(b) Pulse Height	14
(c) Linearity	14
(d) Rise Time	18
4. Radioactive Sources	28
5. "Mylar" Absorbers	29
B. Experimental Considerations	30
1. Radiation Damage	30
(a) Time-of-Flight and Pulse Height Observations	30
(b) Rise Time Observations	31
2. Source - Detector Alignment	32
3. Collimation	32
4. Miscellaneous	32
C. Preliminary Measurements and Adjustments	34
1. Energy Loss Within the Source	34
2. System Linearity	35

Page

3. Standardization of the Time Scale 39

4. Setting the Single Channel Analyzer 44

5. Alpha Calibration 47

6. Schmitt Calibration 47

7. Saturation Curves 48

8. Timing System Trigger Shift 48

9. Calibration of Absorbers for Rise Time Observations 52

D. Procedure 61

1. Detector Calibration 61

(a) Pulse Height Observations 61

(b) Time-of-Flight Observations 64

2. Rise Time Observations 65

III. RESULTS AND ANALYSIS 67

A. Pulse Height and Time-of-Flight 67

1. Analysis of Data 67

2. Average Mass Approximation 72

3. Results 78

B. Rise Time 85

1. Analysis of Data 85

2. Calculations 95

3. Results 97

IV. DISCUSSION AND CONCLUSIONS 113

A. Pulse Height 113

B. Rise Time 120

APPENDIX A. A Model for the Plasma Effect 124

LIST OF FIGURES

		Page
Fig. 1	Counting Cell and Shutter	7
Fig. 2	Vacuum System	8
Fig. 3	Electronic System for Time-of-Flight Observations	12
Fig. 4	Electronic System for Pulse Height Observations	15
Fig. 5	Electronic System for the Linearity Test	16
Fig. 6	Electronic System for Rise Time Observations	19
Fig. 7	Multichannel Adaptor - Coincidence Shaper	21
Fig. 8	Multichannel Adaptor - DC Amplifier and DC Level Adjust	23
Fig. 9	Multichannel Adaptor - Trigger Gate	24
Fig. 10	Multichannel Adaptor - Scale of Four	26
Fig. 11	Multichannel Adaptor - Reset Shaper	27
Fig. 12	Schematic Diagram of Pulse Relations for Linearity Test	38
Fig. 13	Typical Data and Curve Fit to the Full Time-of-Flight Spectrum	43
Fig. 14	Typical Pulse Height Spectrum Observed by Detector #2 with Window Settings of the Single Channel Analyzer	45
Fig. 15	Pulse Height Response as a Function of Field for Detector D-1	49
Fig. 16	Pulse Height Response as a Function of Field for Detector D-8	50
Fig. 17	$\overline{T}' - \overline{T}_o'$ as a Function of Pulse Height for the Median Heavy Fragment of Cf^{252} - Detector D-1	55

		Page
Fig. 18	$\overline{T}' - \overline{T}_o'$ as a Function of Pulse Height for the Median Light Fragment of Cf^{252} - Detector D-1	56
Fig. 19	$\overline{T}' - \overline{T}_o'$ as a Function of Pulse Height for the Median Heavy Fragment of Cf^{252} - Detector D-8	57
Fig. 20	$\overline{T}' - \overline{T}_o'$ as a Function of Pulse Height for the Median Light Fragment of Cf^{252} - Detector D-8	58
Fig. 21	Trigger Shift as a Function of Pulse Height for Median Light and Heavy Fragments of Cf^{252} - Detector D-1	59
Fig. 22	Trigger Shift as a Function of Pulse Height for Median Light and Heavy Fragments of Cf^{252} - Detector D-8	60
Fig. 23	Average Mass as a Function of Velocity for the Heavy Fragment of Cf^{252} as Calculated from the Data of Milton and Fraser	74
Fig. 24	Average Mass as a Function of Velocity for the Light Fragment of Cf^{252} as Calculated from the Data of Milton and Fraser	75
Fig. 25	dV/dX as a Function of Mass for Lindhard's Theory of Electronic Stopping	77
Fig. 26	Velocity Distribution of Light Fragments of Cf^{252} with Average Energy $\overline{E}$ = 11.2 MeV	79
Fig. 27	Velocity Distribution of Heavy Fragments of Cf^{252} with Average Energy $\overline{E}$ = 6.8 MeV	80
Fig. 28	Calibration Curve of Detector D-1 for Median Heavy and Light Fragments of Cf^{252}	83
Fig. 29	Calibration Curve of Detector D-8 for Median Heavy and Light Fragments of Cf^{252}	84
Fig. 30	Comparison of Alpha Calibration and Schmitt Calibration with Time-of-Flight Calibration of D-1 for Median Heavy Fragments of Cf^{252}	86

		Page
Fig. 31	Comparison of the Alpha Calibration and Schmitt Calibration with the Time-of-Flight Calibration of D-1 for Median Light Fragments of Cf^{252}	87
Fig. 32	Comparison of the Alpha Calibration and Schmitt Calibration with the Time-of-Flight Calibration of D-8 for Median Heavy Fragments of Cf^{252}	88
Fig. 33	Comparison of Alpha Calibration and Schmitt Calibration with the Time-of-Flight Calibration of D-8 for Median Light Fragments of Cf^{252}	89
Fig. 34	Pulse Height Defect as a Function of the Average Energy for Median Light and Heavy Fragments of Cf^{252}	90
Fig. 35	Typical Data and Curve Fit for Detector Pulse	92
Fig. 36	Typical Data for a Pulser Pulse	94
Fig. 37	Observed Rise Times as a Function of Incident Particle Energy for Several Bias Voltages - Detector D-9	102
Fig. 38	Observed Rise Times as a Function of Incident Particle Energy for Several Bias Voltages - Detector D-10	103
Fig.39	Calculated Plasma Time as a Function of Incident Particle Average Energy - Detector D-9	104
Fig. 40	Calculated Plasma Time as a Function of Incident Particle Average Energy - Detector D-9	105
Fig. 41	Calculated Plasma Time as a Function of Incident Particle Average Energy - Detector D-9	106
Fig. 42	Calculated Plasma Time as a Function of Incident Particle Average Energy - Detector D-10	107

Page

Fig. 43 Calculated Plasma Time as a Function of Incident Particle Average Energy - Detector D-10 108

Fig. 44 Calculated Plasma Time as a Function of Incident Particle Average Energy - Detector D-10 109

Fig. 45 Observed Rise Time as a Function of Incident Particle Average Energy for Median Light and Heavy Fragments of Cf^{252} - Detector D-9 111

Fig. 46 Calculated Plasma Time as a Function of Applied Field - Detectors D-9 and D-10 112

Fig. 47 Comparison of Empirical Calibration Curve with Experimental Data - Detector D-1 115

Fig. 48 Comparison of Empirical Calibration Curve with Experimental Data - Detector D-8 116

LIST OF TABLES

		Page
Table I.	Comparison of the Figures of Merit Proposed by Schmitt and Pleasonton with those Observed with Detectors D-1 and D-8	11
Table II.	Electronic Components for Time-of-Flight and Pulse Height Measurements	13
Table III.	Electronic Components for the Linearity Test	17
Table IV.	Electronic Components for the Rise Time Measurements	20
Table V.	Results of the Measurement of Energy Loss Within the Source	36
Table VI.	Results of the Observation of $\overline{T}'-\overline{T}_o'$ with Detector D-1	53
Table VII.	Results of the Observation of $\overline{T}'-\overline{T}_o'$ with Detector D-8	54
Table VIII.	Results of Energy Calibration of Films for Rise Time Measurements	62
Table IX.	Results of Pulse Height and Time-of-Flight Observations with Detector D-1	81
Table X.	Results of Pulse Height and Time-of-Flight Observations with Detector D-8	82
Table XI.	Summary of Calculation of T_{min} as a Function of Bias for Detectors D-9 and D-10	99
Table XII.	Results of Rise Time Observations with Detector D-9 and No Coincidence	100
Table XIII.	Results of Rise Time Observations with Detector D-10 and No Coincidence	101

List of Tables continued

		Page
Table XIV.	Results of Rise Time Observations with Coincidence	110

I. INTRODUCTION

Semiconductor radiation detectors have met with considerable success in many fields of nuclear research principally because of their small size, simplicity and excellent energy resolution.

The number of ion pairs, N_o, created by an incident particle within a semiconductor detector is

$$N_o = E/w \qquad (1)$$

where E is the incident particle energy and w is the energy expended per ion pair formed. Experiments have shown (M10, G2) that w is essentially independent of particle type with the exception of heavy ions such as fission fragments (B1). The fact that w is apparently larger for heavy ions results in a pulse height defect which can be defined as (K1)

$$\Delta = E\,(1 - PH_{FF}/PH_{\alpha}). \qquad (2)$$

Δ is the pulse height defect in energy units; E is the energy of the heavy ion; PH_{FF} is the observed pulse height of the heavy ion and PH_{α} is the expected pulse height of an alpha particle of the same energy.

The pulse height defect has been ascribed to three different effects:

(1) Gold Film Loss

Surface barrier detectors have a thin gold film deposited over the front surface of the detector to act as an electrode. Energy lost by an incident particle in the gold layer does not contribute to the observed signal from the detector. The discussion in this dissertation is limited to surface barrier

detectors. Diffused junction detectors have relatively thick "dead layers" on their front surfaces which have the same type of effect as the gold layer in surface barrier detectors. Typically this gold film is about 100 Angstroms thick which results in negligible energy loss for an alpha particle while fission fragments may lose as much as 0.5 MeV. This discrepancy contributes to the pulse height defect by reducing the energy available to produce ionization for a fission fragment as compared with an alpha particle.

(2) Non-ionizing Nuclear Collisions

For light particles such as alphas, electronic collisions dominate the energy loss process and nuclear collisions have almost negligible effect (B6). On the other hand, fission fragments experience nuclear collisions while still relatively energetic and such collisions play a significant role in the energy loss processes towards the end of the fragment track (B6). With regard to a semiconductor detector the question arises as to the efficiency of struck lattice atoms for producing ionization since the pulse height is proportional to the number of ion pairs formed (F2).

The general problem of non-ionizing collisions in detectors has been treated theoretically by

Lindhard et al (L1) and subsequent experiments by Sattler (S2) support the theory. Haines and Whitehead (H1) used the Lindhard formalism to calculate the energy lost to non-ionizing nuclear collisions for any type of ion incident upon a silicon detector and concluded that fission fragments should lose several MeV via non-ionizing collisions.

Recently, Moak et al (M9) have reported observations in which the pulse height defect was eliminated by aligning the detector crystal axis parallel to a well-collimated beam of iodine ions. Their interpretation was that channelling by the incident heavy ions reduced nuclear collisions to a minimum which leads to the conclusion that the pulse height defect is due solely to non-ionizing nuclear collisions.

(3) Recombination Losses

The separation and collection of the carriers created by an incident charged particle within the depletion region is accomplished by the applied field. The simplest model of collection assumes a field-independent mobility and negligible distortion of the field by the ionization. In this case, the collection time is directly related to the transit time across the depletion region. For the particular case of a surface barrier detector and a particle range much less than the width of the depletion

region, the result is (W2)

$$t_c = \frac{0.53\ d^2}{\mu V} . \qquad (3)$$

t_c is the collection time; d is the width of the depletion region; μ is the mobility and V is the applied bias voltage.

Miller, et al (M1) observed that the rise times of pulses due to fission fragments were an order of magnitude greater than that predicted by equation (3). This led the authors to introduce the concept of a "plasma time" based on the hypothesis that the dense column of ionization along the particle track shielded itself from prompt collection by the applied field. The plasma time is roughly defined as the time required for the ionization column to disperse to the point where normal field collection can proceed. It has been argued (M7) that since the collection process is thus impeded, recombination within the ionization column makes a significant contribution to the pulse height defect.

In principle the magnitude of the plasma time can be reduced by increasing the applied field and experiment has shown (S1, B1) that at least in some detectors the pulse height defect does decrease as detector bias increases. Unfortunately, the field cannot be increased without limit, since non-linearities due to multiplication effects will then

be introduced (W3, A1).

In spite of the considerable investigation into the pulse height defect there is still no clear explanation of the exact cause. It is certain that the gold film losses contribute but this only accounts for a small portion of the defect. The experiments by Moak with channelling effects seem conclusive but cannot explain the bias dependence of the pulse height defect observed by others.

One area of investigation that has been neglected is the dependence of the pulse height defect on the energy of the incident particle. Experiments reported with accelerated ions (M9, S3) do not go below 30 MeV and studies of the plasma effect have been made with undegraded fission fragments only (M5).

The goal of the present experiments was to examine the energy dependence of the pulse height defect to as low an energy as possible and to explore the energy dependence of the plasma time in an attempt to establish its relation to the pulse height defect.

II. EXPERIMENTAL

A. Apparatus

1. Counting Cell and Vacuum System

The cell was a hollow aluminum cylinder with an inside diameter of 3.0 inches and a length of 9.99 inches. Each end had a removable end plate, sealed hermetically with an O-ring. The end plates had detector mounts at their centers and one plate held a source holder and an externally controlled shutter as well. With the shutter closed the source was covered on both sides, thus protecting the detectors from radiation damage while experiments were not in progress. The cell and shutter arrangement are shown in Figure 1.

For some of the experiments the cell was fitted with a sliding detector mount (not shown in Figure 1) in the form of a lucite cylinder fitting snugly inside the counting cell. This permitted the distance from the source to detector #1 to be varied.

Figure 2 illustrates the simple glass vacuum system consisting of a mechanical vacuum pump, cold trap, McLeod gauge, mercury manometer and connecting tubing. The system was capable of producing a vacuum of better than 0.01 mm Hg. It was estimated that a pressure of 0.1 mm Hg. or less was required to insure negligible energy loss along the flight path.

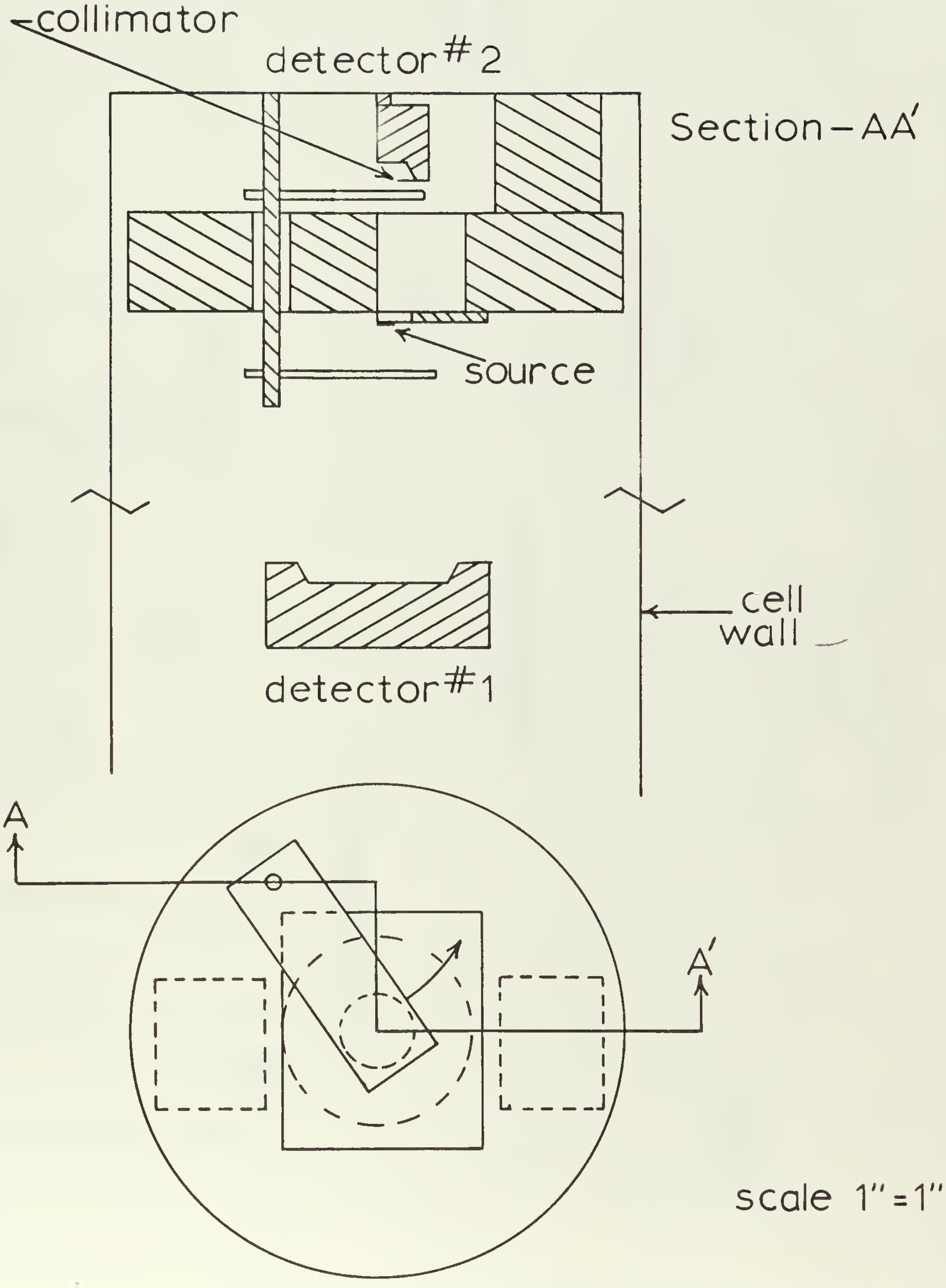

FIG. 1

COUNTING CELL AND SHUTTER

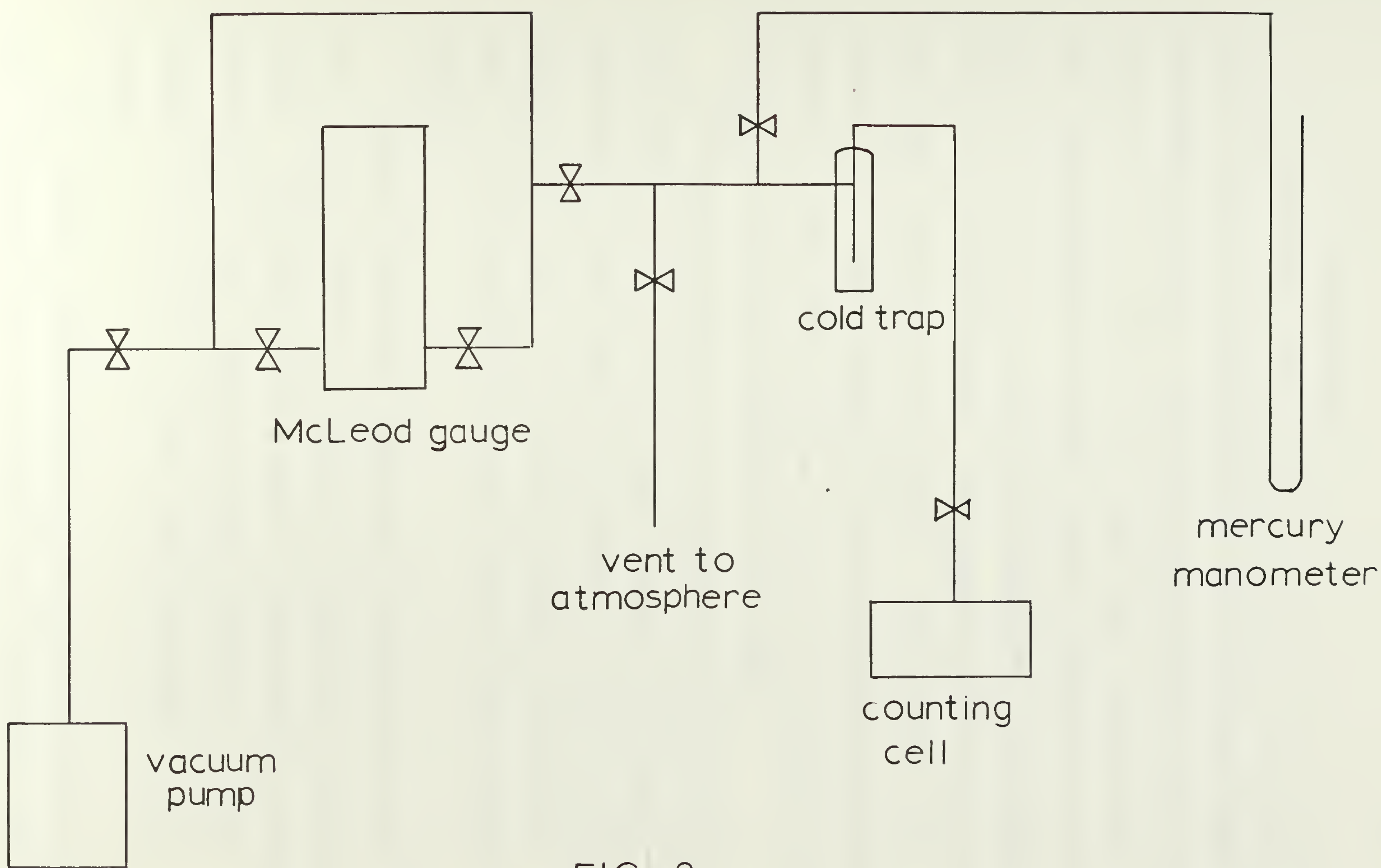

FIG. 2
VACUUM SYSTEM

2. The Detectors

The detectors used in all experiments were surface barrier detectors manufactured by the Oak Ridge Technical Enterprises Company. Two large area detectors were the subjects of the calibration. The first, detector D-1, was ORTEC model SBQN450-60, serial number 3-749E, with an active area of 450 mm^2 and a gold film thickness of approximately 75 Å on the front surface. The nominal resistivity of the n-type silicon was 350 ohm-cm. The detector was operated at a bias voltage of 100 volts which produced a depletion layer of 95 microns. This is the detector that was used in the work reported by Mulás (M2).

The second detector to be calibrated, detector D-8, was ORTEC model SBI 450-60, serial number 6-187B, with active area 450 mm^2 and gold thickness of about 100 Å. The operating bias of 250 volts produced a depletion layer of 330 microns in the 1750 ohm-cm n-type silicon detector.

A smaller detector, ORTEC model SBEI050-60, serial number 5-902, was used to provide timing and coincidence signals. This detector was made of n-type silicon with resistivity of 1150 ohm-cm and was operated at a bias voltage of 100 volts to give a depletion depth of 150 microns.

The fission fragment spectra obtained with the two large detectors were in reasonably good agreement with the

figures of merit proposed by Schmitt and Pleasonton (S4). These are listed in Table I.

The two detectors used in the plasma time studies were ORTEC model SBEG100-60. Both detectors had an active area of 100 mm^2 and the silicon slices had a thickness of 0.020 inches. Detector D-9, serial 4-122C, had a resistivity of 660 ohm-cm and detector D-10, serial 5-433C, had a resistivity of 900 ohm-cm.

3. Electronic System

(a) Time-of-Flight

A block diagram of the electronic system for time-of-flight observations is shown in Figure 3 and the components are listed in Table II. Signals generated within the detectors by incident particles triggered the time pick off units (TPO) which provided timing signals to the time-to-pulse height converter (TPHC). The time interval seen at the TPHC was the difference between the flight times of a pair of fission fragments travelling in opposite directions to detectors #1 (the one to be calibrated) and #2 over evacuated flight paths of known length. This time interval was converted to a pulse of proportional amplitude which was stored in the pulse height analyzer (PHA) subject to a coincidence requirement.

Coincidence was demanded between the output of the TPHC and the output of a single channel analyzer (SCA) which produced a pulse whenever the amplified signal from

TABLE I

Comparison of the Figures of Merit Proposed by Schmitt and Pleasonton with those Observed with Detectors D-1 and D-8

Parameter	Result D-1	Result D-8	Expected Value
N_L/N_V	2.12	2.00	2.85
N_H/N_V	1.77	1.69	2.2
N_L/N_H	1.20	1.18	1.30
$\frac{L}{L - H}$	0.38	0.46	0.38
$\frac{H}{L - H}$	0.49	0.52	0.44
$\frac{H - HS}{L - H}$	0.75	0.87	0.70
$\frac{LS - L}{L - H}$	0.49	0.55	0.49
$\frac{LS - HS}{L - H}$	2.12	2.41	2.18

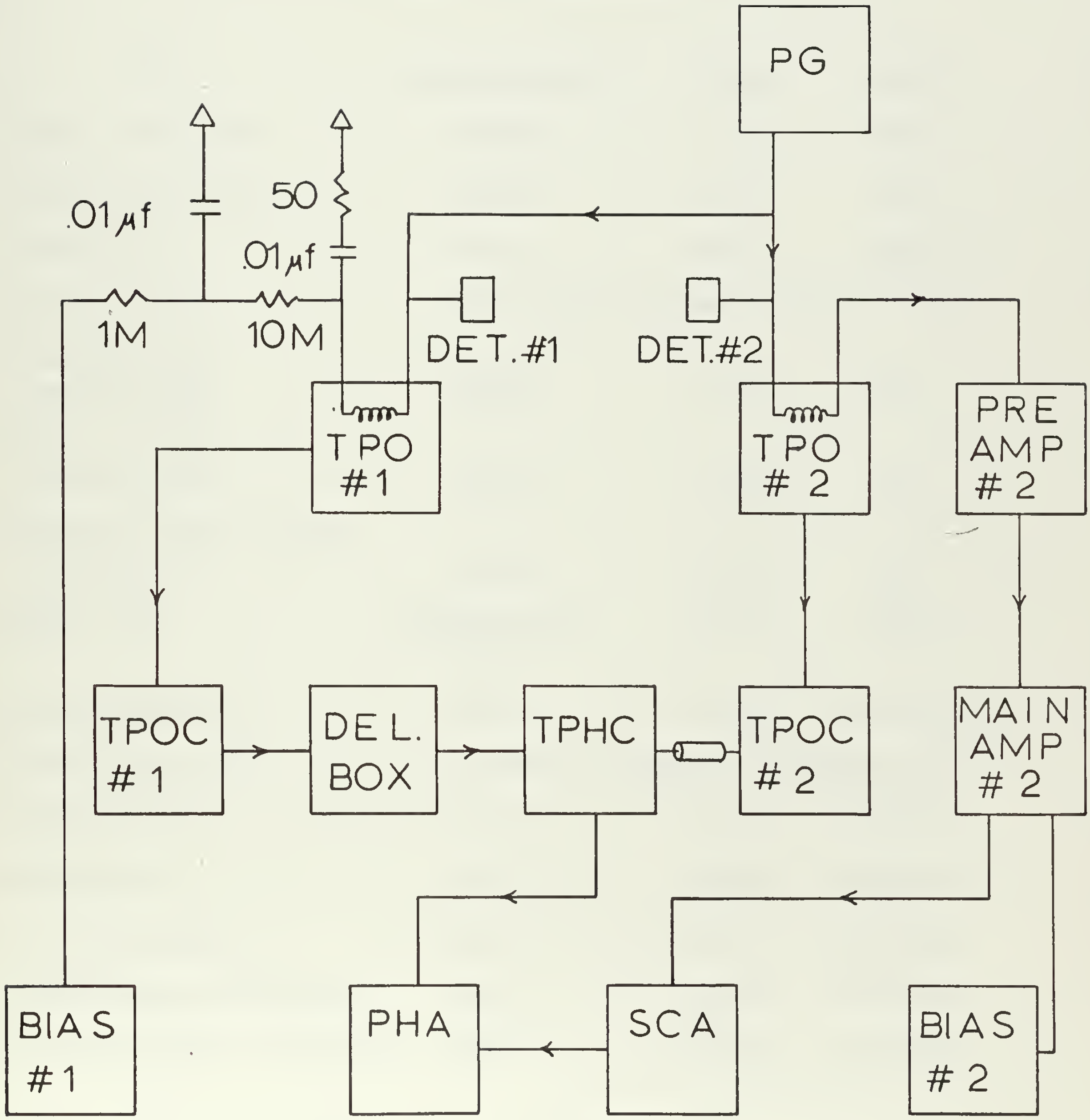

FIG. 3
ELECTRONIC SYSTEM FOR
TIME-OF-FLIGHT OBSERVATIONS

TABLE II

Electronic Components for Time-of-Flight and Pulse Height Measurements

Unit	Manufacturer	Model	Serial
Time pickoff #1	ORTEC	260	206
Time pickoff #2	ORTEC	260	202
Preamp # I	RIDL	31-18	76217
Preamp # II	Homemade version of RIDL 31-18		
Time pickoff control #1	ORTEC	403	46
Time pickoff control #2	ORTEC	403	44
Time to pulse height converter	ORTEC	405	24
Delay box	Nanosecond System	260	1793
Bias supply #2	RIDL	40-14	50A8234
Bias supply #1	Homemade version of RIDL 40-14		
Main amp #1	RIDL	30-21	25A7203
Main amp #2	RIDL	30-21	50B5337
Mercury pulser	RIDL	47-7	25A8209
Pulse Height analyzer	RIDL	34-12	86113-D
Single channel analyzer	RIDL	33-10B	50J7312

ORTEC - Oak Ridge Technical Enterprises Co.

RIDL - Radiation Instrument Development Laboratory

detector #2 fell within its window. This window bracketed either the light or heavy fission fragment peak of the fragments striking detector #2. When the window was set on the light peak, storage of the output of the TPHC was permitted only when a companion heavy fragment struck detector #1 and vice versa.

In order to standardize the time scale, pulses from a mercury switch pulser were introduced at the two TPO's and the time interval between start and stop pulses was varied with a variable delay box.

(b) Pulse Height

Data yielding the pulse height response of detector #1 was collected under identical conditions to each time-of-flight run. A block diagram of the electronic system is given in Figure 4 and the components are listed in Table II. In this instance the pulse height analyzer input was switched to receive the amplified linear signal from detector #1. The coincidence circuitry was identical to that used for time-of-flight observation. Pulses from the mercury pulser (PG) were introduced at the input to charge-sensitive preamp #1 to standardize the pulse height scale.

(c) Linearity

The electronic system shown in Figure 5 was used for an auxiliary experiment to test the linearity of the TPHC and PHA combination. The components are listed in Table III. Random pulses from a NaI scintillation counter

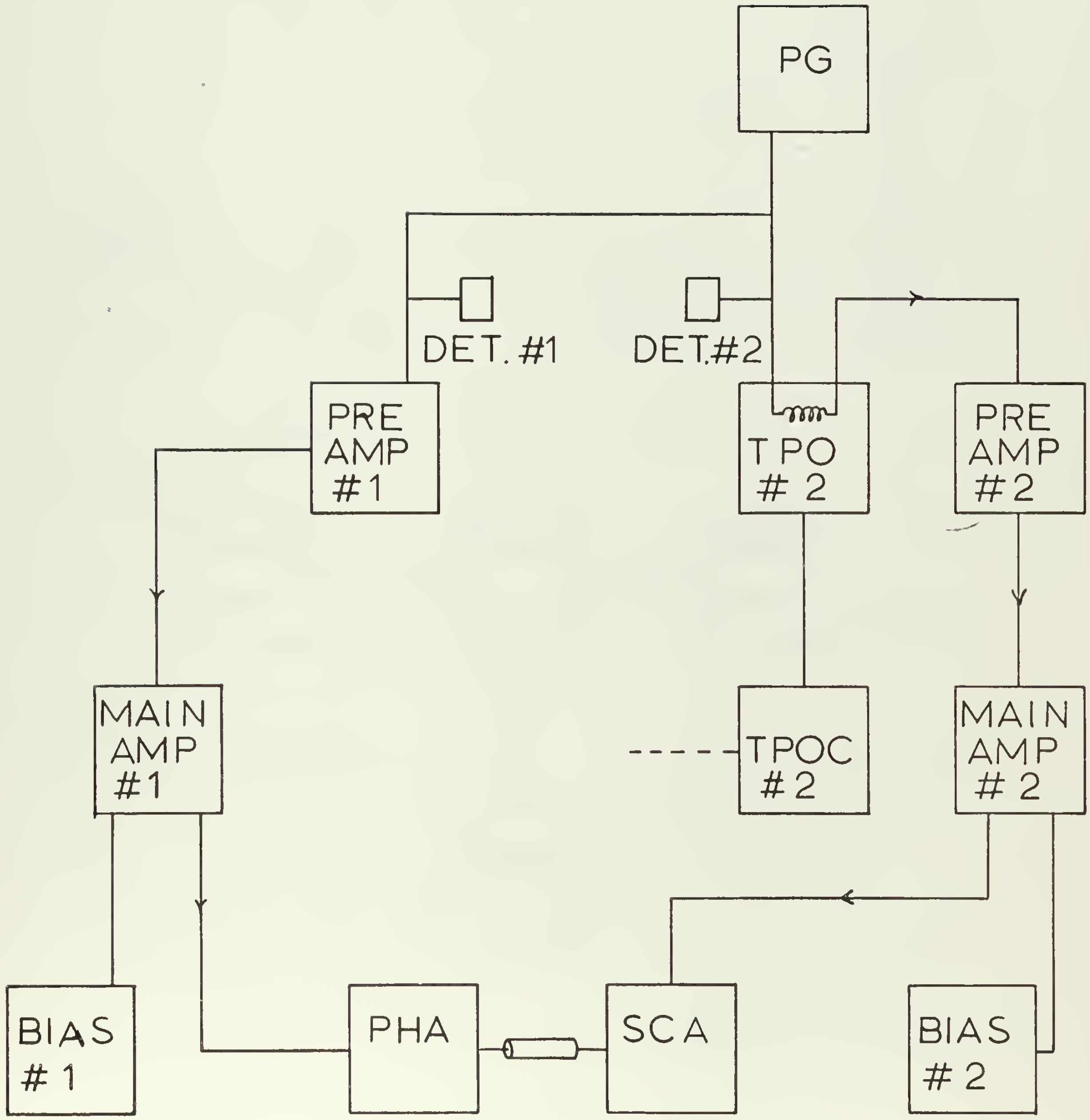

FIG. 4
ELECTRONIC SYSTEM FOR
PULSE HEIGHT OBSERVATIONS

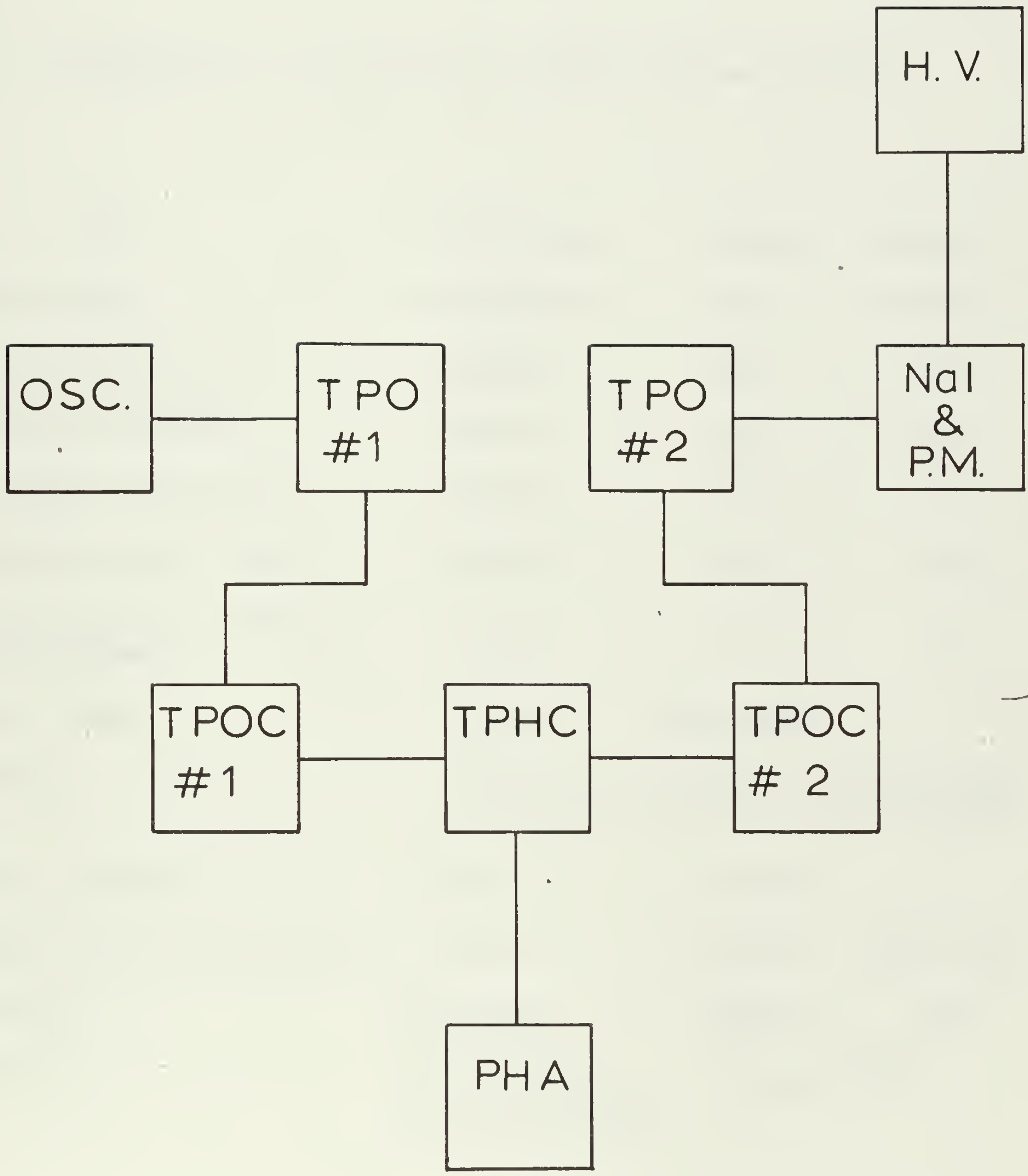

FIG. 5
ELECTRONIC SYSTEM
FOR THE LINEARITY TEST

TABLE III

Electronic Components for the Linearity Test

Unit	Manufacturer	Model	Serial
Oscillator	Tektronix	111	000645
Time pickoff #1	ORTEC	260	206
Time pickoff #2	ORTEC	260	202
Pickoff control #1	ORTEC	403	46
Pickoff control #2	ORTEC	403	44
Time to pulse height converter	ORTEC	405	24
Photo tube	CBS	CL-1008	-
Preamp	Homemade version of RIDL model 10-8A		
Power Supply	RIDL	40-9B	-
Pulse height analyzer	RIDL	34-12	86113-D
Crystal	Harshaw	AM366	7D8
Source	New England Nuclear Corp.	1.5 mc Co^{57}	

triggered TPO #2 to provide a start pulse to the TPHC while stop pulses were provided by the oscillator triggering TPO #2. The output of the TPHC was stored in the PHA with no demands on coincidence.

(d) Rise Time

The electronic system for rise time observations was, with minor modification, a scheme proposed by Steingraber and Berlman (S5). A digital representation of the vertical signal from a sampling oscilliscope was stored in consecutive channels of a multichannel scaler, with a one-to-one correspondence between samples of the oscilliscope sweep and memory location of the multichannel scaler.

A block diagram of the system is given in Figure 6 and the components are listed in Table IV. Detector #2 provided an external trigger to the oscilliscope via a time pickoff unit. The time pickoff unit discriminator was set to exclude triggering on alpha particles. The linear signal from detector #2 went to a single channel analyzer whose window could be set on either the light or heavy fission fragment peak as seen by detector #2. The output of the single channel analyzer was led to a shaper and thence to the detector gate input on the multichannel scaler. The shaper (shown in Figure 7) was required because the output of the single channel analyzer was of the wrong polarity and duration.

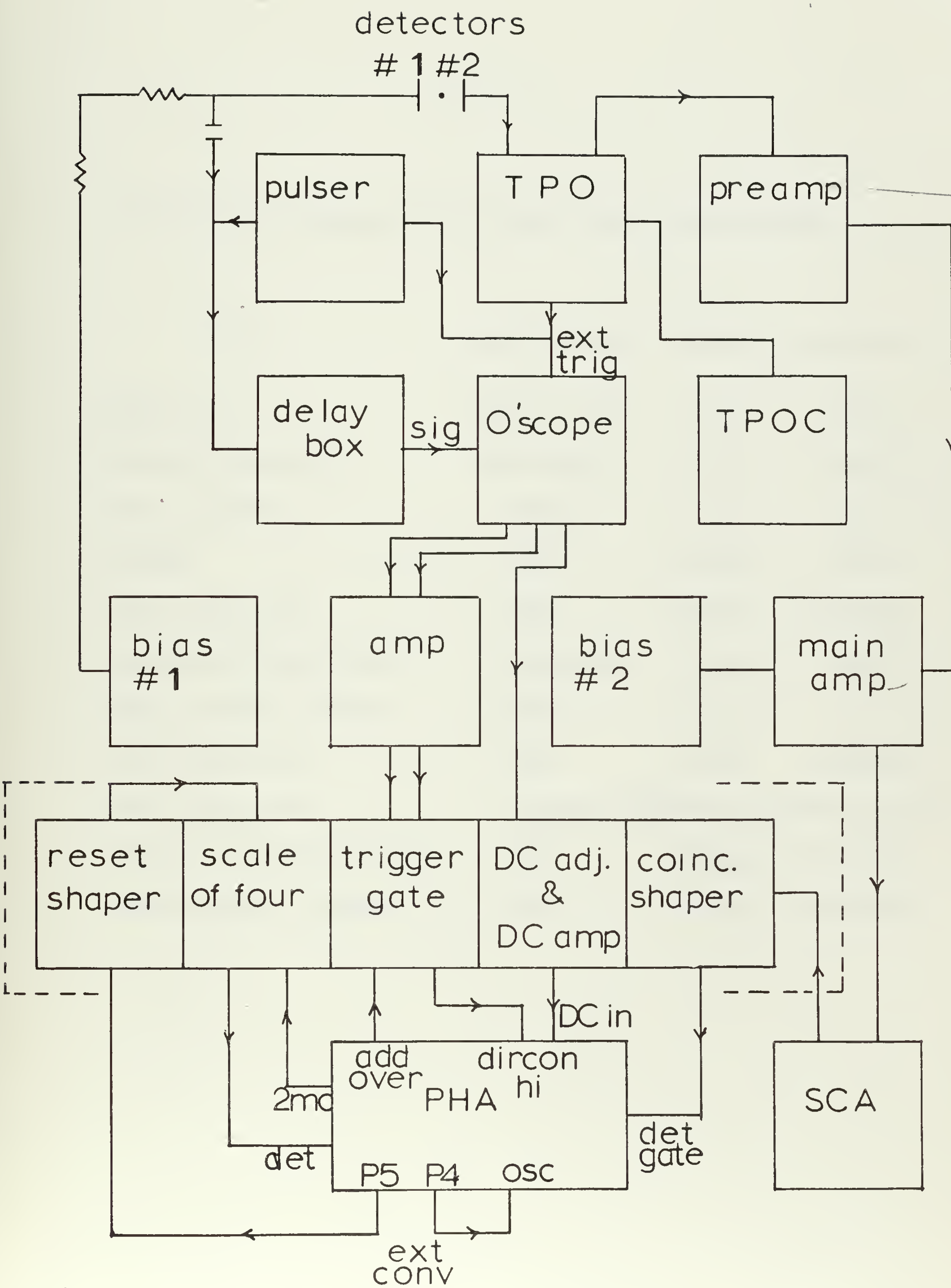

FIG 6
ELECTRONIC SYSTEM
FOR RISE TIME OBSERVATIONS

TABLE IV

Electronic Components for Rise Time Measurements

Unit	Manufacturer	Model	Serial
Delay box	Nanosecond	260	1793
Pulser generator	Tektronix	111	000645
Time pickoff	ORTEC	260	202
Preamp	RIDL	31-18	76217
Bias supply #1	RIDL	40-14	50A8234
Sampling oscilliscope	Tektronix	1S1	000182
Time pickoff control	ORTEC	403	44
Main amplifier	RIDL	30-21	50B5337
Bias supply #2	Homemade version of RIDL 40-14		
Single channel analyzer	RIDL	33-10B	50J7312
Multichannel analyzer	RIDL	34-12	86113-D

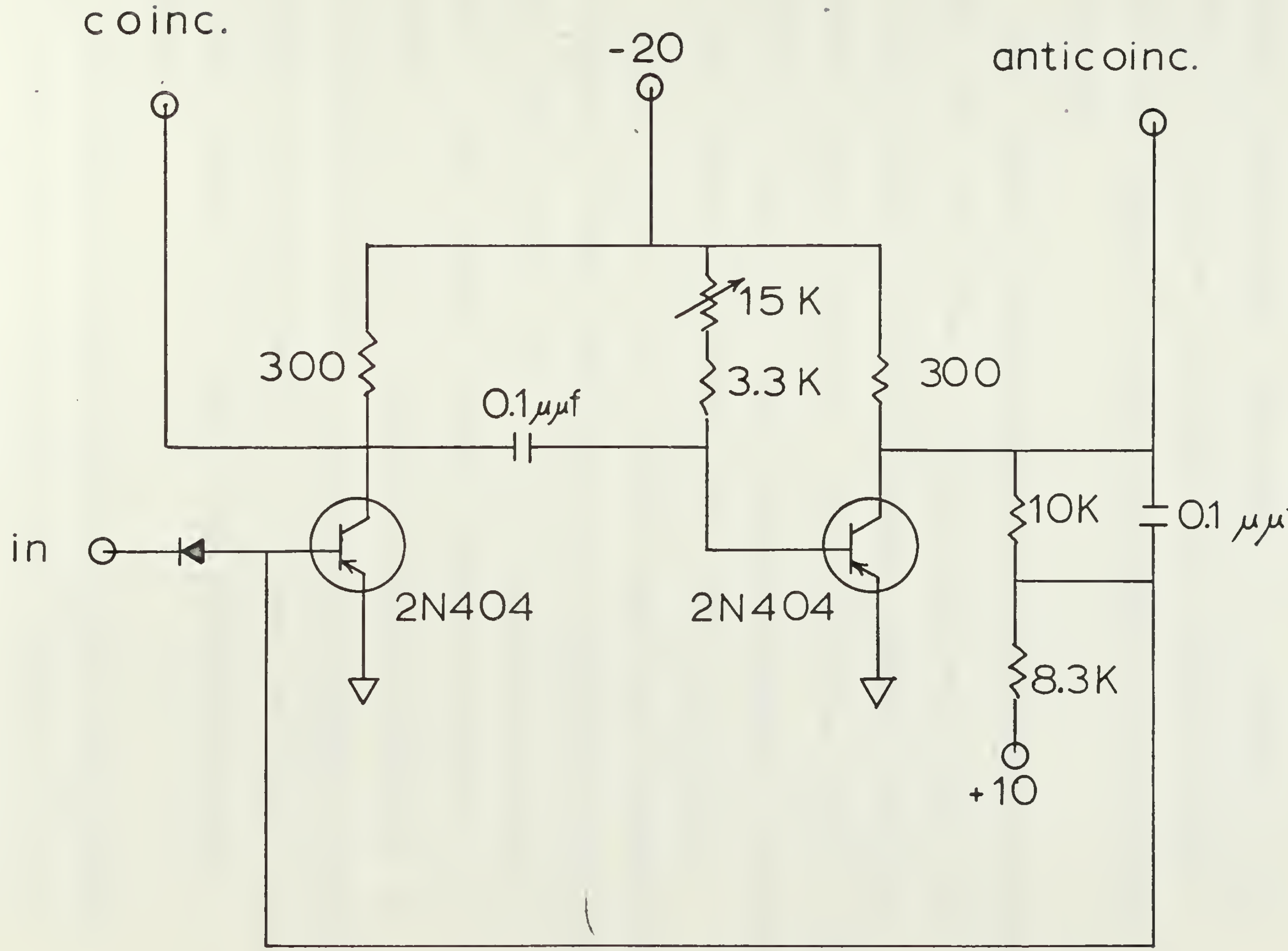

FIG. 7

MULTICHANNE ADAPTOR – COINCIDENCE SHAPER

The signal from detector #1 was taken to a delay box and then directly to the signal input of the sampling oscilliscope. The delay ($\sim$40 nanosec.) was required to achieve the proper time relation between signal and trigger to permit the signal to be displayed on the CRT.

The vertical signal output, the oscilliscope trigger signal, and the retrace blanking pulse were taken from the oscilliscope to the multichannel adaptor (enclosed by dotted line on Figure 6). The latter two signals were amplified at their exit from the oscilliscope to prevent the long cables from loading down the oscilliscope.

The DC level of the vertical signal was adjusted at the adaptor and then amplified by an operational amplifier with a gain of about ten. These circuits are shown in Figure 8. This signal was then applied to the DC (or Mössbauer) input of the analog-to-digital converter of the multichannel scaler. The DC level and gain adjustment described above were necessary to place the signal within the usable range (0 to -8v) of the analog-to-digital converter.

The amplified trigger signal from the oscilliscope went to the input of the trigger gate circuit shown in Figure 9. This circuit either blocked or passed the signal depending on the state of the bistable composed of T_1 and T_2. With T_1 off, T_3 was on and the trigger signal was shunted to ground. When T_1 was on, T_3 was off and the

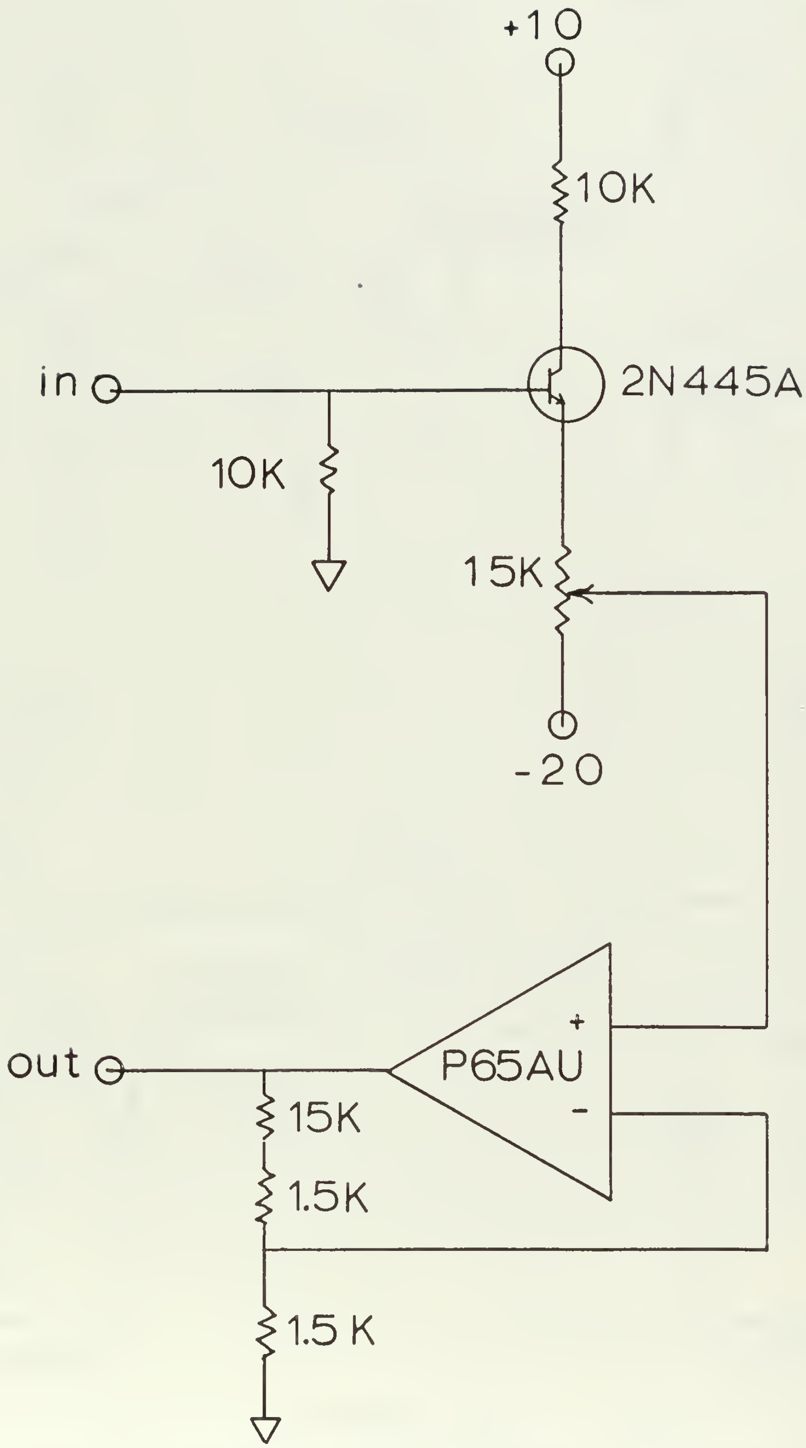

FIG. 8
MULTICHANNEL ADAPTOR—
DC AMPLIFIER AND DC LEVEL ADJUST

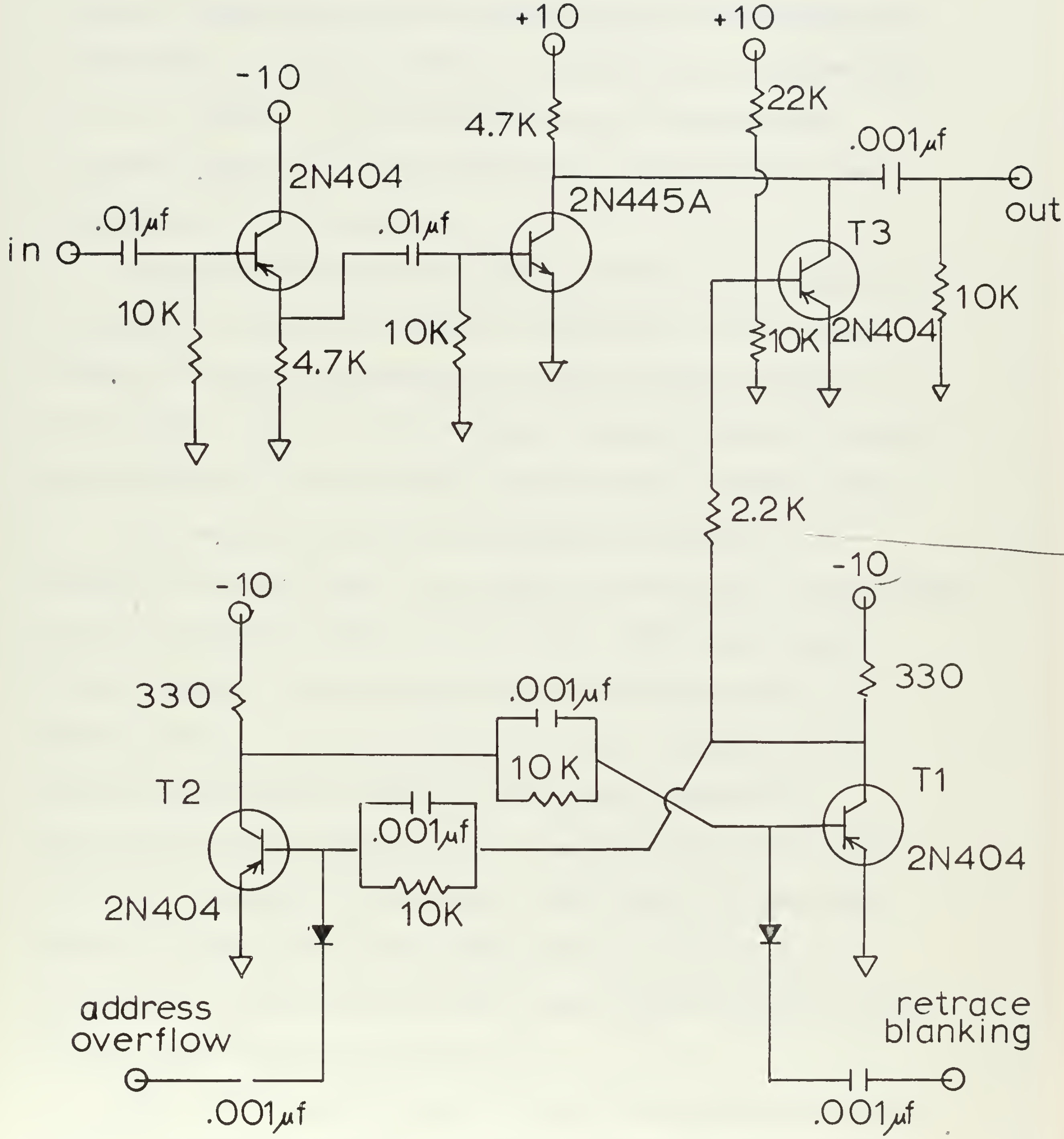

FIG. 9
MULTICHANNEL ADAPTOR — TRIGGER GATE

trigger signal passed to the output. T_1 was switched off by an address overflow pulse from the multichannel scaler, signifying that the multichannel had reached its last memory location before the oscilliscope reached the end of a sweep. T_1 was switched on by the retrace blanking pulse from the oscilliscope which marked the beginning of a new sweep.

Trigger signals which passed through the trigger gate strobed the analog-to-digital converter, thus causing analog to digital conversion of the DC level present at the input. The DC level was the vertical signal from the oscilliscope in coincidence with its own trigger signal.

The analog-to-digital converter produced a 2 megacycle pulse train, the length of which was proportional to the vertical signal at the input, when the trigger pulse arrived. This pulse train was scaled down by a factor of four and then applied to the detector input of the multichannel scaler, which could count at a maximum rate of about 500 kc. The circuit of the scale of four is shown in Figure 10. The scale of four was reset to zero before each pulse train arrived by the reset pulse from the ADC which was first amplified by the reset shaper shown in Figure 11.

The multichannel scaler stored the counts presented at its detector input in a single memory location until a channel advance pulse arrived at its oscillator input. The channel advance pulse was provided by the store pulse

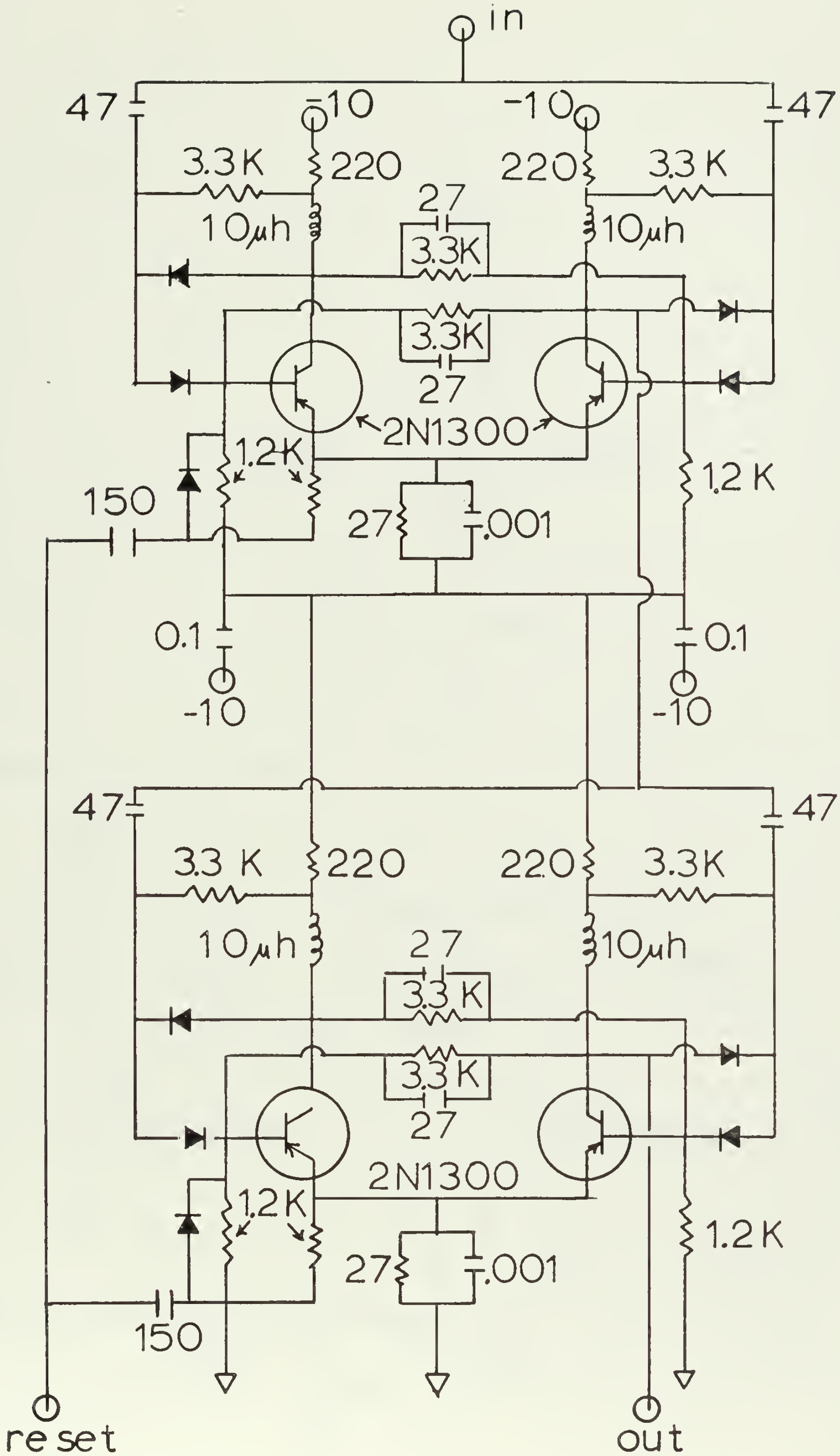

FIG. 10
MULTICHANNEL ADAPTOR
SCALE OF FOUR

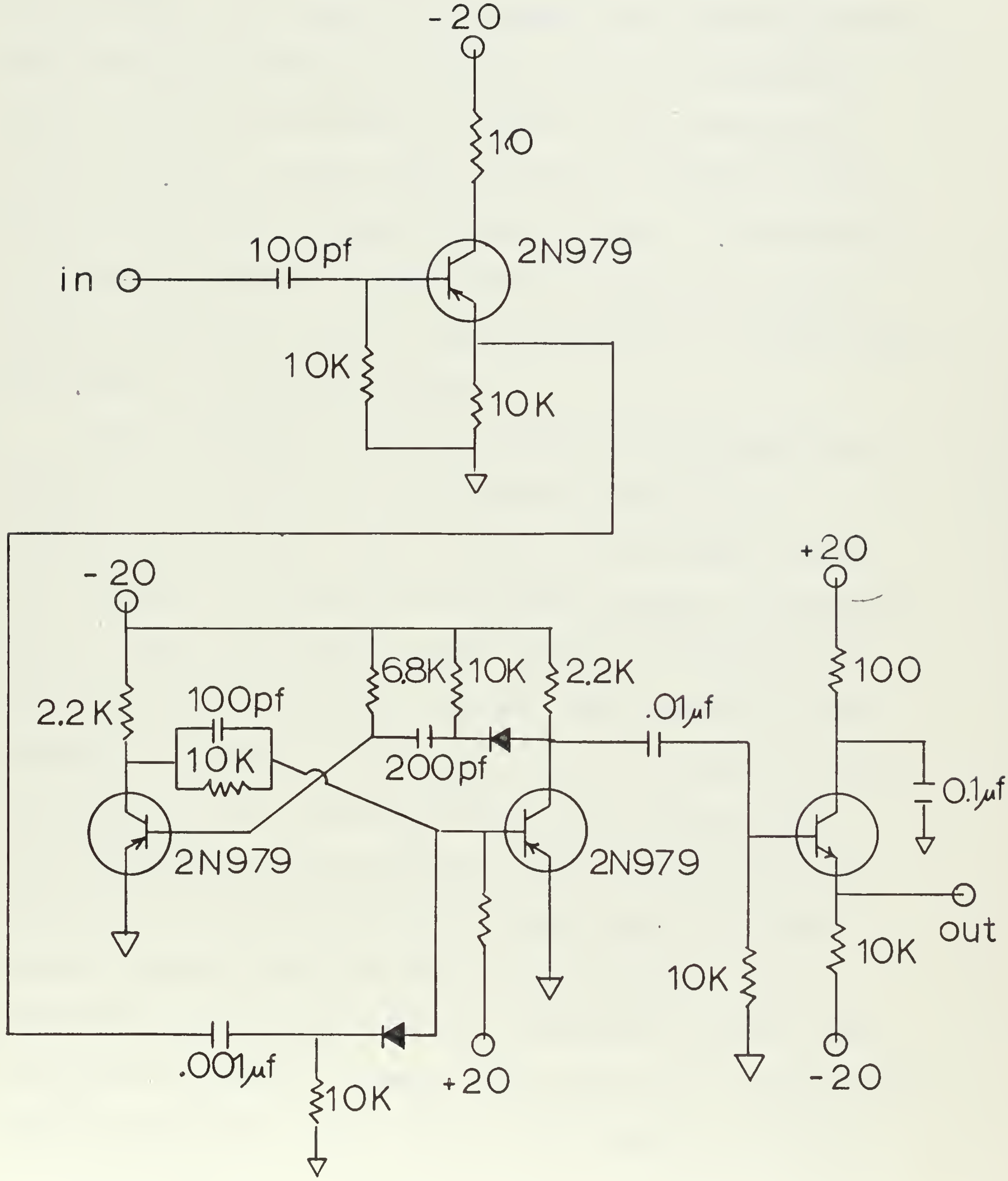

FIG. 11
MULTICHANNEL ADAPTOR
RESET SHAPER

from the analog-to-digital converter. Since the store pulse is generated by the final pulse of each 2 megacycle pulse train, each consecutive sample from the oscilliscope was stored in consecutive channels of the multichannel scaler. It was important to operate with a dead time close to zero to insure that the analog converter would not be busy when a trigger signal arrived. If that were to happen no channel advance would be generated and the sweep of the multichannel scaler would be out of step with the sweep of the oscilliscope.

For coincidence work the output of the coincidence shaper was connected to the detector gate of the multichannel scaler. The DC level of the shaper output was normally -20 volts which blocked storage of the pulse train. When the single channel analyzer triggered the shaper the output went to 0 volts. The monostable was adjusted to maintain this condition for a length of time (0.5 milliseconds) which overlapped the longest pulse train presented to the detector input. Thus only pulse trains in coincidence with the signal from the single channel analyzer were permitted to be stored. This coincidence arrangement did not interfere, however, with the channel advance. Signals which were not in coincidence merely contributed zero counts to the channel involved.

4. Radioactive Sources

A source of spontaneously fissioning Cf^{252} was

used for calibration of the detectors and for the study of pulse rise times. This Cf^{252} source was sandwiched between nickel films of nominal thickness $50\,\mu g/cm^2$ and $100\,\mu g/cm^2$. The source diameter was about 2 mm and the source intensity approximately 4×10^5 fissions/min. The energy loss through the nickel films was determined experimentally and in all cases was less than 4 MeV.

A second Cf^{252} source was used for determining this energy loss through the nickel. This source was plated on a platinum disk over an area of about 4 mm diameter. This was a bare source with negligible energy loss within the source and had an intensity of about 10^5 fissions/min.

A Co^{57} gamma source was used in the experiment to test the system linearity (see Section II-C2). This was a 0.3 mc. source enclosed in a plastic case.

5. "Mylar" Absorbers

"Mylar" film was employed as an absorber to vary the energy of the fission fragments. The "Mylar" was available in sheets of nominal thicknesses 0.15 mil., 0.25 mil., 0.35 mil. and 0.50 mil., and any combination of the above could be laminated to give intermediate thicknesses.

A permanent set of "Mylar" absorbers was constructed with nominal thicknesses of 0.15 mil., 0.25 mil., 0.30 mil., 0.35 mil. and 0.40 mil. Holes of roughly 50 mm^2

were cut in thin pieces of plexiglass, 0.2 mm thick. The edges of the holes were smoothed and rounded with fine steel wool to reduce the scattering surface to a minimum. Then sheets of "Mylar" film were glued to the plexiglass, thereby covering the holes.

B. Experimental Considerations

1. Radiation Damage

(a) Time-of-Flight and Pulse Height Observations

One of the major problems influencing the experimental design was the possibility of radiation damage to the detectors. Studies by Britt and Benson (B2) show that the pulse height defect increases significantly after a dose of approximately 1.5×10^8 fission fragments/cm^2.

Such a change in detector response for detector #2 would have the same effect as drift in the window of the single channel analyzer. To reduce this effect and increase the detector lifetime, detector #2 was placed 2.37 cm from the source instead of flush against it. It was estimated that in this position the detector lifetime would exceed the duration of the experiments.

The detector response was checked at frequent intervals for any change in pulse height and the window adjusted accordingly. The change in response was typically less than 1.0 MeV between each check. A timing calibration was done at the beginning and end of all the time-of-flight

runs and the results compared in order to detect any electronic drift. In no case was there a significant difference in the two time calibrations.

There was no concern with extensive radiation damage to detector #1 since the count rate at this position was less than 200 fragments/cm^2-min.

(b) Rise Time

For the rise time studies detector #1 was moved to within a few millimeters of the source and the possibility of radiation damage was increased since the count rate in this position was about 5×10^4 fragments/cm^2-min. To keep the total dose under 2×10^8 fragments/cm^2 it was necessary that the experiments on a single detector be completed in less than sixty hours. A preliminary set of experiments substantiated this prediction. Over a period of one hundred hours of exposure, the rise time of a given detector was observed to increase by as much as a factor of two.

The final set of experiments was carried out with fresh detectors of low resistivity (low resistivity material is less susceptible to radiation damage (B2)). The total exposure for D-9 was thirty-nine hours and for D-10 was thirty-four hours. This resulted in a dose of $\sim 1.2 \times 10^8$ fragments/cm^2 for D-9 and of $\sim 1.0 \times 10^8$ fragments/cm^2 for D-10.

2. Source-Detector Alignment

A source of difficulty in the rise time experiments was the alignment of the source and the two detectors. The exact position and dimension of the source was unknown and as a result it was possible to achieve only a 50% coincidence rate between the two detectors. This meant that 50% of the trigger pulses from detector #2 to the oscilliscope had no companion signal from detector #1. The net effect was to increase the length of time required to achieve a smooth average pulse in the multichannel analyzer.

3. Collimation

The problems of collimation have been discussed in detail by Schmitt and Pleasonton (S4). For the present experiments it was found that only the small area detectors (50 mm^2) showed any improvement with regard to low energy tailing through the use of a collimator.

4. Miscellaneous

The alpha activity of Cf^{252} is approximately thirty times the fission activity so there was a definite possibility of observing a false coincidence due to alpha particles during the pulse height and time-of-flight experiments. Since the count rate at detector #2 was greater than that at the larger detector, there were many more gating pulses from the single channel analyzer than there were true coincidences. An alpha particle which

happened to strike detector #1 while the gate was open produced a pulse which was treated as a true fission fragment coincidence. In time-of-flight work this was no particular problem since events of this sort produce random time intervals which do not affect the calculation of average flight times for fission fragments. On the other hand, the pulse height spectra of the alpha particles and fission fragments overlap at low energy so it is important to minimize these false coincidences.

The only controllable factor, the width of the gating pulse, was reduced to 0.5 microsec. with the result that the false coincidence rate was less than 1% of the true coincidence rate.

With such a narrow gating pulse and the substantial difference in rise time between the TPHC and the linear amplifier used in pulse height measurements, it was necessary to have slightly different coincidence arrangements for the two types of experiments. For time-of-flight work the output of the single channel analyzer was fed directly to the delayed coincidence input of the multichannel analyzer. For pulse height work it was necessary to delay the output of the single channel analyzer by approximately 2 microsec. before feeding it to the delayed coincidence input of the multichannel analyzer.

In the time-of-flight experiments it was found that at low energies (<20 Mev), the triggering rate of the time pickoff unit varied considerably with the bias voltage of

detector #1. In order to avoid this inherent discrimination the bias voltage was increased until the triggering rate saturated. Thus detector D-8 was calibrated at 250 volts and D-1 at 100 volts.

C. Preliminary Measurements and Adjustments

1. Energy Loss Within the Source

As mentioned previously the Cf^{252} time-of-flight source was sandwiched between thin nickel films which slightly degraded the fission fragments. In order to determine the energy loss detector D-1 was calibrated by the Schmitt procedure (S3) with the bare Cf^{252} source. The method of calibration is suitable in this case since the fragments are only slightly degraded and the Schmitt procedure has shown good results for fragments in this energy range (S3). The results of this calibration were expressed in arbitrary PH units.

$$E_H = 18.17\ (PH) + 6.15 \qquad (4)$$

$$E_L = 17.37\ (PH) + 5.77 \qquad (5)$$

D-1 was then used to observe the pulse height spectra from both sides of the nickel-covered time-of-flight source. The channel numbers corresponding to the light and heavy peaks of these spectra were determined by the geometric procedure suggested by Schmitt (S3). These values were converted to PH units which were used in either equation (4) or (5) to determine the average energy associated with each peak.

In addition it was necessary to know the average velocities of the light and heavy fragments from the nickel-covered source. These were calculated from the average energies.

$$\overline{v^2} = \frac{\overline{E}}{0.518\,\overline{A}} \qquad (6)$$

and from the definition of the standard deviation,

$$\overline{v}^2 = \overline{v^2} - \sigma^2\,(V) \qquad (7)$$

where $\overline{V}$ is expressed in units cm/nanosec., $\overline{E}$ is in MeV and $\overline{A}$ is the average fragment mass in amu.

The results of these calculations are summarized in Table V.

2. System Linearity

The timing system measured the time interval between two pulses by converting this time interval to a pulse of proportional height and then storing this pulse in the appropriate channel of the pulse height analyzer. After many events, the spectrum in the analyzer was $N(T)\,dT$, the number of time intervals of length T between T and $T + dT$ where dT was the channel width in units of time. The conversion of channel numbers to time units assumed a linear relation between the two so it is important that the time-to-pulse height converter and pulse height analyzer combination indeed be linear.

An experiment to test the linearity was suggested by the manufacturer of the timing units. This experiment was performed with the electronic system shown in Figure 5.

TABLE V

Results of the Measurement of Energy Loss
Within the Source

"Closed" Side of Source (nominal thickness of Ni = 100μg/cm^2

Heavy	209.1	4.038	75.54	1.027	0.083	1.010
Light	296.2	5.753	100.05	1.822	0.069	1.348

"Open" Side of Source (nominal thickness of Ni = 50 μg/cm^2

Heavy	214.9	4.152	77.49	1.054	0.083	1.023
Light	303.2	5.892	102.31	1.863	0.069	1.363

* Value taken from (53).

A start pulse arriving from the NaI scintillator at time $\tau = 0$ triggered the ramp within the time-to-pulse height converter. If no stop pulse arrived between $\tau = 0$ and $\tau = T_{RESET}$, the time-to-pulse height converter reset itself and then awaited the next start pulse. Any other start pulses arriving between $\tau = 0$ and $\tau = T_{RESET}$ were ignored. Figure 12 shows a pair of consecutive stop pulses triggered by the fixed frequency oscillator. Start pulses which fell in the shaded area resulted in the uninteresting situation where the time-to-pulse height converter reset itself. Only start pulses occurring in the blank area (at a time less than T_{RESET} prior to a stop pulse) provided a time interval within the range of the time-to-pulse height converter. Thus, during the time T_{RESET} before a stop pulse the system became "alive" in the sense that a coincidence could occur.

If the system became "alive" at $\tau = 0$, then the probability that no start pulse would arrive from the source in time τ was $e^{-\gamma\tau}$, where γ equals the triggering rate of the time pickoff unit driven by the photomultiplier tube. The probability that a start pulse will arrive in any interval $d\tau$ was $\gamma d\tau$. The probability that the first start pulse would arrive between τ and $\tau + d\tau$ was the product of the above probabilities.

$$P(\tau)d\tau = \gamma e^{-\gamma\tau} d\tau \tag{8}$$

The time interval observed by the time-to-pulse height converter was $t = T_{RESET} - \tau$, so the probability

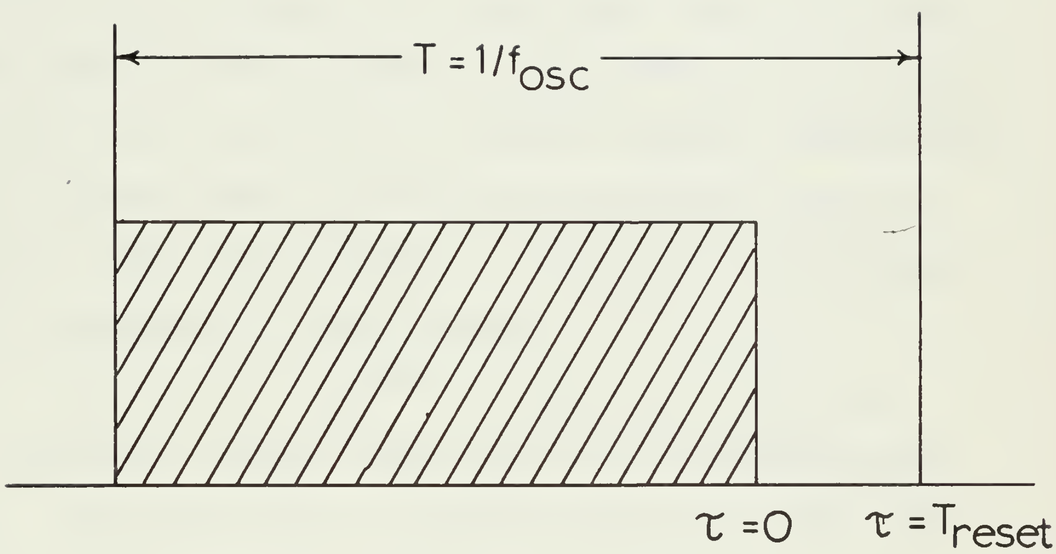

FIG. 12
SCHEMATIC DIAGRAM OF PULSE RELATIONS FOR LINEARITY TEST

of a time interval between t and t +dt was

$$P(t)dt = \gamma e^{-\gamma T_{RESET}} e^{\gamma t} dt. \quad 0 \leq t \leq T_{RESET} \tag{9}$$

The triggering level of the time pickoff unit was set so that γ = 150 cps and since T_{RESET} = 0.25 μsec, $\gamma T_{RESET} << 1$. For all $0 \leq t \leq T_{RESET}$, $e^{\gamma t} \approx 1$ with the result that

$$P(t)\ dt \propto dt. \tag{10}$$

All time intervals between t = 0 and t = T_{RESET} were equally likely.

The stop rate from the fixed frequency oscillator was 100 kc which resulted in a coincidence rate of 60 cpm. The start rate of 9000 cpm and the coincidence rate closely approximated the condition for fission fragment experiments.

The spectrum resulting from this experiment was fit to a second order polynominal by a non-linear least square (B5, M8) technique with final result

$$f(X) = N(1 - 0.119 \times 10^{-3}X + 0.428 \times 10^{-6} X^2). \tag{11}$$

Here X represents channel number and N is a normalization constant. Over the range of interest ($160 \leq X \leq 360$) this resulted in a variation of $\pm 1\%$.

3. Standardization of the Time Scale

The measurement of fission fragment flight times required a consistent method of relating the channel numbers of the pulse height analyzer to the time interval observed at the time-to-pulse height converter.

This was accomplished by determining the equivalent flight time corresponding to the various settings on a

variable delay box. The delay box provided fixed delays over a range of eighty nanoseconds at four nanosecond intervals.

The "equivalent time" of each delay box setting was determined from observation of the full time-of-flight spectrum of undegraded fission fragments, with each observation of about one hour's length being preceded and followed by a delay box run. These were done under identical electronic conditions with the only difference being in the method of triggering the time pickoff units. During the fission fragment observations they were, of course, triggered by the detectors and during the delay box runs both time pickoffs were triggered by the pulse from a single mercury pulser. The delay box was inserted in the signal path of the start side of the time-to-pulse height converter and thus the time interval between start and stop pulses could be varied over a range of about eighty nanoseconds. A delay box run consisted of storing the output of the time-to-pulse height converter in the pulse height analyzer for one minute at each setting. The fission fragment runs were done with a delay box setting of zero.

The analysis of the fission fragment data started with the expression given by Whetstone (W1) as a reasonable representation of the velocity spectrum of undegraded

fission fragments.

$$g(v)dv \propto \left\{ \left[\frac{1}{\sigma(v)} \exp \left\{ -\tfrac{1}{2} \left(\frac{v-\bar{v}}{\sigma(v)} \right)^2 \right\} \right]_H + \left[\frac{1}{\sigma(v)} \exp \left\{ -\tfrac{1}{2} \left(\frac{v-\bar{v}}{\sigma(v)} \right)^2 \right\} \right]_L \right\} dv \tag{12}$$

Here the subscripts L and H refer to the light and heavy fragments respectively, $\bar{v}$ to the appropriate average velocity and $\sigma(v)$ to the appropriate standard deviation of velocity.

Setting $T_1 = D_1/v$ this expression is transformed in the usual fashion

$$h(T_1)dT_1 \propto g(D_1/T_1) \left| \frac{dv}{dT_1} \right| dT_1 \; . \tag{13}$$

This expression represents the spectrum of flight times, T_1, over the path length D_1 to detector #1. However, the observed time spectrum was in terms of the time interval at the time-to-pulse-height converter $T = T_1 - T_2$. T_2 is the flight time of a sister fragment to detector #2 over the flight path D_2. Since $\frac{D_2}{D_1} \approx 0.1$, T_2 was set equal to $\bar{T}_2$, the average flight time over D_2, and the expression $T_1 = T + \bar{T}_2$ was substituted into (13) yielding

$$f(T)dT \propto g(D_1/(T + T_2)) \left| \frac{dv}{dT} \right| dT. \tag{14}$$

Finally the observed time interval, T, was written as a linear function of channel number,

$$T = B_1X + B_2 \; , \tag{15}$$

and this was substituted into (14) giving an expression for the observed spectrum in terms of channel number X.

This expression was fit to the observed time spectrum by a non-linear least square technique (B5, M8) on a digital computer. B_1, B_2, $\sigma(v_H)$, $\sigma(v_L)$ and the normalization were variable parameters while $\bar{v}_L$ = 1.360 cm/nanosec., $\bar{v}_H$ = 1.023 cm/nanosec., $(\bar{T}_2)_L$ = 2.37 nanosec., $(\bar{T}_2)_H$ = 1.77 nanosec., and D_1 = 21.89 cm were held constant. The values of $\bar{v}$ and $\bar{T}_2$ were calculated from the measurement of energy loss through the nickel film and D_1 was obtained by direct measurement.

The values of B_1 and B_2 obtained from the curve fit were then utilized to calculate the T corresponding to each setting of the delay box by substituting into (15) the observed X corresponding to each setting on the delay box.

A representative set of data and the corresponding fitted curve are shown in Figure 13.

To estimate the error involved in substituting $\bar{T}_2$ for T_2 in equation (14) the standard deviation of T_2 was calculated.

$$\sigma(T_2) = \left|\frac{\partial T_2}{\partial v_2}\right| \sigma(v_2) = \frac{D_2}{\bar{v}_2^2} \quad \sigma(v_2) \qquad (16)$$

In the case of a heavy fragment striking detector #2 $\sigma(T_2)$ = 0.194 nanosec. and for a light fragment $\sigma(T_2)$ = 0.835 nanosec. Since the fitting procedure gave $T = B_1X + B_2 = T_1 - \bar{T}_2$, the error in relating T and X was of the order of $\sigma(T_2)$. Therefore, it was reasonable

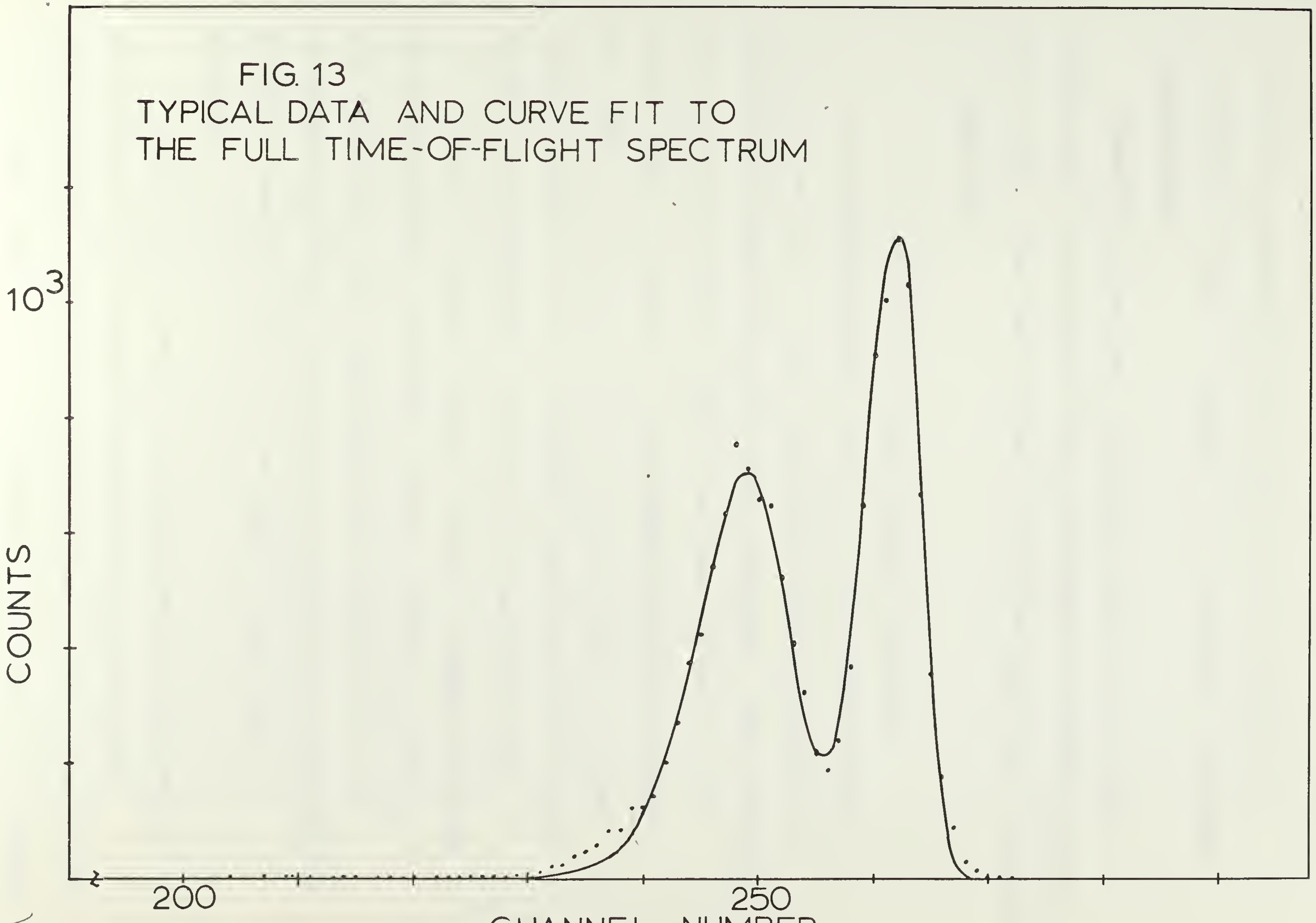

FIG. 13
TYPICAL DATA AND CURVE FIT TO THE FULL TIME-OF-FLIGHT SPECTRUM

to set the uncertainty of T equal to ± 0.1 nanosec. or $\pm 1.0\%$ since T was of the order of 10 nanosec. for these observations.

Therefore, the total systematic error in the time scale due to non-linearity and the method of standardization was $\pm 1.4\%$. The random error in the time scale was negligible by comparison.

4. Setting the Single Channel Analyzer

As mentioned briefly in II-A-3a the single channel analyzer as part of the coincidence system provided the selection between light and heavy fragments. The decision as to how the window should be set was subject to two conditions: it should be set symmetrically on either the light or heavy peak and the width should be chosen narrow enough to give the desired selectivity but not so narrow as to needlessly reduce the coincidence rate.

Figure 14 shows a typical fission fragment spectrum from detector #2 with three possible window selections for each peak. The experiments with detector D-1 all employed the window designated by 3/4 while the experiments with D-8 used all three window widths at one time or another.

Within the accuracy of the experiments there was no difference in the observed results for the different window widths employed for detector D-8. This is evidenced by the fact that all the calibration points fell on a smooth

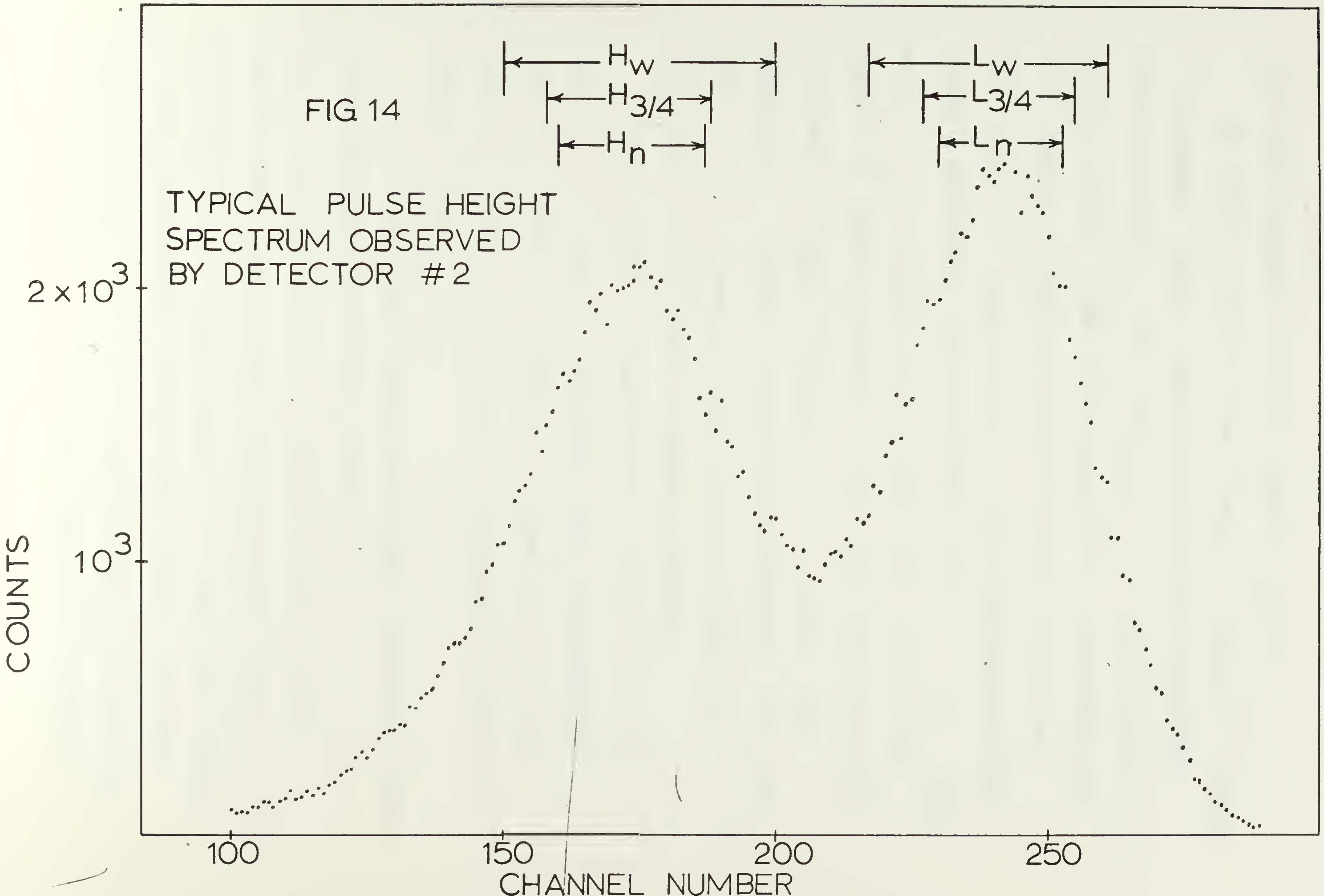

FIG 14

TYPICAL PULSE HEIGHT SPECTRUM OBSERVED BY DETECTOR #2

curve (see Figures 32 and 33, Section III-A3).

In order to achieve consistency in setting the window of the single channel analyzer, the window edges were defined in terms of the arbitrary pulse height units of the mercury pulser. This was accomplished by observing the Cf^{252} fission fragment spectrum with detector #2 and converting the channel numbers of this spectrum to pulse height units via a linear relation between the two. This relation was obtained from a least square fit of the results of pulser observation made both before and after the fission fragment observation. The pulser runs consisted of a series of peaks corresponding to selected pulse heights, observed under identical electronic conditions as the fission fragment spectrum.

This procedure of defining the window edges was repeated after about each twenty hours of operation to monitor the effect of radiation damage to detector #2. Only minor (<1.0 MeV) in detector response were observed between checks.

To set the window for an experiment, the pulse height corresponding to the lower window edge was set on the mercury pulser. The rate of gating pulses from the single channel analyzer was observed with a scaler and the threshold of the analyzer adjusted to reduce this rate to one half the repetition rate of the pulser. Then the mercury pulser was set on the pulse height corresponding to the upper edge and the window width of the analyzer

adjusted to again reduce the count rate by half.

5. Alpha Calibration

Both detectors, D-1 and D-8, were calibrated with alpha particles to give a comparison with the fission fragment calibration curve. This was accomplished by observing the pulse height response of the detectors to the alpha particles emitted by Am^{241} and Cf^{252}.

The procedure was the same as that for pulse height observation of fission fragments except that there was no coincidence requirement and the counting time for each alpha run was only fifteen minutes. Because of the relatively short counting time, the pulser standard runs were done before and after each set of five alpha runs instead of after each individual run as in the fission fragment experiments.

The source to detector distance for the alpha observation was about 3 cm. No effort was made to collimate the particles.

6. Schmitt Calibration

It was desired to compare the fission fragment calibration curve obtained in the present experiments with that obtained from the Schmitt (S3) calibration procedure.

To this end, the complete undegraded fission fragment pulse height spectrum from the bare Cf^{252} source was observed with detectors D-8 and D-1 at a path length of

3 cm. Three separate runs of about one hour in length yielding several thousand counts at each peak were made for both detectors. Each fission fragment run was preceded and followed by a pulser run.

7. Saturation Curves

A number of authors (B1, S1, K1) have reported a field dependence of the pulse height response of semiconductor detectors to fission fragments. Therefore, the detectors were checked for such an effect.

Observations were made of the light and heavy fragments separately at bias voltages ranging from 50 - 300 volts. The results of these observations are shown in Figure 15 for D-1 and Figure 16 for D-8.

Detector D-8 shows a relatively constant response over a wide range of bias voltages. On the other hand, detector D-1 exhibits no flat portion and shows signs of charge multiplication at a relatively low bias voltage. This is the type of behavior described by Walter (W3) which apparently is due to tunneling injection through the oxide layer on the surface.

8. Timing System Trigger Shift

The standardization of the time scale was based upon the flight times of undegraded fission fragments. It was found that for degraded fragments, triggering of the TPO shifted relative to the time of arrival of a particle at

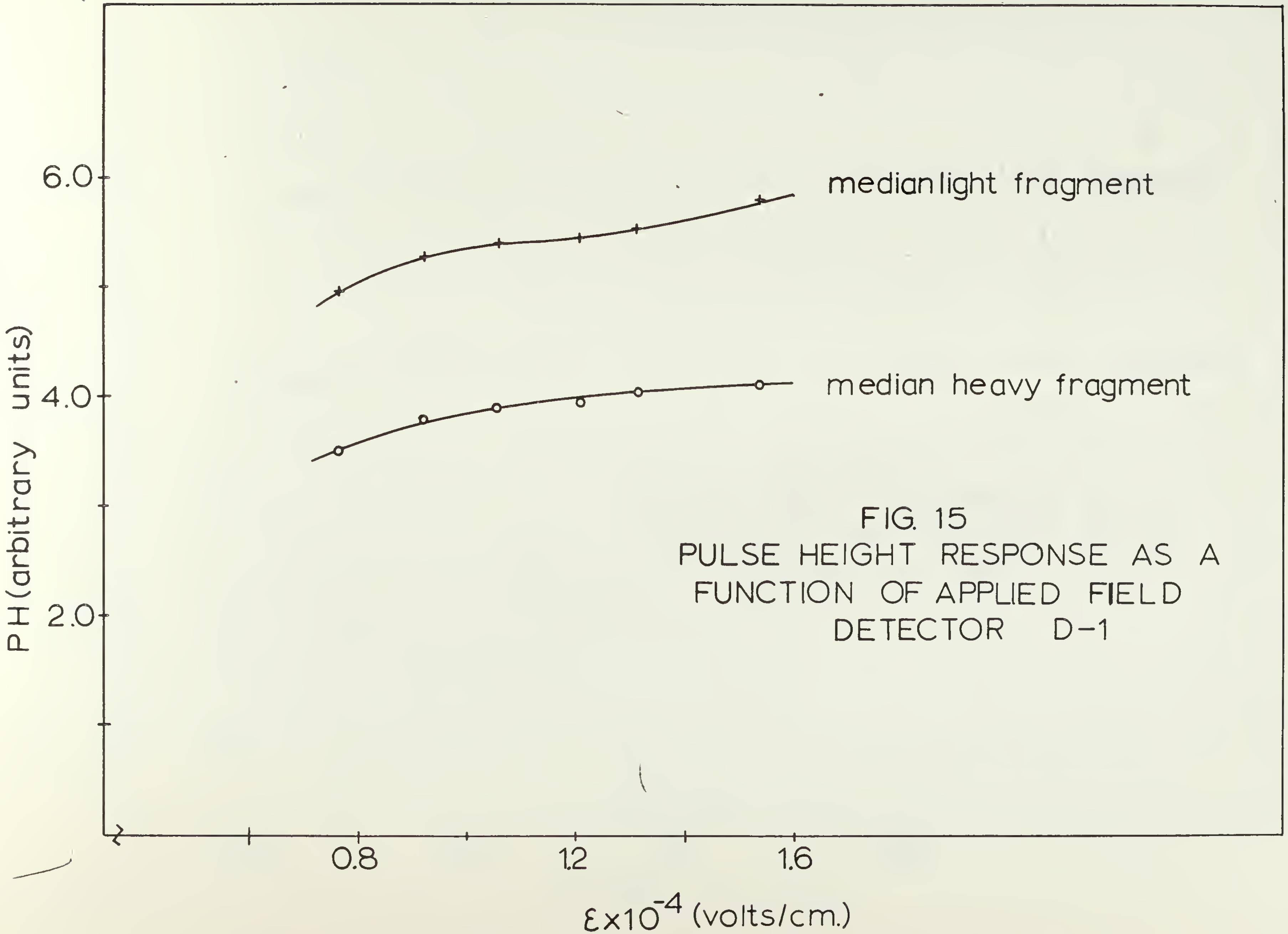

FIG. 15
PULSE HEIGHT RESPONSE AS A FUNCTION OF APPLIED FIELD
DETECTOR D-1

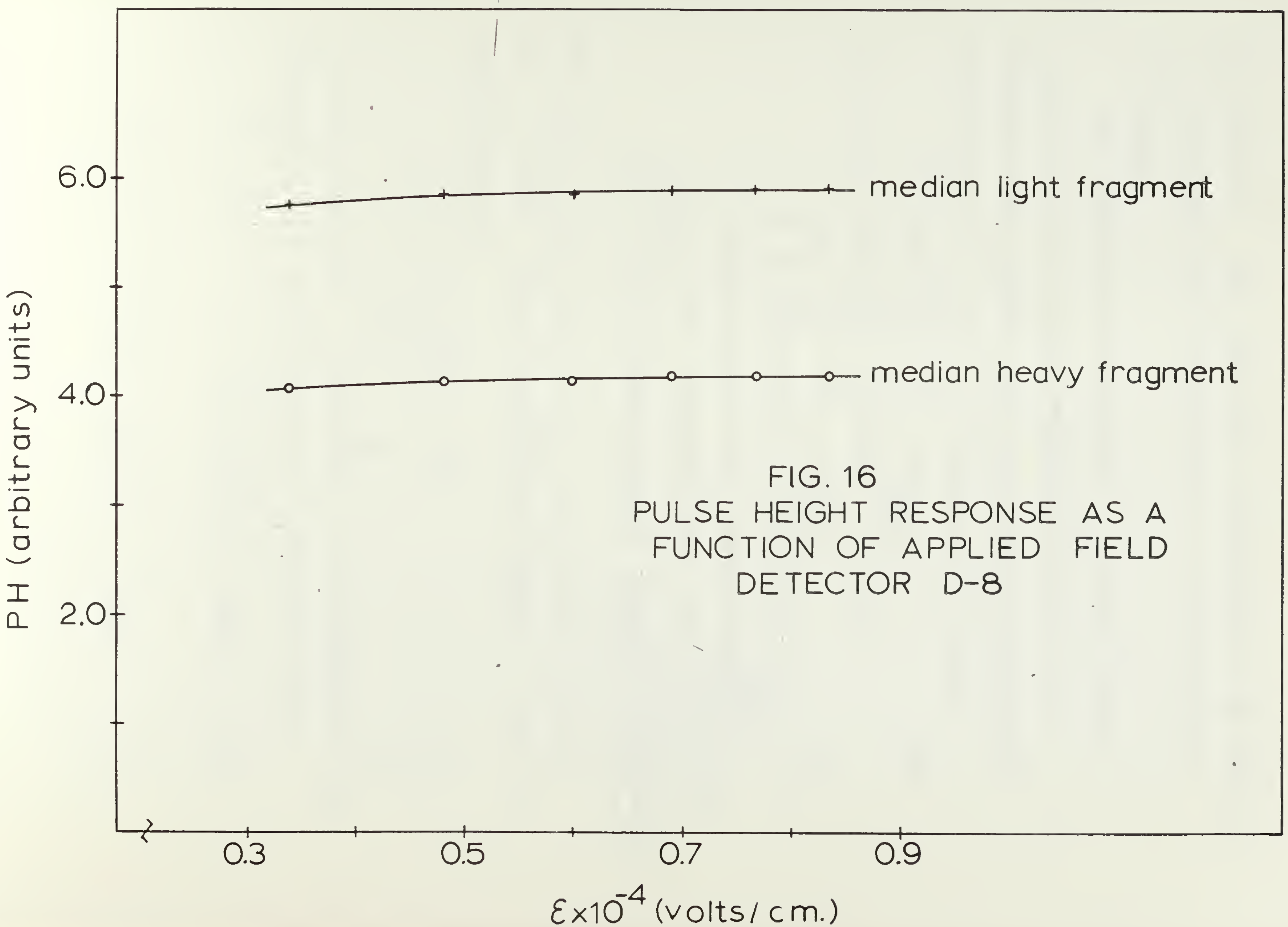

FIG. 16
PULSE HEIGHT RESPONSE AS A FUNCTION OF APPLIED FIELD
DETECTOR D-8

the detector. This time shift corresponded to as much as 1.5 MeV in the final calculation so a correction was necessary.

The magnitude of this effect was determined by comparing time-of-flight observations made at two different path lengths from the source to detector #1. Observations at a short path length D_1', yielded

$$\overline{T'} = D_1' \overline{\left(\frac{1}{v_1}\right)} + \overline{T}_2 + T_{SHIFT} \tag{16}$$

and at the normal path length $D_1 = 21.89$ cm

$$\overline{T} = D_1 \overline{\left(\frac{1}{v_1}\right)} + \overline{T}_2 + T_{SHIFT} \tag{17}$$

$\overline{T}$, $\overline{T'}$ is the average time interval seen by the TPHC;

$\overline{T}_2$ is the average flight time of fragments to detector #2;

T_{SHIFT} is the triggering shift relative to the undegraded case;

$\overline{\left(\frac{1}{v_1}\right)}$ is the average reciprocal velocity of fragments striking detector #1.

For observations with D-1, $D_1' = 1.34$ cm and with D-8, $D_1' = 1.23$ cm. Since by definition $T_{SHIFT} = 0.0$ for the undegraded case

$$\overline{T}_o' = D_1' \overline{\left(\frac{1}{v_{1,o}}\right)} + \overline{T}_2 \tag{18}$$

$$\overline{T}_o = D_1 \overline{\left(\frac{1}{v_{1,o}}\right)} + \overline{T}_2 \tag{19}$$

where the subscript o corresponds to the undegraded case. Subtracting (18) from (16) and (19) from (17) gives

$$\overline{T'} - \overline{T}_o' = D_1' \left[\overline{\left(\frac{1}{v_1}\right)} - \overline{\left(\frac{1}{v_{1,o}}\right)}\right] + T_{SHIFT} \tag{20}$$

$$\overline{T} - \overline{T}_o = D_1 \left[\overline{\left(\frac{1}{v_1}\right)} - \overline{\left(\frac{1}{v_{1,o}}\right)}\right] + T_{SHIFT} \tag{21}$$

(20) and (21) may be combined to give

$$T_{SHIFT} = \bar{T} - \bar{T}_o - D_1 \left[\frac{(\bar{T} - \bar{T}_o) - (\bar{T}' - \bar{T}_o')}{D_1 - D_1'} \right] \qquad (22)$$

$\bar{T}' - \bar{T}_o'$ and the average pulse height response of the detectors were observed for the light and heavy fragments separately with several different thicknesses of "Mylar" absorber covering the source. These results are plotted in Figures 17 and 18 for D-1 and Figures 19 and 20 for D-8. This data is summarized in Tables VI and VII.

Values of $\bar{T} - \bar{T}_o$ and $\bar{T}' - \bar{T}_o'$ taken at the same pulse height (and thus the same $\overline{\left(\frac{1}{v_1}\right)}$) were substituted into (22) to calculate T_{SHIFT} as a function of pulse height. The results are plotted in Figure 21 for D-1 and Figure 22 for D-8.

The unusual shape for the trigger shift with detector D-8 is probably due to the fact that the rise time of the pulse is decreasing as the energy decreases (see Section III-B3). This tends to counteract the trigger shift caused by the decrease in the pulse magnitude towards the triggering level of the time pickoff unit.

9. Calibration of Absorbers for Rise Time Measurements

The energy of Cf^{252} fission fragments after passing

TABLE VI

Results of the Observations of $\overline{T}' - \overline{T}_o'$ with Detector D-1 ($D_1' = 1.34$ cm.)

"Mylar" Thickness (mils)	$\overline{T}'$ (nanosec.)	$\pm$	$\overline{T}'-\overline{T}_o'$ (nanosec.)	$\pm$	$\overline{PH}$ (arbitrary)	$\pm$	Frag. Type
0.0	21.40	0.05	0.0		3.93	0.02	H
0.15	20.87	0.06	0.53	0.08	2.17	0.02	H
0.25	19.58	0.06	1.82	0.08	1.04	0.03	H
0.30	19.24	0.08	2.16	0.09	0.94	0.03	H
0.35	17.56	0.10	3.84	0.11	0.54	0.02	H
0.40	16.79	0.10	4.61	0.11	0.43	0.02	H
0.45	16.76	0.13	4.64	0.14	0.41	0.01	H
0.50	15.05	0.26	6.35	0.26	0.16	0.01	H
0.0	22.50	0.04	0.0		5.52	0.02	L
0.15	22.33	0.05	0.17	0.06	3.50	0.02	L
0.25	21.40	0.06	1.10	0.07	1.87	0.03	L
0.30	21.24	0.05	2.82	0.10	1.70	0.03	L
0.35	20.30	0.07	2.20	0.08	1.01	0.02	L
0.40	19.68	0.09	2.82	0.10	0.82	0.02	L
0.45	19.70	0.09	2.80	0.10	0.77	0.01	L
0.50	17.50	0.13	5.00	0.14	0.35	0.02	L

TABLE VII

Results of Observations of $\overline{T}' - \overline{T}_0'$ with Detector D-8 ($D_1' = 1.23$ cm.)

"Mylar" Thickness (mil)	$\overline{T}'$ (nanosec.)	±	$\overline{T}'-\overline{T}_0'$ (nanosec.)	±	$\overline{PH}$ (arbitrary)	±	Frag. Type
0.00	14.77	0.03	0.0		4.25	0.03	H
0.15	14.00	0.03	0.77	0.04	2.32	0.01	H
0.25	12.90	0.04	1.87	0.05	1.07	0.01	H
0.30	12.98	0.05	1.79	0.05	1.04	0.01	H
0.35	12.29	0.08	2.48	0.09	0.62	0.01	H
0.40	11.01	0.09	3.76	0.09	0.41	0.01	H
0.45	10.51	0.09	4.26	0.09	0.59	0.01	H
0.50	10.36	0.10	4.41	0.10	0.35	0.01	H
0.00	15.94	0.05	0.0		5.92	0.03	L
0.15	15.33	0.04	0.61	0.06	3.31	0.01	L
0.25	14.70	0.03	1.24	0.06	1.92	0.01	L
0.30	14.76	0.04	1.18	0.06	1.87	0.01	L
0.35	14.44	0.06	1.50	0.08	1.153	0.01	L
0.40	13.68	0.06	2.26	0.08	0.79	0.01	L
0.45	13.16	0.06	2.78	0.08	1.13	0.01	L
0.50	13.12	0.06	2.82	0.08	0.70	0.01	L

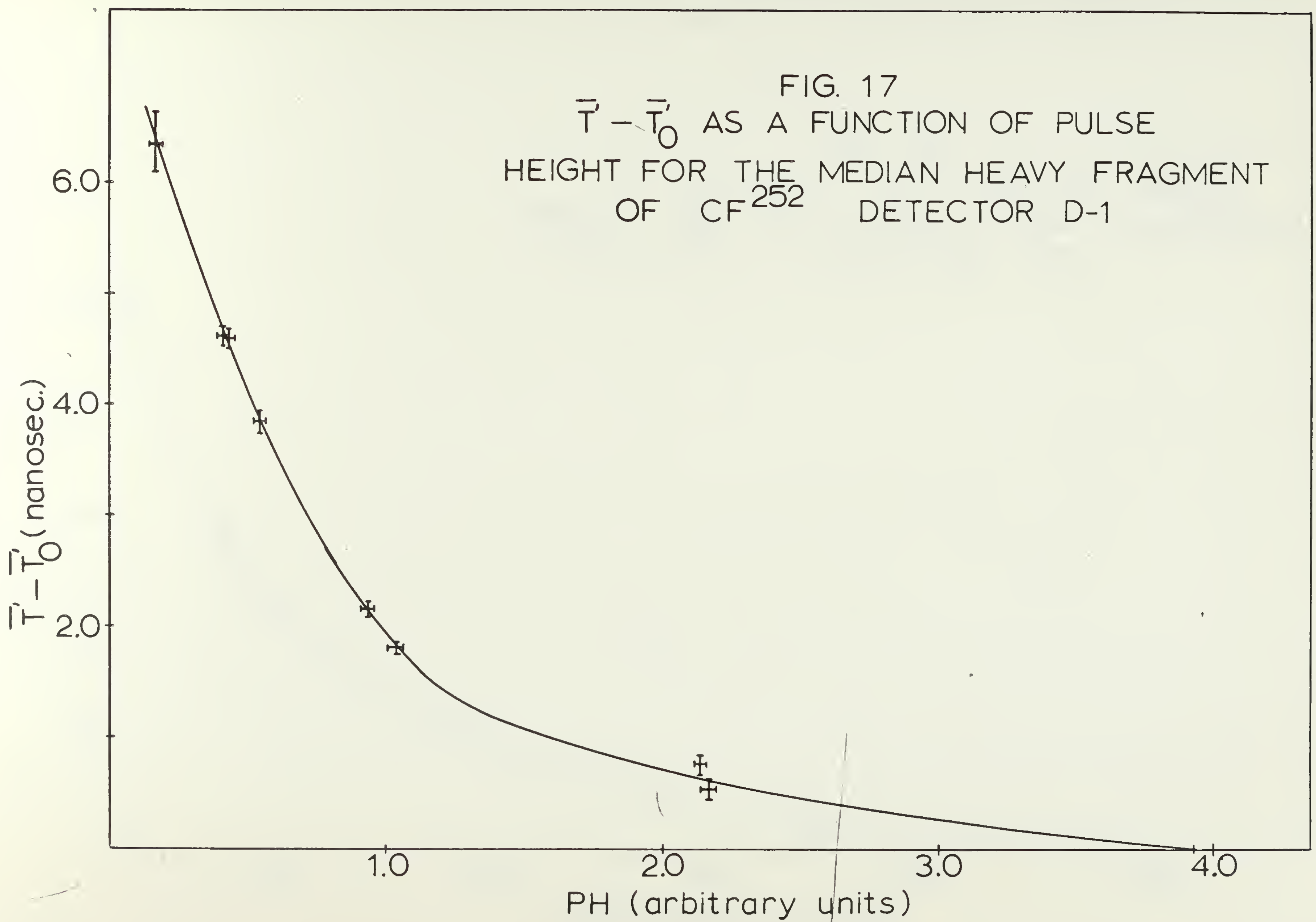
FIG. 17
$\bar{T}' - \bar{T}'_0$ AS A FUNCTION OF PULSE
HEIGHT FOR THE MEDIAN HEAVY FRAGMENT
OF CF^{252} DETECTOR D-1
6.0
4.0
2.0
1.0
2.0
3.0
4.0
PH (arbitrary units)
$\bar{T}' - \bar{T}'_0$ (nanosec.)

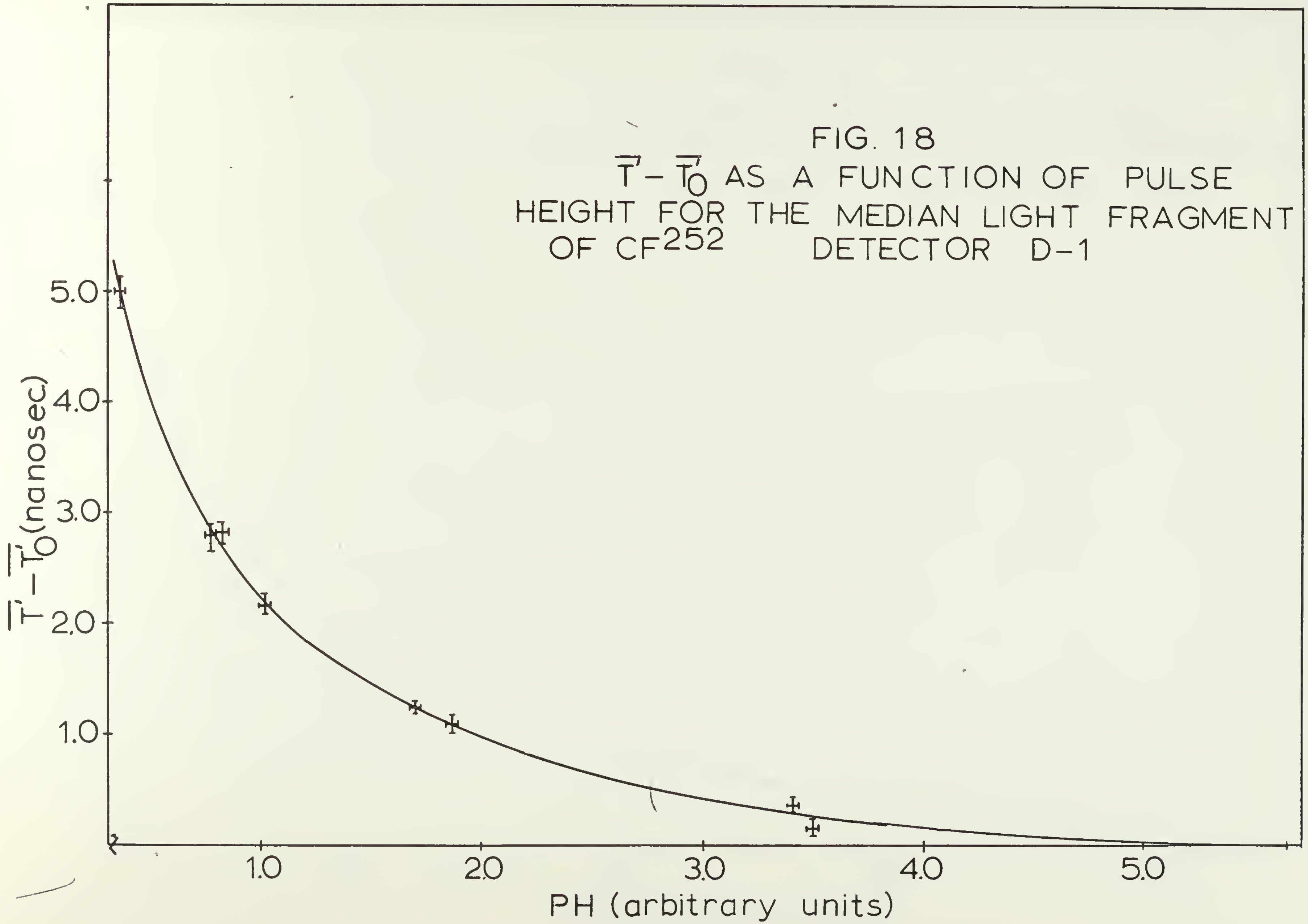

FIG. 18

$\overline{T}' - \overline{T}_0'$ AS A FUNCTION OF PULSE HEIGHT FOR THE MEDIAN LIGHT FRAGMENT OF CF^{252} DETECTOR D-1

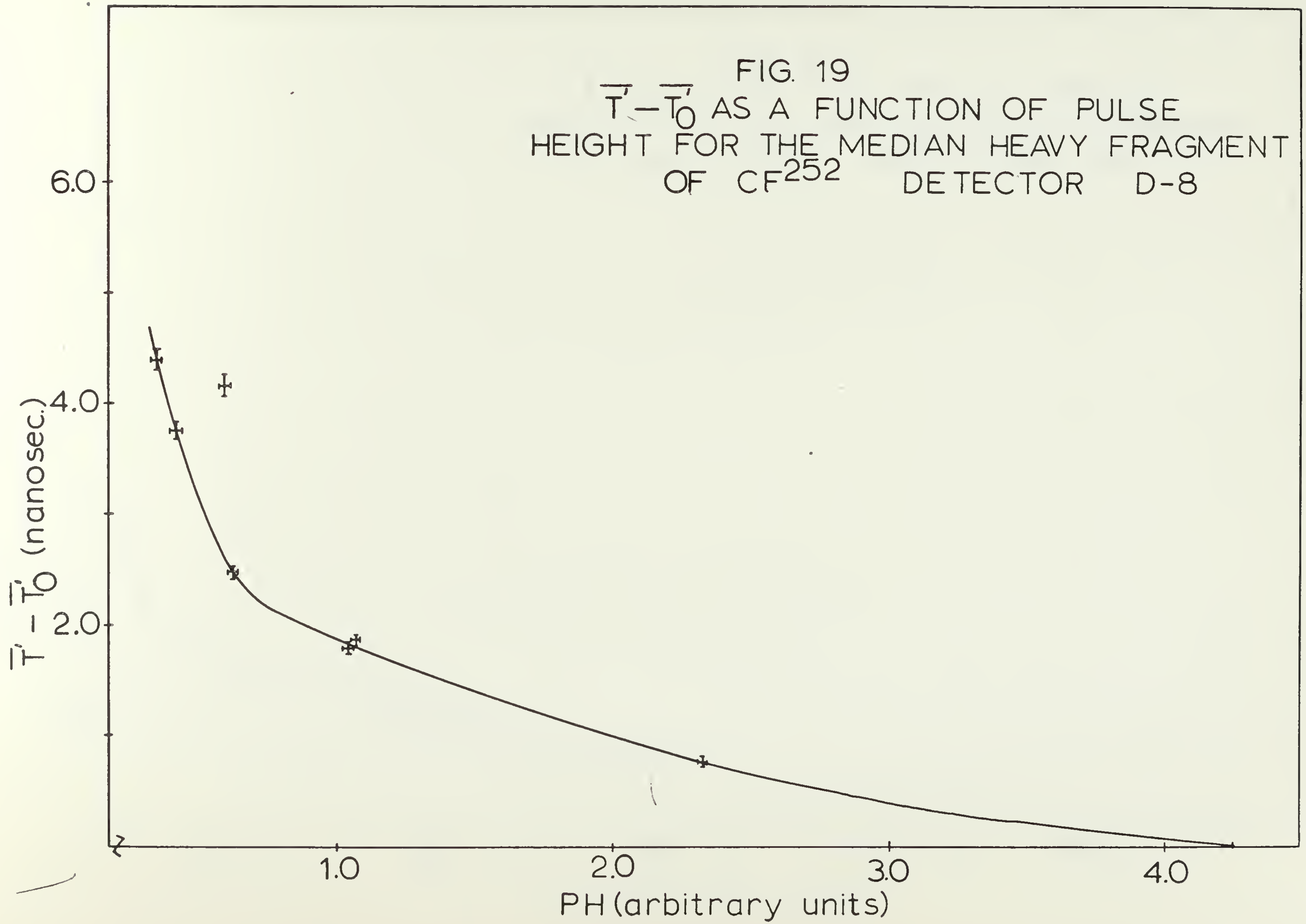

FIG. 19

$\overline{T'} - \overline{T'_0}$ AS A FUNCTION OF PULSE HEIGHT FOR THE MEDIAN HEAVY FRAGMENT OF CF^{252} DETECTOR D-8

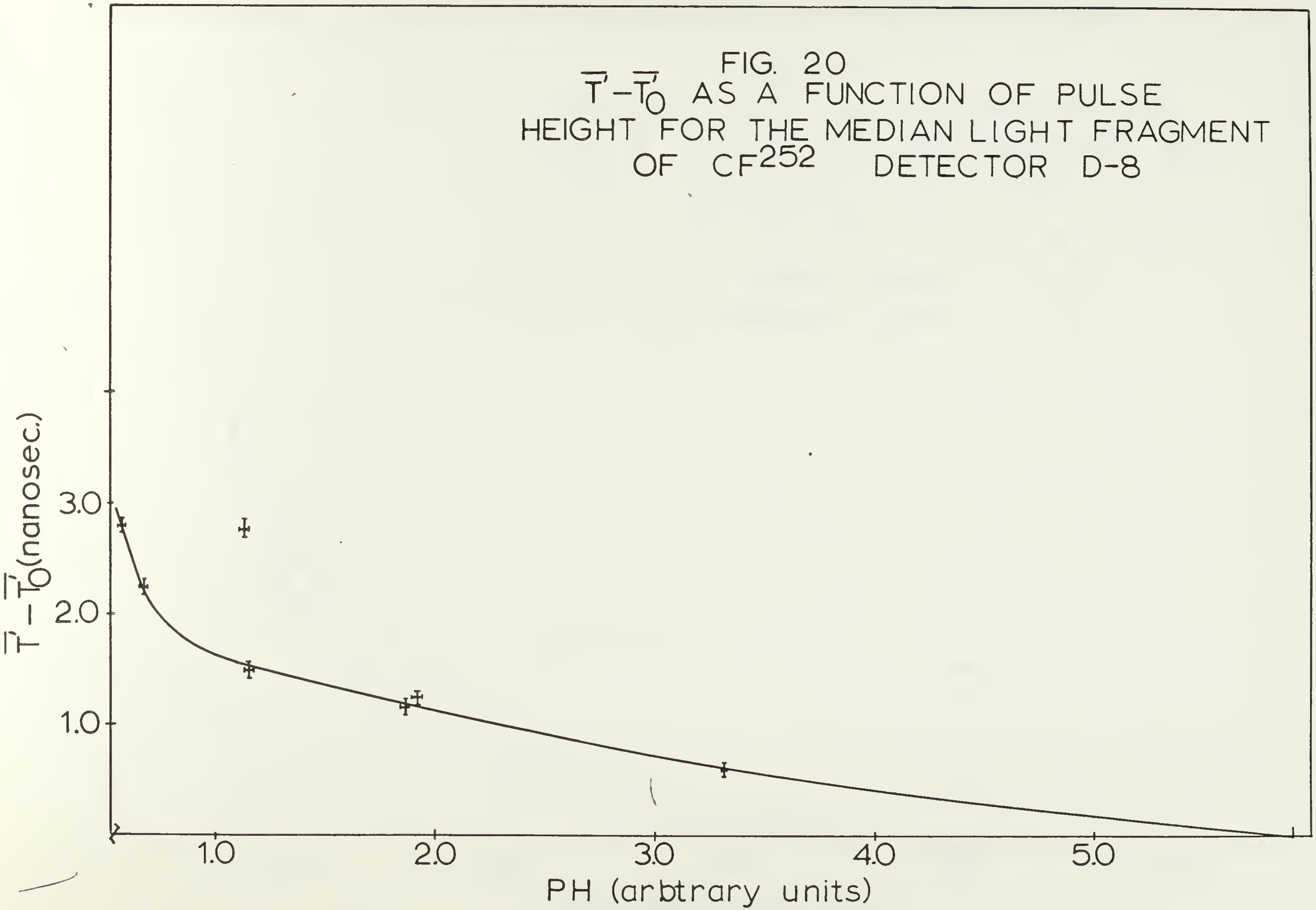

FIG. 20
$\overline{T'} - \overline{T'_0}$ AS A FUNCTION OF PULSE HEIGHT FOR THE MEDIAN LIGHT FRAGMENT OF CF^{252} DETECTOR D-8

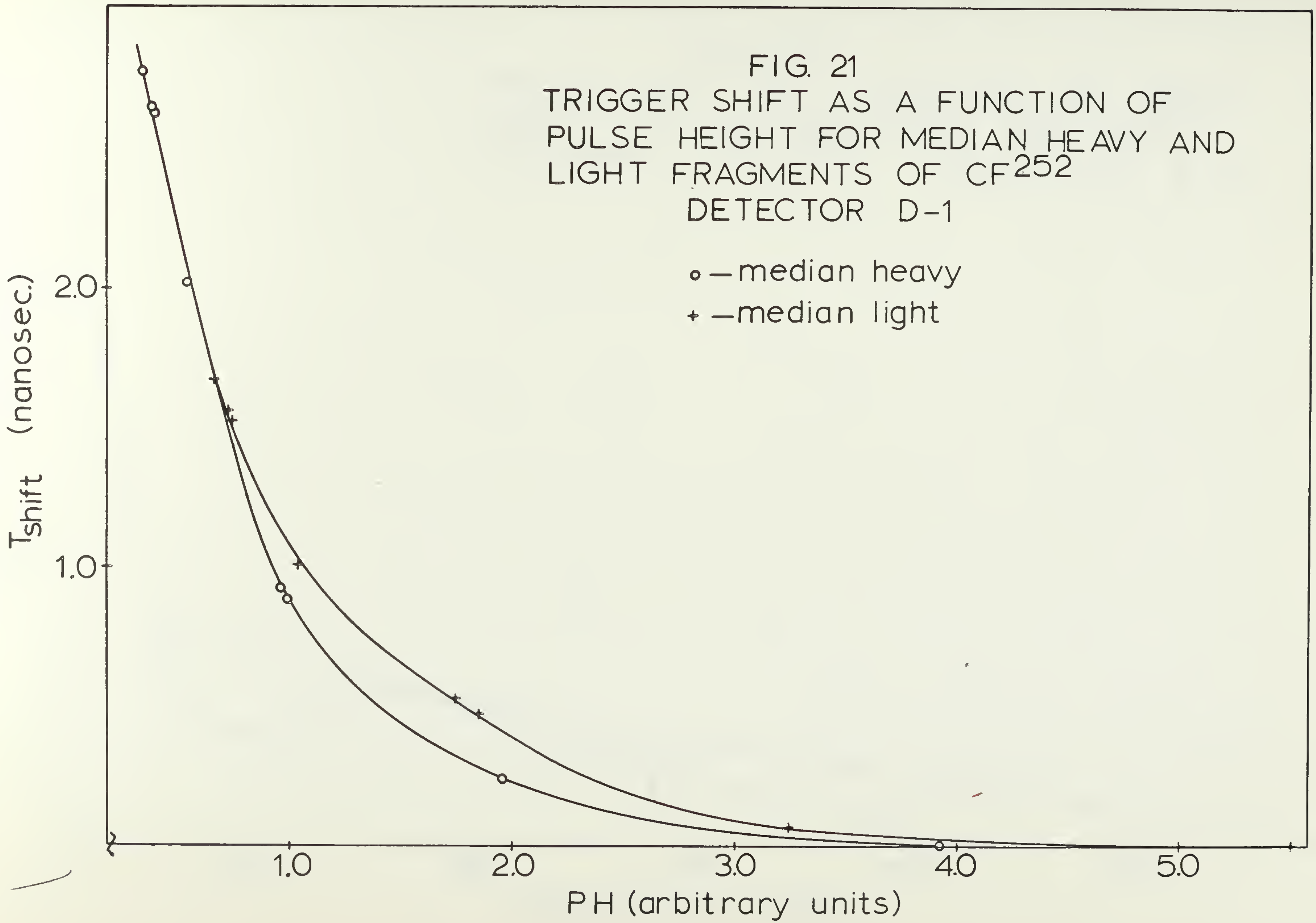

FIG. 21
TRIGGER SHIFT AS A FUNCTION OF PULSE HEIGHT FOR MEDIAN HEAVY AND LIGHT FRAGMENTS OF CF^{252}
DETECTOR D-1

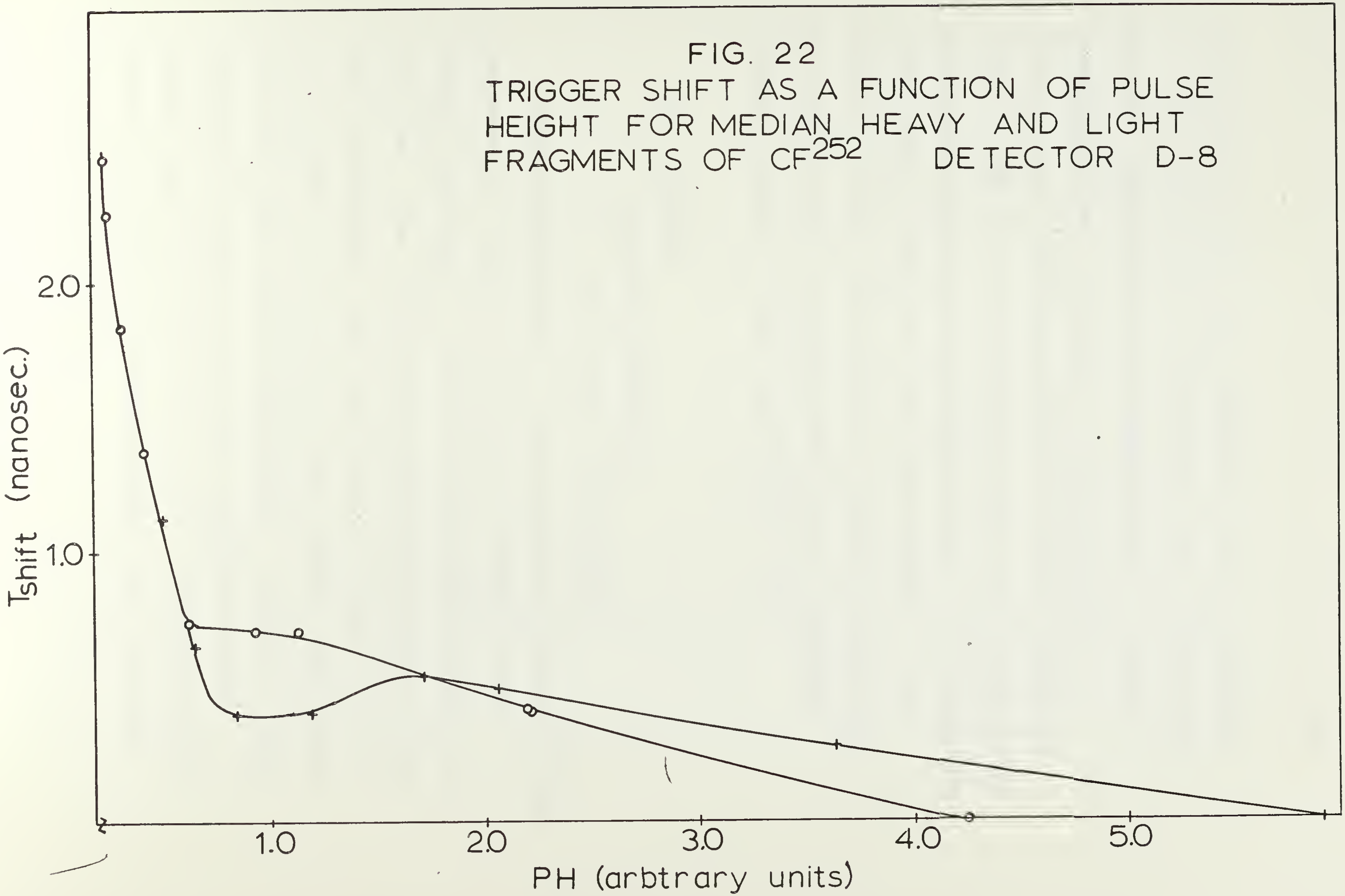

FIG. 22

TRIGGER SHIFT AS A FUNCTION OF PULSE HEIGHT FOR MEDIAN HEAVY AND LIGHT FRAGMENTS OF CF^{252} DETECTOR D-8

through each of the five permanent films (see Section II - A5) was measured experimentally with detector D-1 and D-8. The procedure and calculations for these measurements were identical to those described in Section II-D1a and Section III-A1. With the resulting values of $\overline{PH}$ and the calibration curves for the detectors (see Section III-A3), the average energy of the fragments after passing through the films was obtained. The results of these observations are listed in Table VIII. The energy values determined with the two different detectors agree to within experimental error.

D. Procedure

1. Detector Calibration

(a) Pulse Height Observations

Paired measurements of pulse height and time-of-flight were made with various thicknesses of "Mylar" film covering the source on the side facing the detector to be calibrated. The procedure was identical for each of the "Mylar" absorbers. With the absorber in place the cell was evacuated to 0.01 mm Hg or less and the electronics set up for pulse height observations. A series of runs consisted of observing the light and heavy fission fragment peaks separately with several different window widths on the single channel analyzer, which analyzed the output of detector #2.

TABLE VIII

Results of Energy Calibration of Films for Rise Time Measurements

Film	Fragment	Detector D-1 PH	Detector D-1 E	Detector D-8 PH	Detector D-8 E
15-1	Light	3.53	67.2	3.79	67.0
15-1	Heavy	2.31	47.5	2.55	48.7
25-1	Light	1.93	39.0	2.05	39.0
25-1	Heavy	1.17	27.0	1.24	27.0
30-1	Light	1.53	32.2	1.64	32.0
30-1	Heavy	0.91	22.0	0.97	21.7
35-1	Light	1.08	23.7	1.18	24.0
35-1	Heavy	0.62	16.2	0.68	16.0
40-1	Light	0.70	16.4	0.77	16.5
40-1	Heavy	0.40	11.5	0.43	11.0

Prior to each run the pressure and temperature of the vacuum system was recorded and the amplifier gain of the electronic system was adjusted to bring the fission fragment pulses from the detector within the range of the multichannel analyzer. No further adjustments were made during the run.

To start a run, the detector was disconnected from preamp #1 and the mercury pulser connected to the pulser input of the preamp. The pulser was operated at 120 pps and about ten pulser peaks were stored into the analyzer with a counting time of 30 seconds for each one. The pulse height setting of the pulser was recorded for each peak. The range of pulse heights was chosen to overlap the expected range of fission fragment pulses.

While the contents of the analyzer memory was transferred to punched cards the pulser was connected to preamp #2 and the window of the single channel analyzer set as described in section II-C4. This completed, the pulser was disconnected, the detectors connected and the fission fragment run started.

The fission fragment run counting time varied between one and two hours depending on the coincidence rate. This rate was between 40 and 100 cpm. The coincidence rate increased with an increase in window width and decreased somewhat with increasing "Mylar" film thickness, presumbaly because of scattering.

At the conclusion of the fission fragment run the

contents of the memory were transferred to punched cards and then a second pulser run was made. The procedures here were the same as that described above except that the pulse height settings of the pulser were selected to fall in between those of the first pulser run.

(b) Time-of-Flight Observations

The electronic system was set up as shown in Figure 3. Before each run the cell pressure and temperature were observed and recorded. With the detectors disconnected and the mercury pulser triggering the time pickoff units at 120 pps, a series of peaks was observed by varying the time difference between the start and stop pulses with the delay box. Storage at each delay setting was for 30 seconds. The range of delays was chosen to overlap the expected fission fragment flight times.

Upon completion of the delay box run, the window of the single channel analyzer was set, matching the time-of-flight run with a pulse height run done with the same window width and absorber.

This completed, the fission fragment run was started and just as in the pulse height case, the counting time depended upon the coincidence rate. The coincidence rate for time-of-flight runs was within a few per cent of the rate for pulse height runs done under the same conditions.

Finally, a second delay box run was made, identical to the first. When a whole group of time-of-flight runs were made sequentially, this second delay box run served

as the initial delay box run for the following fission fragment run.

The procedure described above was followed for the determination of the trigger shift of the timing system at the reduced path length D_1' (cf. Section III-1b). The only change was to reduce the counting time to a few minutes because of the much higher coincidence rate at the short path length.

2. Rise Time Observations

The procedure for the rise time measurements was first to adjust the display of the oscilliscope to display the pulses from the detector. The analysis of the data required that the display include a significant portion of the base line to establish the zero point and a portion of the pulse tail to establish the maximum point. With the display set, the time scale of the multichannel analyzer was established in nanoseconds/channel by making a series of observations of pulses from the pulser with various delays introduced by the delay box. The pulser was operated at about 100 cps and data was collected for one minute at each delay setting.

With that completed, the observations of fission fragments commenced. One type of experiment was to observe the rise time of the detector pulses with no coincidence requirement. Observations were made at bias voltages between 50 - 250 volts at each different

absorber thickness. After completing the series of experiments on a single detector the time scale was checked again with the pulser and delay box. It was found that the scale drifted less than 2.0%. The counting time in the above experiments varied between two and twenty minutes for each individual observation. The longer times correspond to low energy and low bias voltage observations with a greater signal to noise ratio.

A second type of experiment was attempted whereby the median light and median heavy fragments could be observed separately with the coincidence circuit in operation. It was found that in the coincidence mode, smoothing of the average pulse in the multichannel analyzer was not as good as in the non-coincidence mode and therefore individual observations took a good deal longer. In fact, it was found that in the coincidence mode smoothing comparable with the non-coincidence mode was not obtainable. This indicated a basic imperfection in the coincidence circuit. In view of the long time required for the coincidence experiments the time scale was checked after each individual observation.

III. Results and Analysis

A. Pulse Height and Time-of-Flight

1. Analysis of Data

The raw experimental data were the form of punched cards listing the number of counts stored in each channel of the multichannel analyzer. All subsequent calculations were performed on a digital computer.

The experimental data observed for various absorber thicknesses were used to calculate a set of points, $(\overline{PH}, \overline{E})$, for both median light and median heavy fission fragments. A smooth curve was drawn through these points yielding the desired calibration curve for the detector.

The calculation of $\overline{PH}$ involved the computation of the first moment of the observed fission fragment pulse height spectrum and expressing the result in pulse height units. The first moment was obtained from the simple expression

$$\overline{X} = \frac{\sum N(X)X}{\sum N(X)} \qquad (23)$$

Here, $X \equiv$ channel number
$N(X) \equiv$ number of counts in channel x.

The summation was carried out over the entire spectrum.

A linear relation between pulse height and channel number was computed from the observation of mercury pulser peaks corresponding to selected pulse height settings on the pulser. These pulser observations were made before and after each fission fragment run to minimize

the effect of drift. The average channel number of each pulser peak was calculated from equation (23). In this case the summation was taken over each peak individually. These observations of $(PH_i, \overline{X}_i)$ of k different pulser peaks were fit to the linear model

$$\overline{X} = B \cdot PH + C \tag{24}$$

by the method of least squares, in which case (B3)

$$B = \frac{\sum_{i=1}^{k} (PH_i - \overline{PH})\, \overline{X}_i}{\sum_{i=1}^{k} (PH_i - \overline{PH})^2} \tag{25}$$

$$C = \frac{\sum_{i=1}^{k} \overline{X}_i}{k} - B \cdot \frac{\sum_{i=1}^{k} PH_i}{k} \tag{26}$$

Equation (24) was inverted to give

$$PH = (\overline{X} - C)/B \tag{27}$$

and the $\overline{X}$ calculated from the fission fragment spectrum substituted in to give a prediction of $\overline{PH}$ for that particular observation. The uncertainty of the prediction was calculated from an expression given by Brownlee (B3)

$$\delta(\overline{PH}) = \pm\frac{ts}{|B|}\left[1 + 1/k + \frac{\overline{X} - A}{B^2 \sum_i (PH_i - \overline{PH})^2}\right]^{\frac{1}{2}} \tag{28}$$

where t is Student's t for (k-2) degrees of freedom and S is the variance estimate.

There is an additional uncertainty in $\overline{PH}$ due to the fact that only a finite number of events were observed. Therefore, the true value of $\overline{X}$ is only known to within $\pm \frac{1.96\, \sigma(x)}{\sqrt{N}}$. N, the total number of events observed,

was in all cases greater than 2500 events. The total uncertainty in $\overline{PH}$ is

$$\delta(\overline{PH})_{TOTAL} = \left[\delta(\overline{PH})^2 + \left(\frac{1.96\ \sigma(X)}{B\ \sqrt{N}}\right)^2 \right]^{\frac{1}{2}} . \quad (29)$$

In all cases this uncertainty was less than 0.03 pulse height units, corresponding to 0.5 MeV.

Energy values were calculated from the time-of-flight data from the approximate expression

$$\overline{E} = 0.518\ \overline{A}\ \overline{V^2} \ . \quad (30)$$

$\overline{E}$ is the average energy in MeV; $\overline{A}$ is the average mass in amu and $\overline{V}^2$ is the average square velocity in $(\text{cm/nanosec.})^2$.

For the median light fragment $\overline{A} = 106.0$ and for the median heavy fragment $\overline{A} = 141.9$. These are the post neutron emission masses observed by Schmitt, Kiker and Williams (S3). It was appropriate to use the post neutron emission values since neutron emission occurs within 4×10^{-14} secs of fission (F1) and therefore, the energy of the particle striking the detector is that associated with the post neutron emission mass.

The quantity $\overline{V}^2$ was calculated from the observed time-of-flight spectrum as follows. The first moment of the spectrum was computed from (23) which gave $\overline{X}$. This was expressed in units of time via a linear relation between time and channel number calculated from the observation of delay box peaks before and after each

fission fragment run. The calculation of the linear relation was identical to that done for the pulser runs except in this case the result was an expression

$$\overline{T} = (\overline{X} - C)/B \quad , \tag{31}$$

Substituting $\overline{X}$ from the time-of-flight spectrum gave a prediction of $\overline{T}$, the average time difference observed by the time-to-pulse-height converter. The average flight time to detector #1 over the flight path D_1 = 21.89 cm was

$$\overline{T}_1 = \overline{T} + \overline{T}_2 + T_{SHIFT} \quad . \tag{32}$$

$\overline{T}_2$ was the average flight time to detector #2 over the flight path D_2 = 2.37 cm of the sister fragments to those striking detector #1. $\overline{T}_2$ was determined from the expression

$$\overline{T}_2 \doteq D_2 \left(\overline{\frac{1}{v_2}}\right) \simeq \frac{D_2}{\overline{v}_2} \left\{ 1 + \left[\frac{\sigma(v_2)}{\overline{v}_2} \right]^2 \right\} \quad . \tag{33}$$

$\overline{V}_2$ was known from the calculation of energy loss within the source and $\sigma(V_2)$ was taken from the results of Schmitt et al (S3). For a heavy fragment striking detector #1: $\overline{V}_2$ = 1.342 cm/nanosec., $\sigma(V_2)$ = 0.0693 cm/nanosec., and $\overline{T}_2$ = 1.76 nanosec. For a light fragment striking detector #1: $\overline{V}_2$ = 1.007 cm/nanosec., $\sigma(V_2)$ = 0.0831 cm/nanosec., and $\overline{T}_2$ = 2.37 nanosec.

T_{SHIFT} was the correction for trigger shift as the fragments were degraded. This was calculated for the $\overline{PH}$

corresponding to the particular time-of-flight run being analyzed as described in Section III-A1.

In addition to $\bar{T}_1$, the standard deviation of T_1, $\sigma(T_1)$, was required for the calculation of $\overline{V_1^2}$.

$$\sigma^2(T_1) = \sigma^2(T) + \sigma^2(T_2) + 2\rho(T,T_2)\sigma(T)\sigma(T_2) \tag{34}$$

$\rho(T, T_2)$ is the correlation coefficient between T and T_2. This quantity was estimated from the velocity data of Milton and Fraser (M4) as $\rho(T, T_2) = 0.5$. - (T) came directly from the observed time spectrum and $\sigma^2(T_2)$ was calculated from $\sigma^2(T_2) = \left(\frac{D_2}{\bar{V}_2^2}\right)^2 \sigma^2(v_2)$ using the values of $\bar{V}_2$ and $\sigma(V_2)$ given above.

In order to calculate $\overline{V_1^2}$ the expression for V_1^2 was expanded in a Taylor series about $\bar{T}_1$

$$v_1^2 = \frac{D_1^2}{T_1^2} = D_1^2\left[\frac{1}{\bar{T}_1^2} - \frac{2}{\bar{T}_1^3}(T_1 - \bar{T}_1) + 3\frac{(T_1-\bar{T}_1)^2}{\bar{T}_1^4} - \cdots\right]. \tag{35}$$

Keeping terms to the second order and taking the average of both sides yielded

$$\overline{v_1^2} = \frac{D_1^2}{\bar{T}_1^2}\left[1 + 3\left(\frac{\sigma(T_1)}{\bar{T}_1}\right)^2\right] \tag{36}$$

The values of $\bar{T}_1$ and $\sigma(T_1)$ obtained above were substituted into this expression to give $\overline{V_1^2}$ which in turn was substituted into equation (30) to give the average energy, $\bar{E}$.

Starting with equation (30) the uncertainty in energy

was calculated.

$$\delta^2(E) = \left|\frac{\partial E}{\partial \bar{v}_2}\right|^2 \delta^2(\overline{v_2^2}) + \left|\frac{\partial E}{\partial A}\right|^2 \delta^2(A)$$

$$\delta E = \left\{\left[0.518A\right]^2 \delta^2 (\overline{v_1^2}) + \left[0.518\ \overline{v_1^2}\right]^2 \delta^2 (A)\right\}^{\frac{1}{2}} \tag{37}$$

$\delta(A) \approx \pm 0.4$ amu (S3) and $\delta(\overline{V_1^2})$ was calculated.

$$\delta^2(\overline{v_1^2}) = \left|\frac{\partial \overline{v_1^2}}{\partial \bar{T}_1}\right|^2 \delta^2(\bar{T}_1) + \left|\frac{\partial \overline{v_1^2}}{\partial \sigma}\right|^2 \delta^2(\sigma) \tag{38}$$

$$\delta^2(\overline{v_1^2}) = \left\{2D_1^2\left[1+6\left(\frac{\sigma(T_1)}{\bar{T}_1}\right)^2\right](\bar{T}_1)^{-3}\right\}^2 \delta^2(T_1) + \left\{\frac{6D_1\sigma(T_1)}{\bar{T}_1^2}\right\}^2 \delta^2(\sigma(T_1)).$$

$\delta(\sigma(T_1))$ was obtained from equation (34) by setting $\rho(T, T_2)$ at the extreme limits of 0 and $+1$. The uncertainty in T_1 was calculated.

$$\delta^2(\bar{T}_1) = \delta^2(\bar{T})_{TOTAL} + \delta^2(\bar{T}_2) + \delta^2(T_{SHIFT}). \tag{39}$$

It was estimated that $\delta(\bar{T}_2) = 0.01$ nanosec. and $\delta(T_{SHIFT}) = 0.1$ nanosec. while the calculation of $\delta(\bar{T})_{TOTAL}$ was identical to that done previously for $\delta(\overline{PH})_{TOTAL}$ (cf. equation 29) with the addition of an extra term for the uncertainty of the time scale.

2. Average Mass Approximation

The average energy was calculated from

$$\bar{E} = 0.518\ \bar{A}\ \ \overline{v^2} \tag{40}$$

which is an approximation to the correct expression

$$\bar{E} = 0.518\ (\overline{Av^2}) \tag{41}$$

It can be established from the data of Schmitt (S3), Whetstone (W1), and Milton and Fraser (M4) that for undegraded fission fragments, equation (40) gives the correct values of energy for the median light and median heavy fragments to within $\pm$ 1.0 MeV.

This agreement can be explained by rewriting equation (40) and (41) as sums and comparing them term by term. Equation (40) becomes

$$\bar{E} = 0.518\ \bar{A}\ \frac{\sum_i v_i^2\ N(v_i)}{N_T} \tag{42}$$

and (41) becomes

$$\bar{E} = 0.518\ \frac{\sum \bar{A}\ (v_i)\ v_i^2\ N(v_i)}{N_T} \tag{43}$$

$N(v_i)$ is the discrete frequency distribution of the velocity as observed with a multichannel analyzer; N_T is the total number of observed events and $\bar{A}(v_i)$ is the average mass of the fission fragments for a given velocity v_i. These two equations can be subtracted to give

$$\Delta\bar{E} = 0.518\ \frac{\sum_i \left[\bar{A} - \bar{A}(v_i)\right] v_i^2\ N(v_i)}{N_T} \tag{44}$$

Figures 23 and 24 show $\bar{A}(v)$ for the light and heavy fragments respectively. These curves were calculated from

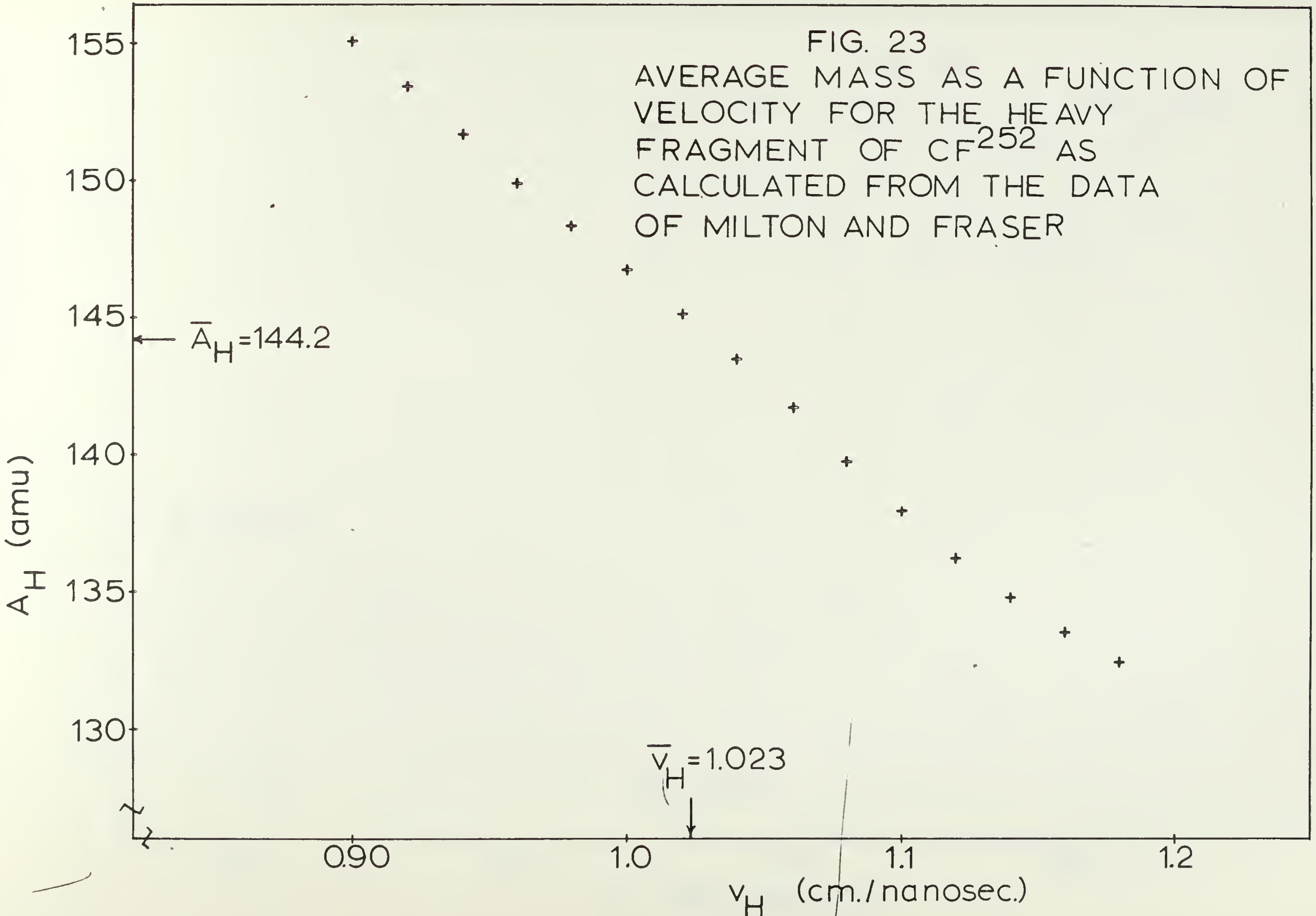

FIG. 23
AVERAGE MASS AS A FUNCTION OF VELOCITY FOR THE HEAVY FRAGMENT OF CF^{252} AS CALCULATED FROM THE DATA OF MILTON AND FRASER

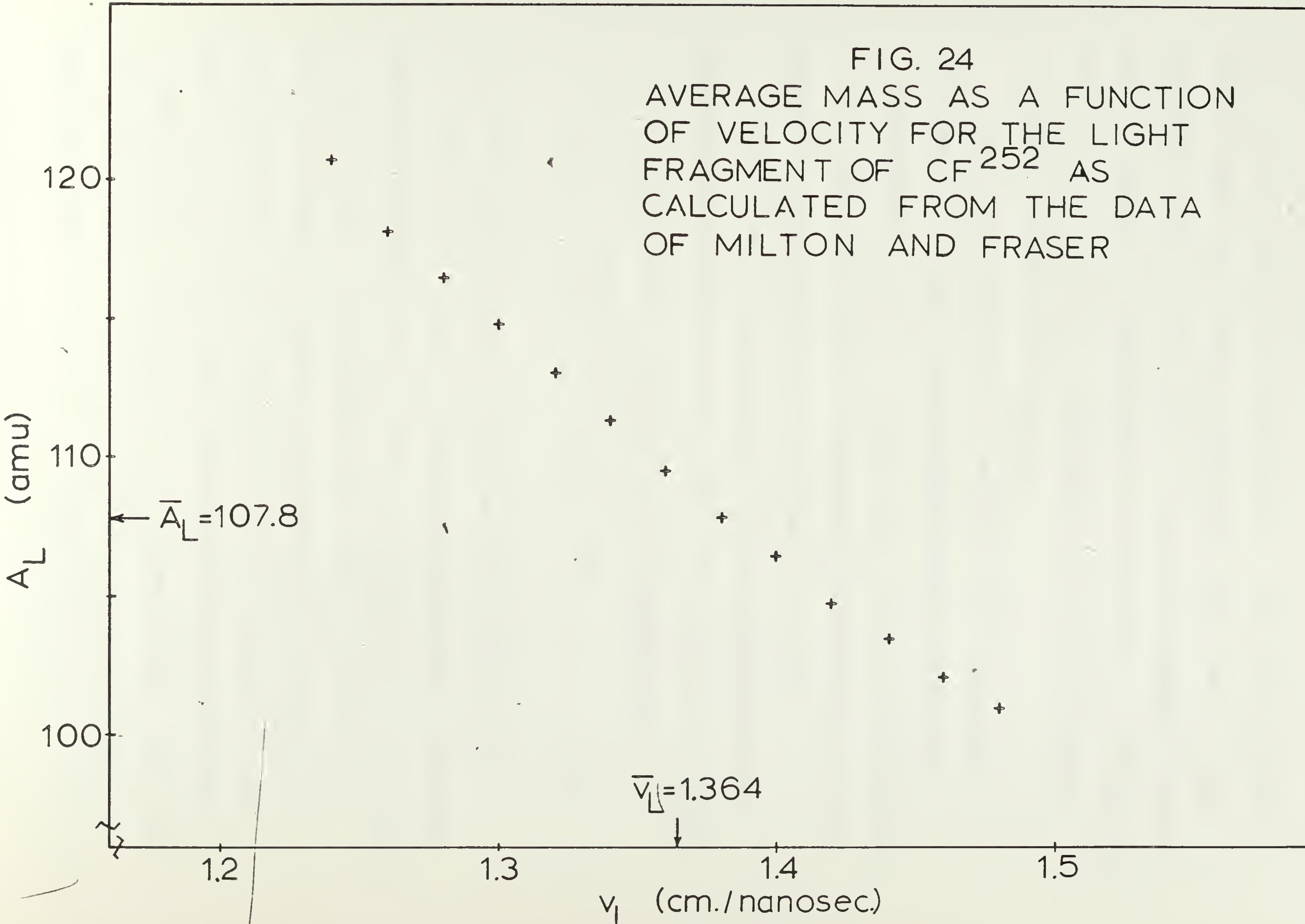

FIG. 24
AVERAGE MASS AS A FUNCTION OF VELOCITY FOR THE LIGHT FRAGMENT OF CF^{252} AS CALCULATED FROM THE DATA OF MILTON AND FRASER

the data of Milton and Fraser (M4). $\overline{A}(v)$ fits a linear model quite well over the individual mass peaks. Also $\overline{A}(\overline{v}) \approx \overline{A}$. This, along with the apparent symmetry (W1) of $N(v_1)$, results in cancellation of the terms of the opposite sign in equation (44), explaining the relatively good agreement between (40) and (41).

Of course, there is no assurance that the same agreement holds true for degraded fission fragments. It is important to note though, that $\Delta\overline{E}$ is proportional to v^2, which will tend to decrease $\delta\overline{E}$ independent of the degree of cancellation of the terms in the sum.

The degree of cancellation will be affected by the dependence of dv/dx upon the mass. The theory of Lindhard (L1) for $(dv/dx)_{elec.}$ gives the mass dependence as

$$f(A) = \frac{Z_1^{7/6}}{A\left[Z_1^{2/3} + Z_2^{2/3}\right]^{3/2}} . \qquad (45)$$

Z_1 is the atomic number of the incident particle and Z_2 is the atomic number of the stopping medium. The mass dependence implicit in Z_1 can be calculated from the theory of equal charge displacement (G1). F(A) is plotted in Figure 25 showing a smooth, relatively minor (10% over each individual peak) dependence of dv/dx upon the mass. $(dv/dx)_{nuclear} \propto \frac{Z_1^2}{A^2}$ (E1), which in the range of interest is very nearly independent of the fragment mass. For both the light and heavy fragments the variation of dv/dx over either the light or heavy peak is only about 10%. Therefore,

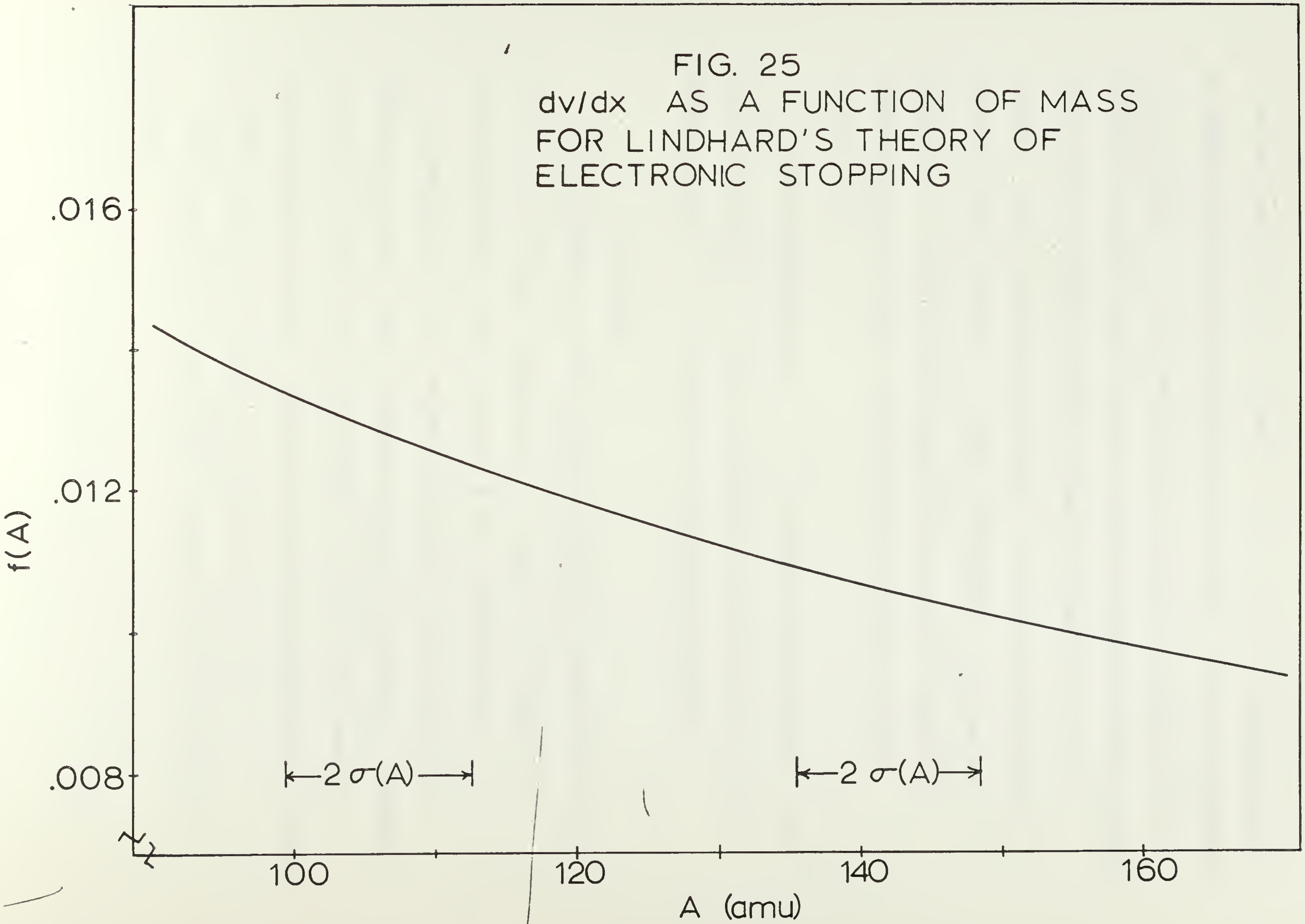

FIG. 25
dv/dx AS A FUNCTION OF MASS FOR LINDHARD'S THEORY OF ELECTRONIC STOPPING

it seems reasonable to assume that the joint distribution of mass and velocity maintains its shape as the fragments are degraded. An indication that this is indeed so is provided by the fact that the velocity spectrum for either the light or heavy fragment remains symmetrical even for the lowest energies observed. Figure 26 shows the velocity distribution of light fragments with median energy E = 11.2 MeV and Figure 27 shows the velocity distribution of heavy fragments with median energy E = 6.8 MeV.

From consideration of all of the above factors the error introduced by the average mass approximation was estimated as $\pm$ 1.0 MeV for all energies observed.

3. Results

The results of the fission fragment calibration by the time-of-flight techniques are given in Table IX for detector D-1 and in Table X for detector D-8. It is impossible to give exact confidence limits due to estimated errors (see Sections III-A2 and IIC-3), however, the errors indicated in the table probably represent 95% confidence limits. The calibration points are plotted in Figure 28 for D-1 and in Figure 29 for D-8.

The results of the alpha particle calibration for D-1 was

$$E_{\alpha} = 17.09 \text{ (PH)} \tag{46}$$

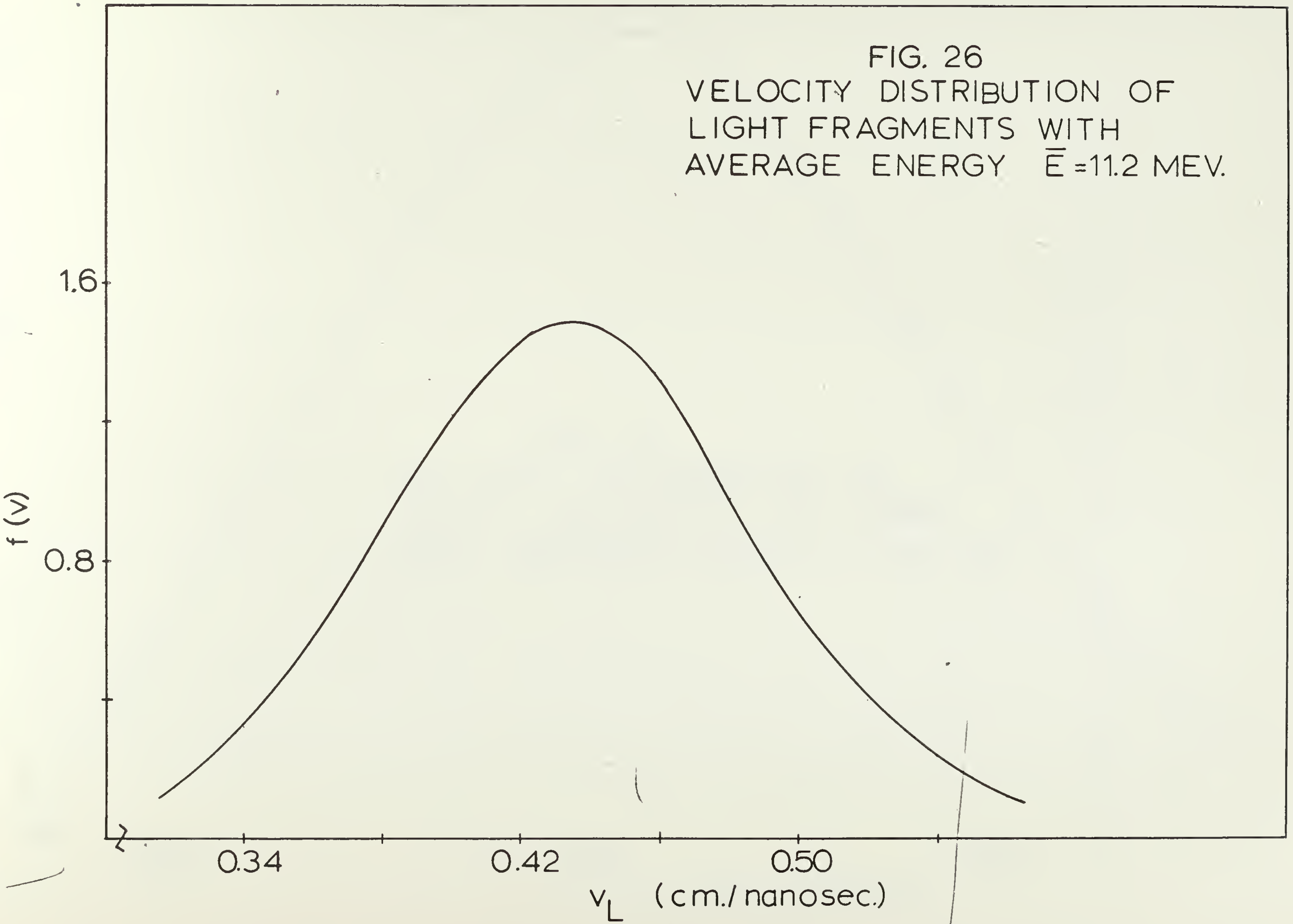

FIG. 26
VELOCITY DISTRIBUTION OF LIGHT FRAGMENTS WITH AVERAGE ENERGY $\bar{E}$ =11.2 MEV.

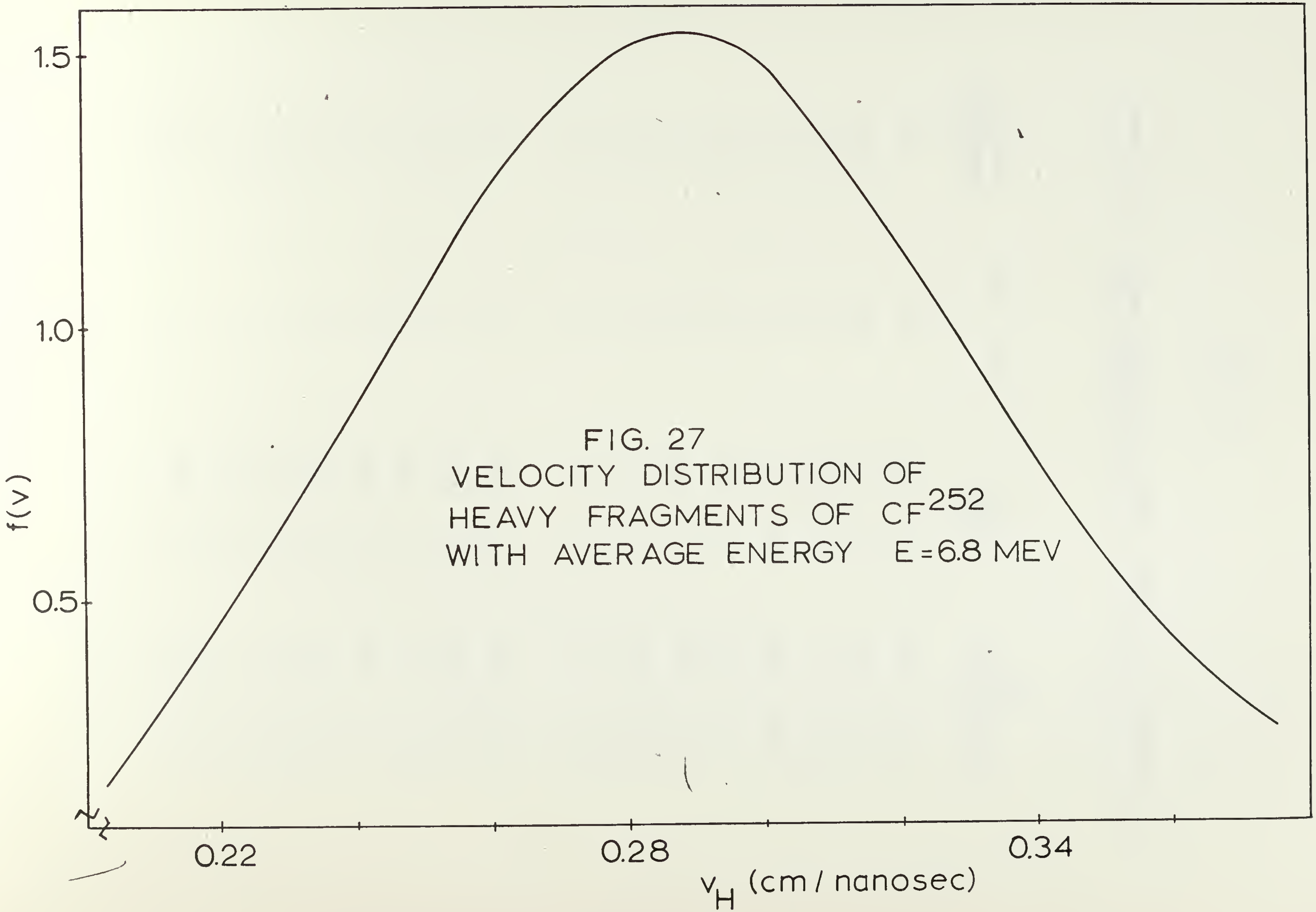

FIG. 27
VELOCITY DISTRIBUTION OF
HEAVY FRAGMENTS OF CF^252
WITH AVERAGE ENERGY E=6.8 MEV
1.5
1.0
0.5
f(v)
0.22
0.28
0.34
v_H (cm / nanosec)

TABLE IX

Results of Pulse Height and Time-of-Flight Observations with Detector D-1

"Mylar" Thickness (mil)	Frag. Type	$\overline{E}$ (MeV)	$\pm$	$\overline{PH}$ (Arbitrary)	$\pm$
0.0	H	76.8	2.3	3.93	0.02
0.15	H	41.5	1.6	1.97	0.01
0.25	H	23.8	1.2	1.00	0.02
0.30	H	23.0	1.2	0.97	0.01
0.35	H	14.3	1.1	0.55	0.01
0.40	H	11.1	1.1	0.38	0.01
0.45	H	11.2	1.1	0.38	0.00
0.50	H	10.4	1.0	0.34	0.01
0.0	L	100.5	3.1	5.52	0.02
0.15	L	61.6	2.9	3.26	0.01
0.25	L	38.1	1.5	1.86	0.02
0.30	L	36.7	1.1	1.76	0.01
0.35	L	23.0	1.2	1.05	0.01
0.40	L	17.4	1.1	0.75	0.01
0.45	L	17.5	1.1	0.73	0.01
0.50	L	16.2	1.1	0.67	0.01

TABLE X

Results of Pulse Height and Time-of-Flight Observations with Detector D-8

"Mylar" Thickness (mil)	Frag. Type	$\overline{E}$ (MeV)	$\pm$	$\overline{PH}$ (Arbitrary)	$\pm$
0.00	H	77.6	2.4	4.28	0.02
0.00	H	79.2	3.1	4.20	0.02
0.00	H	76.0	3.1	4.20	0.02
0.15	H	44.3	1.9	2.20	0.02
0.15	H	44.4	1.8	2.22	0.02
0.25	H	24.7	1.2	1.13	0.02
0.25	H	25.3	1.2	1.14	0.02
0.30	H	21.2	1.0	0.93	0.01
0.35	H	14.9	1.1	0.62	0.01
0.35	H	15.1	1.1	0.63	0.01
0.40	H	11.1	1.1	0.43	0.00
0.40	H	10.9	1.1	0.41	0.01
0.40	H	10.8	1.1	0.43	0.01
0.45	H	9.0	1.1	0.33	0.00
0.50	H	7.1	1.0	0.25	0.00
0.50	H	6.8	1.0	0.23	0.00
0.50	H	7.1	1.0	0.24	0.00
0.00	L	101.2	2.8	5.94	0.01
0.00	L	100.8	3.0	5.93	0.03
0.00	L	101.4	3.1	5.89	0.01

TABLE X continued

"Mylar" Thickness (mil)	Frag. Type	$\overline{E}$ (MeV)	$\pm$	$\overline{PH}$ (Arbitrary)	$\pm$
0.15	L	66.3	2.1	3.63	0.01
0.15	L	66.0	2.1	3.59	0.01
0.25	L	39.2	1.7	2.07	0.02
0.25	L	39.2	1.5	2.05	0.01
0.30	L	33.7	1.5	1.72	0.02
0.35	L	23.5	1.2	1.19	0.01
0.35	L	23.4	1.4	1.18	0.01
0.40	L	17.4	1.1	0.84	0.01
0.40	L	17.7	1.3	0.83	0.01
0.40	L	17.2	1.2	0.84	0.00
0.45	L	14.4	1.1	0.66	0.00
0.50	L	11.8	1.0	0.52	0.00
0.50	L	11.5	1.1	0.49	0.00
0.50	L	11.4	1.1	0.49	0.00

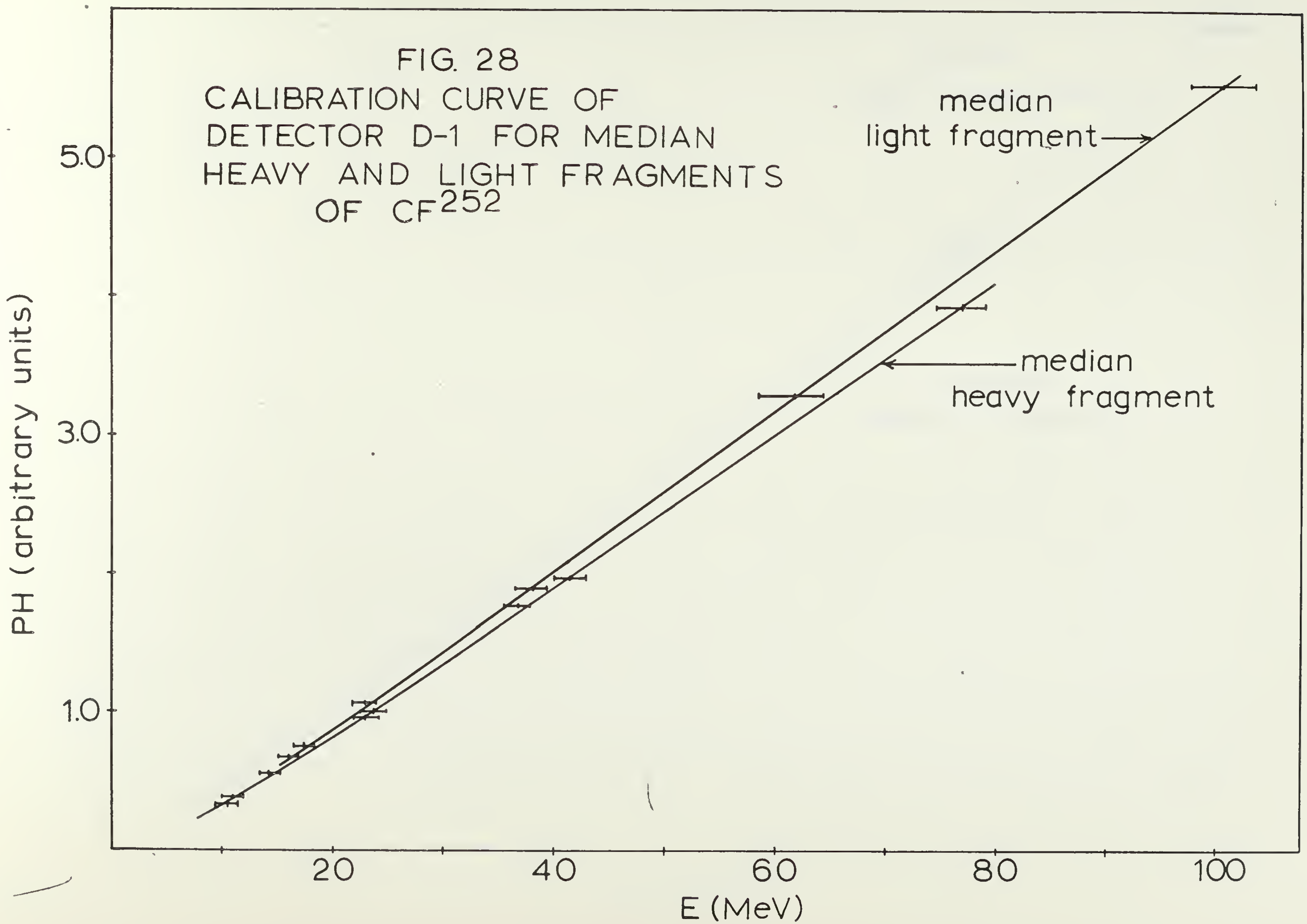

FIG. 28
CALIBRATION CURVE OF DETECTOR D-1 FOR MEDIAN HEAVY AND LIGHT FRAGMENTS OF CF^{252}

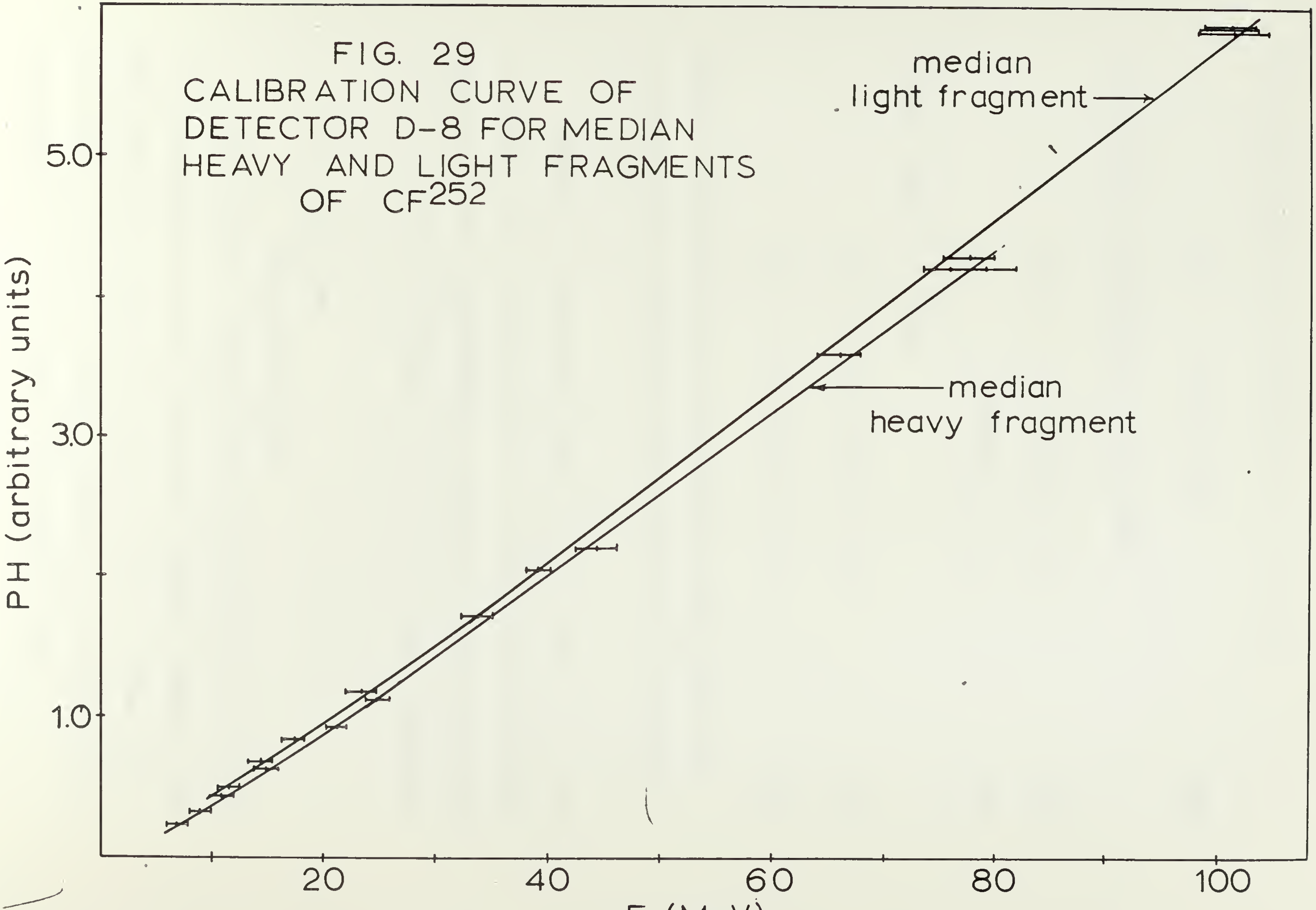
FIG. 29
CALIBRATION CURVE OF
DETECTOR D-8 FOR MEDIAN
HEAVY AND LIGHT FRAGMENTS
OF CF252
median
light fragment
median
heavy fragment
PH (arbitrary units)
5.0
3.0
1.0
20
40
60
80
100
E (MeV)

The alpha particle calibration of D-8 gave

$$E_{\alpha} = 16.19 \text{ (PH)} \qquad (47)$$

The Schmitt calibration of D-1 gave

$$E_H = 18.17 \text{ (PH)} + 6.14 \qquad (48)$$

$$E_L = 17.37 \text{ (PH)} + 5.76 \qquad (49)$$

while that of D-8 was

$$E_H = 17.05 \text{ (PH)} + 5.11 \qquad (50)$$

$$E_L = 16.29 \text{ (PH)} + 4.77 \qquad (51)$$

These calibration lines are plotted along with the time-of-flight calibration for comparison in Figures 30, 31, 32, 33.

Figure 34 shows the pulse height defect as a function of energy for both detectors. No corrections have been applied to the experimental curves for either gold film loss or field dependence of the pulse height response.

B. Rise Time

1. Analysis of Data

The data for the rise time experiments was in the form of punched cards listing the channel number X and the number of counts in channel X, N(X). These were read into a digital computer which fit the data to a polynominal by non-linear least squares (B5)

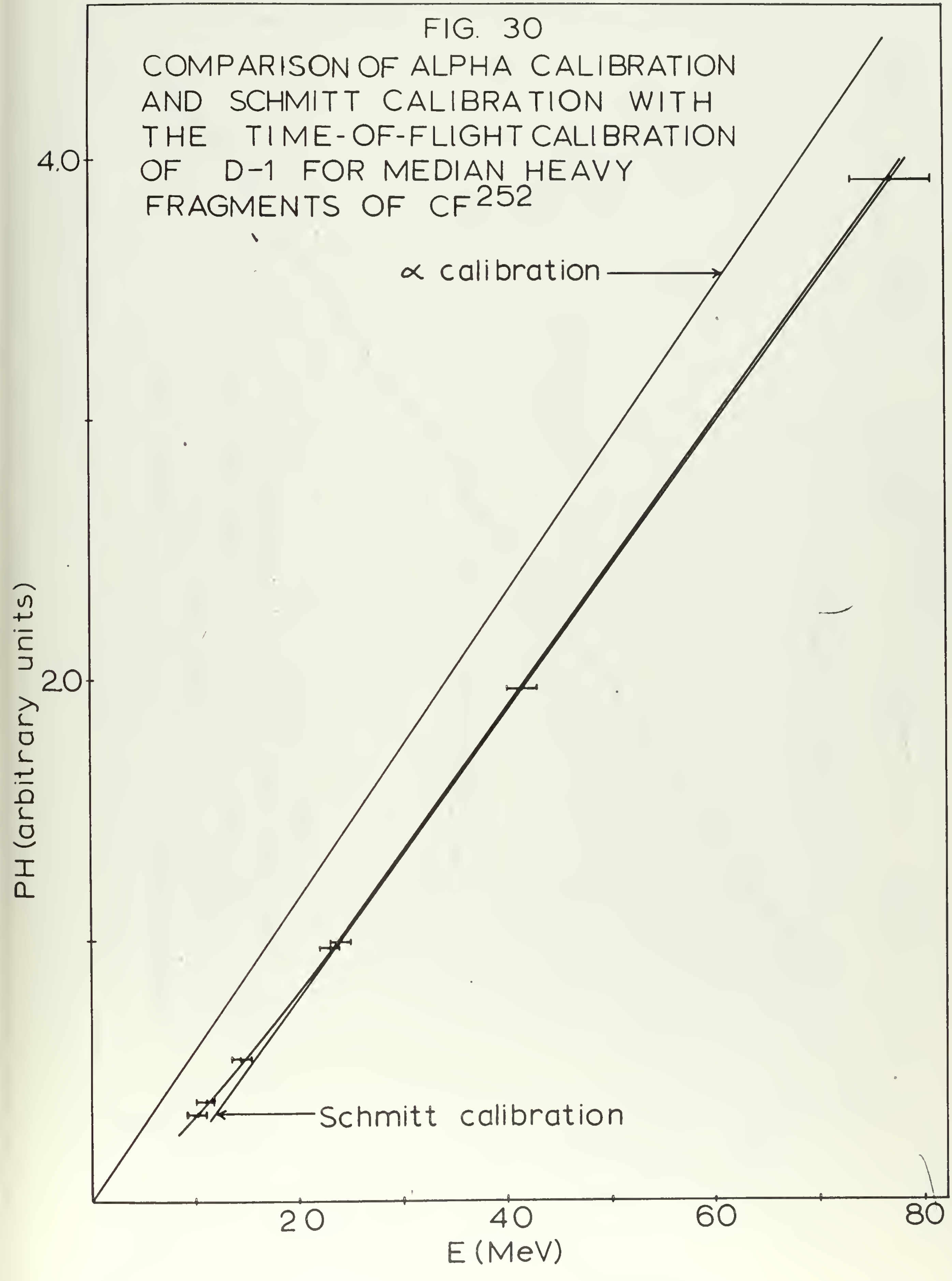

FIG. 30

COMPARISON OF ALPHA CALIBRATION AND SCHMITT CALIBRATION WITH THE TIME-OF-FLIGHT CALIBRATION OF D-1 FOR MEDIAN HEAVY FRAGMENTS OF CF^{252}

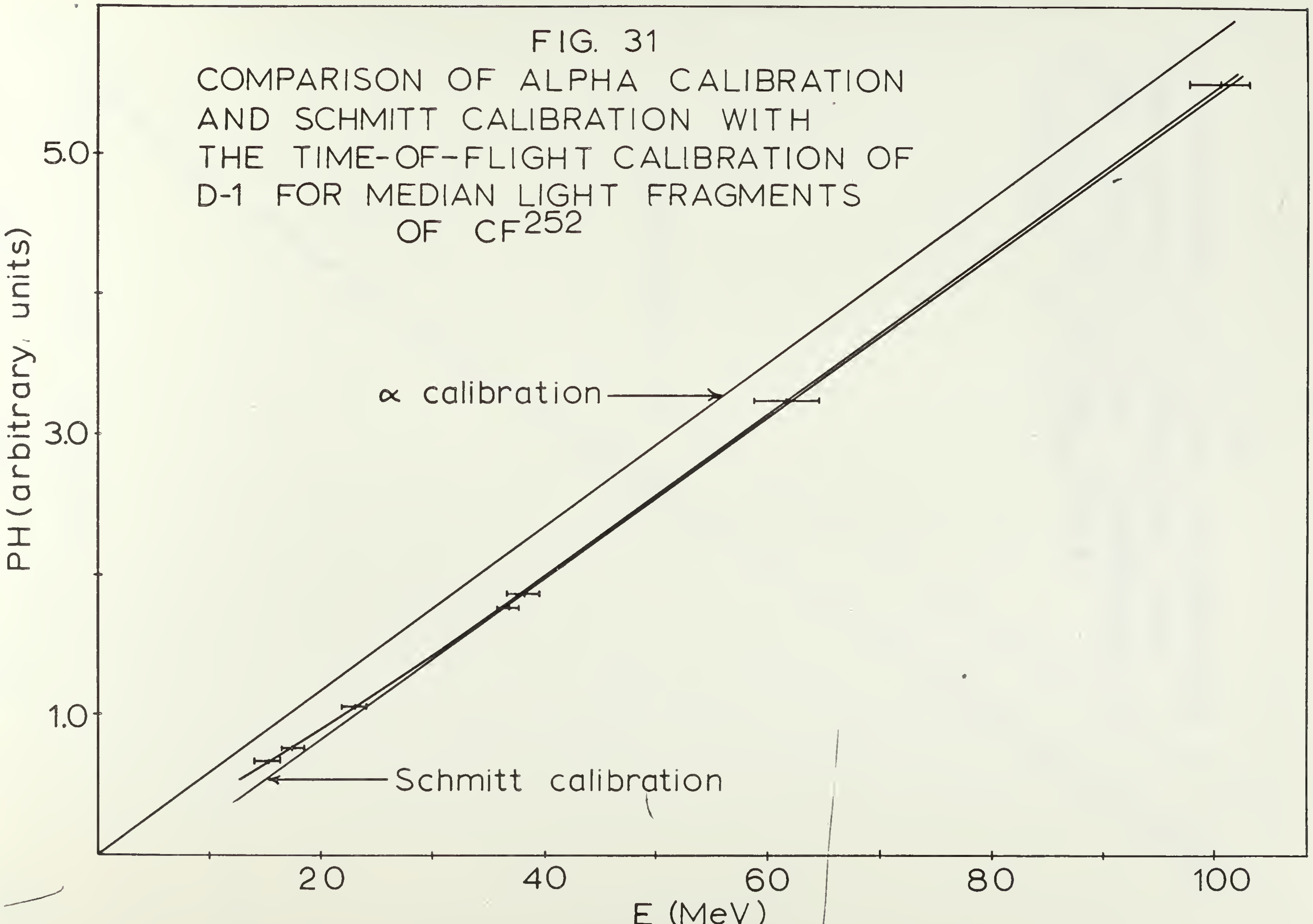

FIG. 31
COMPARISON OF ALPHA CALIBRATION AND SCHMITT CALIBRATION WITH THE TIME-OF-FLIGHT CALIBRATION OF D-1 FOR MEDIAN LIGHT FRAGMENTS OF CF^{252}

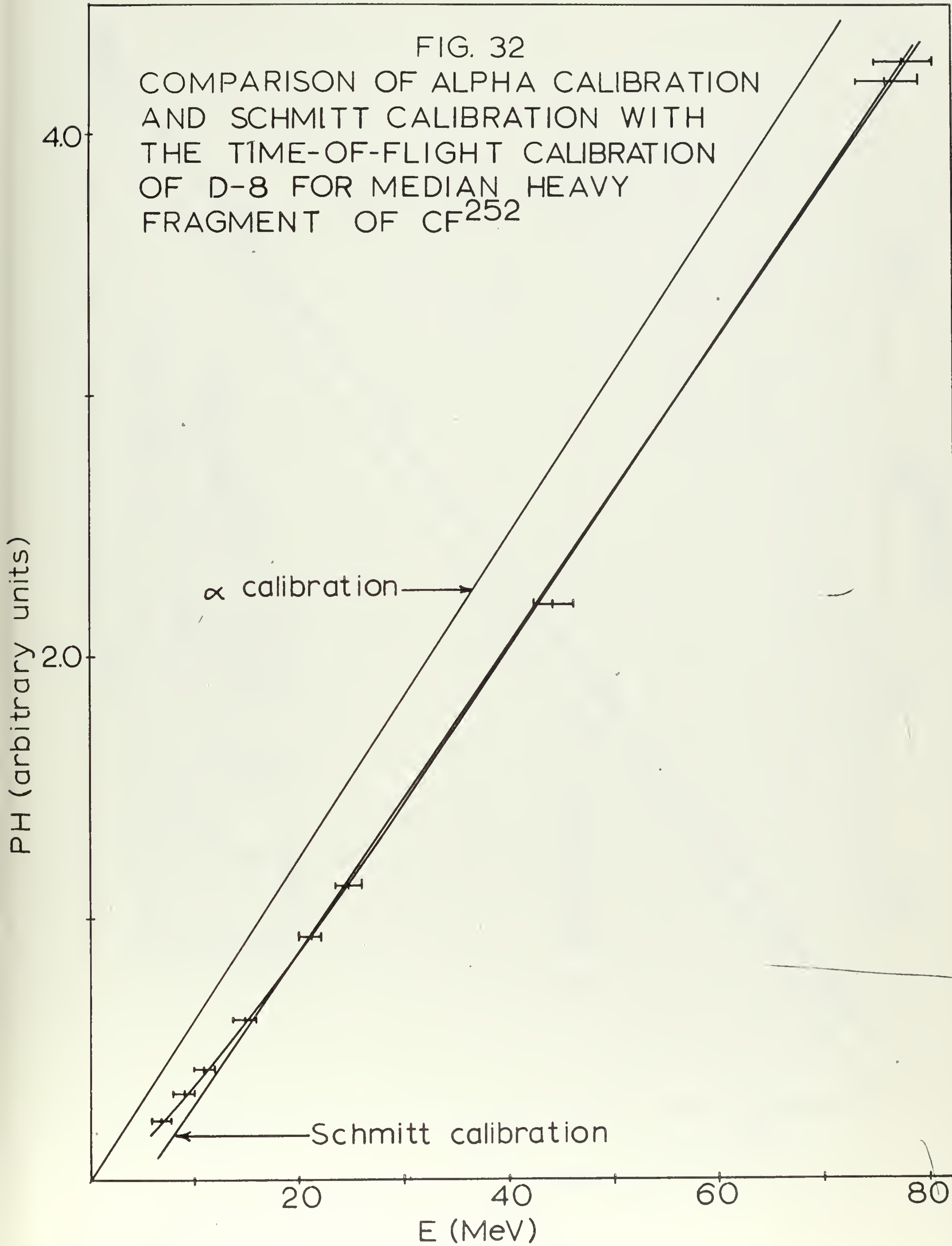
FIG. 32
COMPARISON OF ALPHA CALIBRATION
AND SCHMITT CALIBRATION WITH
THE TIME-OF-FLIGHT CALIBRATION
OF D-8 FOR MEDIAN HEAVY
FRAGMENT OF CF252
α calibration
Schmitt calibration
PH (arbitrary units)
4.0
2.0
E (MeV)
20
40
60
80

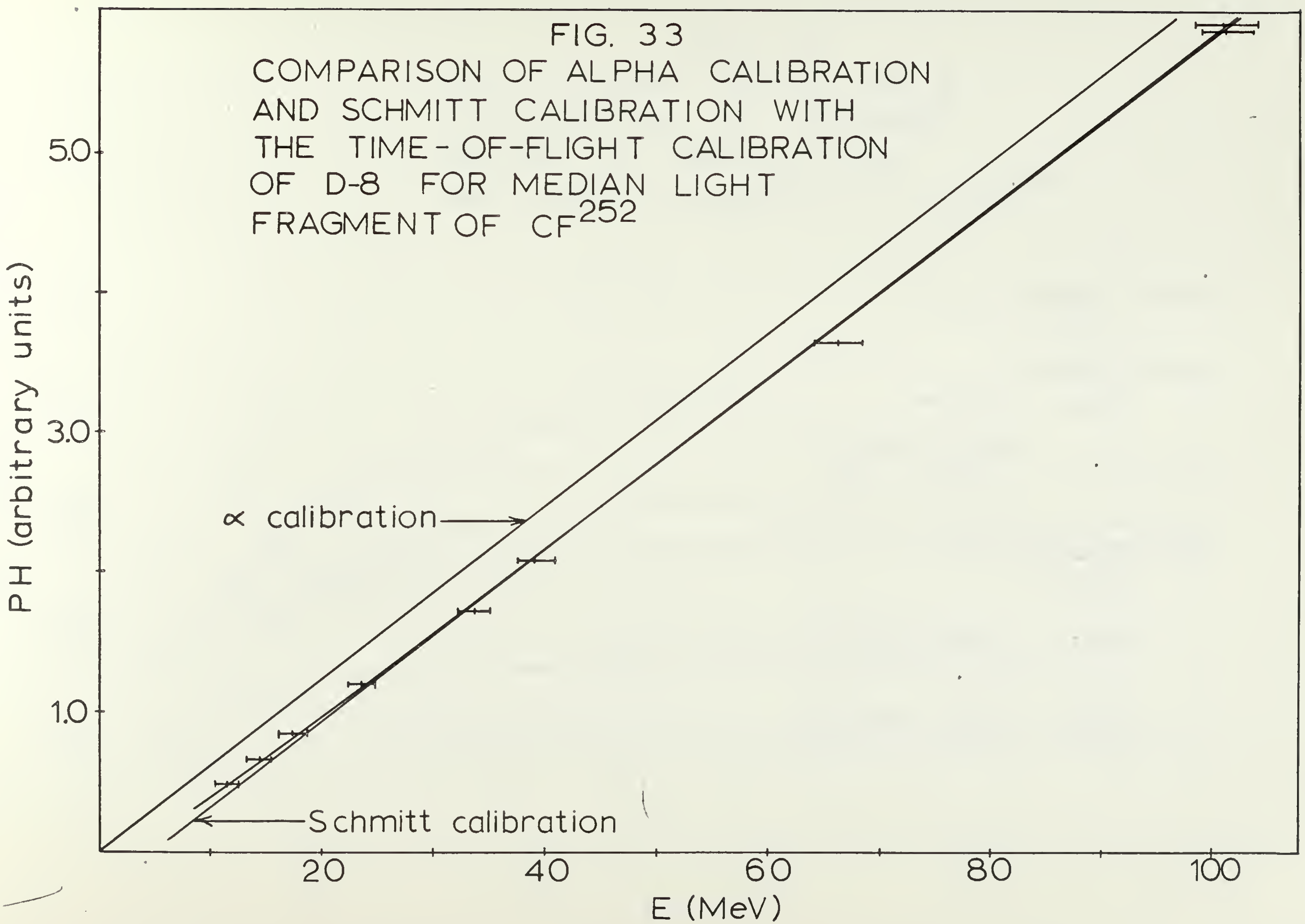

FIG. 33

COMPARISON OF ALPHA CALIBRATION AND SCHMITT CALIBRATION WITH THE TIME-OF-FLIGHT CALIBRATION OF D-8 FOR MEDIAN LIGHT FRAGMENT OF CF^{252}

FIG. 34

PULSE HEIGHT DEFECT AS A FUNCTION OF THE AVERAGE ENERGY OF MEDIAN HEAVY AND LIGHT FRAGMENTS OF CF^{252}

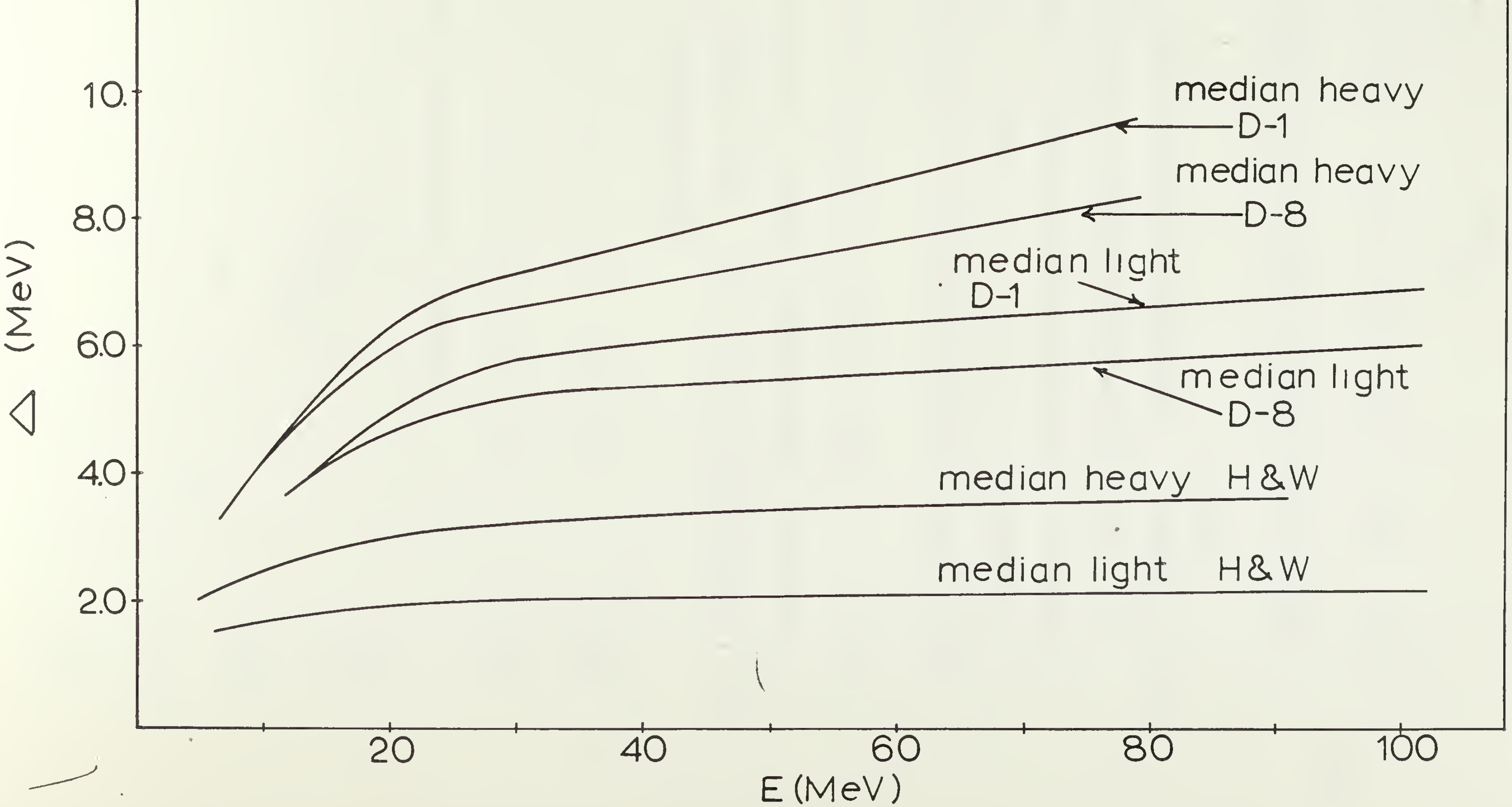

$$f(X) = B_1 \qquad X \leq B_5$$

$$\begin{aligned} f(X) &= B_1 + B_2(X - B_5) + B_3(X - B_5)^2 + B_4(X - B_5)^3 \\ &\quad + B_6(X - B_5)^4 + B_7(X - B_5)^6 + B_8(X - B_5)^8 \qquad X > B_5 \end{aligned} \tag{52}$$

All the B_i's were variable parameters. A typical fit is shown in Figure 35. Having obtained the B_i's, the maximum point of the curve was calculated by setting $f'(X) = 0$ and solving for X. This was accomplished by several iterations of the Newton-Raphson formula (M6).

$$X_o' = X_o - f'(X_o)/ f''(X_o) \tag{53}$$

X_o was the value of X which maximizes the function f(X) defined in equation (52). The 10% and 90% points of the curve were calculated next

$$A_1 = 0.1\ (f\ (X_o) - B_1) + B_1 \tag{54}$$

$$A_2 = 0.9\ (f\ (X_o) - B_1) + B_1 \tag{55}$$

X_1 and X_2 were obtained by iteration

$$X_1' = X_1 - \frac{f\ (X_1) - A_1}{f'(X_1)} \tag{56}$$

$$X_2' = X_2 - (f\ (X_2) - A_2)/ f'\ (X_2) \tag{57}$$

Finally the distance between the 10% and 90% points was calculated

$$\Delta X = X_2 - X_1 \tag{58}$$

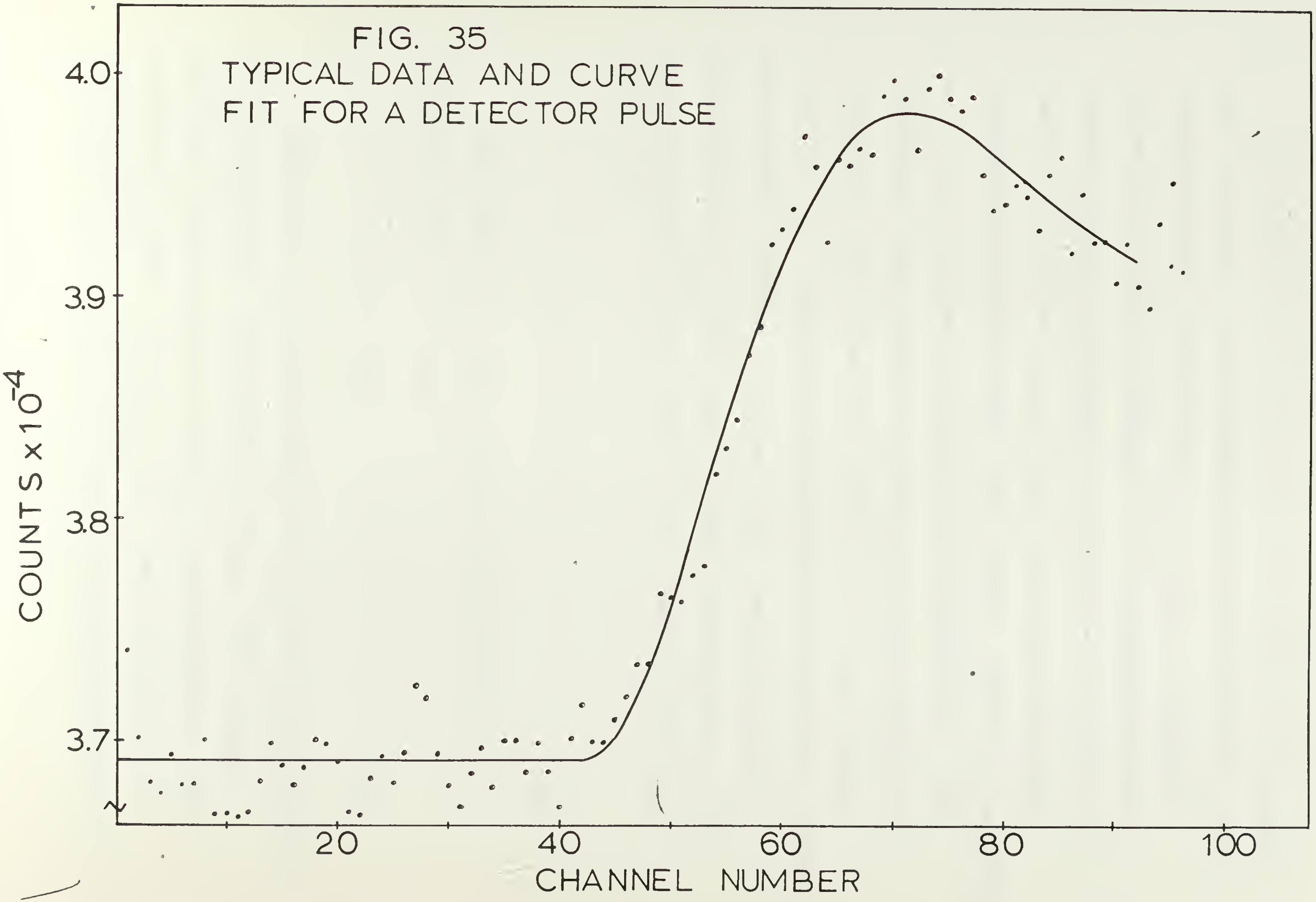

FIG. 35
TYPICAL DATA AND CURVE FIT FOR A DETECTOR PULSE

To convert ΔX to time, the time scale of the system was determined i nanoseconds per channel from the pulser observations at different delay settings. A typical pulser run is shown in Figure 36. The midpoint of the leading edge was calculated by separately averaging the counts in the base line and the flat top of the pulse and then averaging the two. The channel number corresponding to the midpoint was determined by interpolation. This calculation was carried out for each delay setting of a given series of pulser runs yielding a set of channel numbers (X_i). The time corresponding to each delay setting was known to within a constant from the calibration of the delay box for the time-of-flight observations. The set of points (T_i, X_i) was fit by a linear least square model (B3)

$$X = B \cdot T + C \quad . \tag{59}$$

The value of B thus obtained was employed to calculate the rise time from ΔX.

$$T_r = \Delta X/B. \tag{60}$$

The error in ΔX was estimated from the uncertainties in the curve fit. The fitting program (B5) produced upper and lower bounds on the B_i, corresponding to 95% confidence limits. The upper and lower bounds for B_1, the base line, were used to calculate the uncertainties in

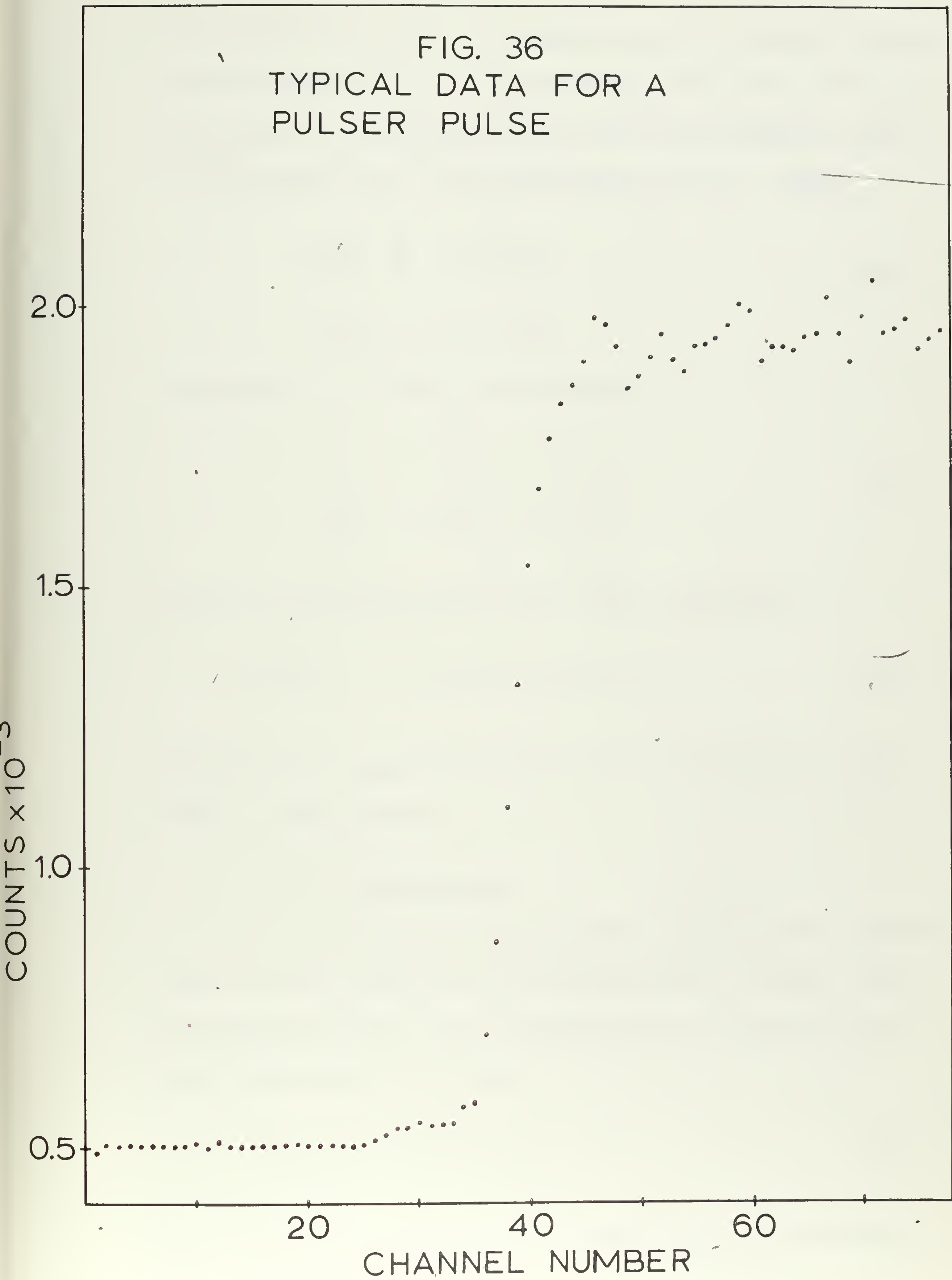
FIG. 36
TYPICAL DATA FOR A
PULSER PULSE
2.0
1.5
1.0
0.5
COUNTS x 10^-3
20
40
60
CHANNEL NUMBER

the values of A_1 and A_2 corresponding to the 10% and 90% points respectively. It was assumed that the error in the value of the maximum point was approximately equal to the error in B_1, and independent of B_1. Thus,

$$\delta A_1 = 0.9\ \delta B_1$$
$$\delta A_2 = 0.9\ \delta B_1 \quad . \tag{61}$$

The error in X_1 and X_2 is given by

$$\delta X_1 = \delta A_1 / f'(X_1)$$
$$\delta X_2 = \delta A_2 / f'(X_2) \tag{62}$$

Finally the uncertainty in $\triangle X$ was calculated.

$$\delta(\triangle X) = \left[\delta X_1^2 + \delta X_2^2 \right]^{\frac{1}{2}} \tag{63}$$

Generally the uncertainty was about $\pm$ 10% but in some cases it was greater.

2. Calculations

The calculation of the plasma time from the observed rise time was similar to the calculation of Meyer (M5). It was assumed that all contributions to the rise time were independent, yielding

$$t_m^2 = t_{RC}^2 + t_A^2 + t_P^2 \tag{64}$$

where t_m is the observed rise time; t_{RC} is the RC time

constant of the detector-amplifier combination; t_A is the rise time of the vertical amplifier of the oscilliscope and t_p is the plasma time. This formula differs from Meyer's (M5) in that there is no separate contribution from the charge collection time. This factor is lumped in with t_p as was done in the theoretical discussion in Appendix A.

Meyer (M5) gives the equivalent circuit time constant as

$$\begin{aligned} t_{RC_{(10-90\%)}} &= 2.2\, R_V\, (C_V + C_s) \\ R_V &= \rho/A\,(T - d) \\ C_V &= C_B \left(\frac{d}{T - d}\right) \\ C_s &= C_B C_A / (C_B + C_A) \end{aligned} \qquad (65)$$

C_A is the input capacity of the oscilliscope; R_V and C_V are the resistance and capacitance of the undepleted detector material and C_B is the capacitance of the depletion region. T, the thickness of the silicon slice; A, the area and ρ, the resistivity were obtained from the detector manufacturer. C_B and d were obtained from a monograph (B4) as a function of bias voltage. C_A = 7pf, from the manufacturer's specifications. The manufacturer also gave the rise time of the vertical amplifier, $t_{A\,(10\,-\,90)}$ = 0.35 nanosec. t_{RC} was calculated from equation (65) and combined with t_A in equation (64) to

give the minimum rise time as a function of bias voltage

$$t_{min} = \left[t_m^2 - t_P^2\right]^{\frac{1}{2}} = \left[t_{RC}^2 + t_A^2\right]^{\frac{1}{2}} \tag{66}$$

These calculations are summarized in Table XI for detectors D-9 and D-10.

Finally the plasma time was calculated from the observed rise time by transposing equation (66) to give

$$t_P = \left[t_m^2 - t_{min}^2\right]^{\frac{1}{2}} \tag{67}$$

3. Results

The results of the rise time measurements as a function of energy and bias voltage are given in Tables XII and XIII for detectors D-9 and D-10 respectively. The observed rise times for D-9 and D-10 are plotted in Figures 37 and 38. The calculated plasma times are plotted for D-9 in Figures 39 - 41 and for D-10 in Figures 42 -44. Straight lines of slope 1/2 and 1/3 have been drawn through each set of points.

The results of the coincidence measurements with detector D-9 are given in Table XIV and the observed rise times plotted in Figure 45. These observations were made at a bias of 250 volts. Figure 46 shows the dependence of the calculated plasma times upon the applied field. For

undegraded fission fragments, based on the data taken without coincidence requirements.

TABLE XI

Summary of the Calculation of T_{min} as a Function of Bias for Detectors D-9 and D-10

V (volts)	d (microns)	C_B (pf)	C_V (pf)	C_S (pf)	R_U (kilohm)	t_{RC} (nanosec)	$T^2{}_{min}$ (nanosec)
		D-9	= 660 ohm-cm				
25	64	170	24.5	6.74	293	2.01	4.92
49.4	90	120	25.8	6.60	276	1.97	4.75
73.6	110	96	26.5	6.52	262	1.90	4.48
122.8	140	75	28.6	6.41	243	1.87	4.37
171.8	170	64	32.2	6.31	223	1.86	4.33
221.1	190	55	32.9	6.21	210	1.81	4.15
		D-10	= 900 ohm-cm				
28.2	80	137	25.6	6.66	386	2.74	8.38
52.1	108	100	27.0	6.55	360	2.65	7.90
77.2	130	82	28.2	6.44	340	2.59	7.57
126.7	169	64	31.0	6.31	305	2.50	7.12
176.0	198	54	34.5	6.19	279	2.50	7.12
225.1	221	48	36.9	6.10	258	2.44	6.83

TABLE XII

Results of Rise Time Observations with Detector D-9

Film	Bias (volts)	T_r (nanosec.)	$\pm$	T_{min}^2 (nanosec)^2	T_p (nanosec)	$\pm$	$\bar{E}$ (MeV)
NF	25	10.34	0.8	4.92	10.1	0.8	89.9
NF	4.94	6.65	0.3	4.75	6.29	0.3	89.9
15-1	25	8.12	0.8	4.92	7.81	0.8	56.9
15-1	4.94	5.95	0.5	4.75	5.54	0.5	56.9
25-1	25	5.44	1.0	4.92	4.97	1.1	33.0
25-1	49.4	5.28	0.8	4.75	4.82	0.9	33.0
NF	73.6	5.13	0.3	4.48	4.68	0.3	89.9
NF	122.8	4.18	0.2	4.37	3.63	0.2	89.9
NF	171.8	3.66	0.1	4.33	3.02	0.1	89.9
NF	221.1	3.41	0.1	4.15	2.74	0.1	89.9
15-1	73.6	4.57	0.4	4.48	3.94	0.5	56.9
15-1	122.8	3.46	0.2	4.37	2.76	0.3	56.9
15-1	171.8	3.29	0.2	4.33	2.55	0.3	56.9
15-1	221.1	3.07	0.2	4.15	2.30	0.3	56.9
25-1	73.6	3.34	0.3	4.48	2.58	0.4	33.0
25-1	122.8	3.12	0.3	4.37	2.32	0.4	33.0
25-1	171.8	2.81	0.2	4.33	1.89	0.3	33.0
25-1	221.1	2.88	0.2	4.15	2.04	0.3	33.0
30-1	73.6	3.32	0.3	4.48	2.56	0.4	27.2
30-1	122.8	3.12	0.3	4.37	2.32	0.4	27.2

TABLE XII continued

Film	Bias (volts)	T_r (nanosec.)	$\pm$	T_{min}^2 (nanosec.)^2	T_p (nanosec.)	$\pm$	$\bar{E}$ MeV
30-1	171.8	2.91	0.3	4.33	2.04	0.4	27.2
30-1	221.1	2.91	0.3	4.15	2.08	0.4	27.2
30-1	25	4.86	0.9	4.92	4.33	1.0	27.2
30-1	49.4	3.86	0.5	4.75	3.19	0.6	27.2
35-1	73.6	3.48	0.4	4.48	2.76	0.5	20.0
35-1	122.8	2.77	0.3	4.37	1.82	0.5	20.0
35-1	171.8	2.86	0.2	4.33	1.97	0.3	20.0
35-1	221.1	2.53	0.2	4.15	1.51	0.4	20.0
35-1	49.4	3.16	0.4	4.75	2.29	0.6	20.0
40-1	73.6	2.50	0.4	4.48	1.33	0.8	13.6
40-1	122.8	2.78	0.4	4.37	1.84	0.6	13.6
40-1	171.8	2.81	0.4	4.33	1.89	0.6	13.6
40-1	221.1	2.45	0.3	4.15	1.36	0.6	13.6
NF	73.6	5.41	0.3	4.48	4.99	0.3	89.9
NF	122.8	4.29	0.2	4.37	3.75	0.2	89.9
NF	171.8	3.82	0.2	4.33	3.21	0.2	89.9
NF	221.1	3.36	0.2	4.15	2.68	0.3	89.9
15-1	221.1	3.19	0.1	4.15	2.45	0.1	56.9
25-1	221.1	2.88	0.2	4.15	2.04	0.3	33.0
30-1	221.1	2.94	0.2	4.15	2.12	0.3	27.2
35-1	221.1	2.47	0.2	4.15	1.395	0.4	20.0
NF	221.1	3.44	0.1	4.15	2.75	0.1	89.9

TABLE XIII

Results of Rise Time Observations with Detector D-10

Film	Bias (volts)	T_r (nanosec.)	±	T_{min}^2 (nanosec.)^2	T_P (nanosec.)	±	$\bar{E}$ (MeV)
NF	77.2	5.50	0.3	7.57	4.76	0.3	89.9
NF	126.7	4.12	0.2	7.12	3.14	0.3	89.9
NF	176.0	3.81	0.2	7.12	2.72	0.3	89.9
NF	225.1	3.55	0.2	6.83	2.40	0.3	89.9
15-1	77.2	4.16	0.3	7.57	3.12	0.4	56.9
15-1	126.7	3.66	0.3	7.12	2.51	0.4	56.9
15-1	176.0	3.47	0.2	7.12	2.22	0.3	56.9
15-1	225.1	3.27	0.2	6.83	1.96	0.3	56.9
25-1	77.2	3.36	0.4	7.57	1.93	0.7	33.0
25-1	126.7	3.16	0.3	7.12	1.69	0.6	33.0
25-1	176.0	2.86	0.2	7.12	1.04	0.5	33.0
25-1	225.1	3.13	0.3	6.83	1.73	0.5	33.0
30-1	77.2	2.98	0.3	7.57	1.14	0.7	27.2
30-1	126.7	2.79	0.3	7.12	0.82	1.2	27.2
30-1	176.0	3.27	0.3	7.12	1.89	0.5	27.2
30-1	225.1	2.83	0.2	6.83	1.08	0.4	27.2
35-1	77.2	2.87	0.4	7.57	0.82	1.3	20.0
35-1	126.7	2.86	0.3	7.12	1.03	0.9	20.0
35-1	176.0	2.98	0.3	7.12	1.36	0.6	20.0
35-1	225.1	2.74	0.4	6.83	0.82	1.0	20.0
40-1	77.2	2.89	0.3	7.57	0.88	0.9	13.6

TABLE XIII continued

Film	Bias (volts)	T_r (nanosec.)	$\pm$	T_{min}^2 (nanosec.)^2	T_P (nanosec.)	$\pm$	$\bar{E}$ (MeV)
40-1	126.7	2.67	0.4	7.12	-		13.6
40-1	176.0	2.69	0.4	7.12	-		13.6
40-1	225.1	2.89	0.4	6.83	1.24	0.8	13.6
40-1	28.2	3.95	0.6	8.38	2.69	0.9	13.6
40-1	52.1	2.90	0.5	7.90	0.72		13.6
NF	77.2	5.81	0.3	7.57	5.22	0.3	89.9
NF	126.7	4.43	0.2	7.12	3.54	0.3	89.9
NF	176.0	4.10	0.2	7.12	3.11	0.3	89.9
NF	225.1	3.78	0.1	6.83	2.73	0.1	89.9
NF	28.2	9.84	0.5	8.38	9.40	0.6	89.9
NF	52.1	6.48	0.3	7.90	5.85	0.3	89.9
15-1	28.2	7.90	0.5	8.38	7.36	0.5	56.9
15-1	52.1	5.85	0.4	7.90	5.14	0.5	56.9
25-1	28.2	5.86	1.1	8.38	5.09	1.2	33.0
25-1	52.1	4.06	0.6	7.90	2.93	0.8	33.0
30-1	28.2	6.35	0.7	8.38	5.65	0.8	27.2
30-1	52.1	4.66	0.7	7.90	3.72	0.9	27.2
35-1	28.2	5.86	1.2	8.38	5.09	1.4	20.0
35-1	52.1	4.27	0.8	7.90	3.21	1.1	20.0
NF	225.1	3.73	0.3	6.83	2.66	0.4	89.9
15-1	225.1	3.23	0.3	6.83	1.91	0.5	56.9
25-1	225.1	2.98	0.2	6.83	1.44	0.4	33.0

TABLE XIII continued

Film	Bias (volts)	T_r (nanosec.) $\pm$	T_{min}^2 (nanosec.)^2	T_p (nanosec.) $\pm$	$\bar{E}$ (MeV)
30-1	225.1	2.84 0.4	6.83	1.06 0.9	27.2
40-1	225.1	2.92 0.4	6.83	1.31 0.8	13.6
35-1	225.1	2.90 0.4	6.83	1.26 0.8	20.0

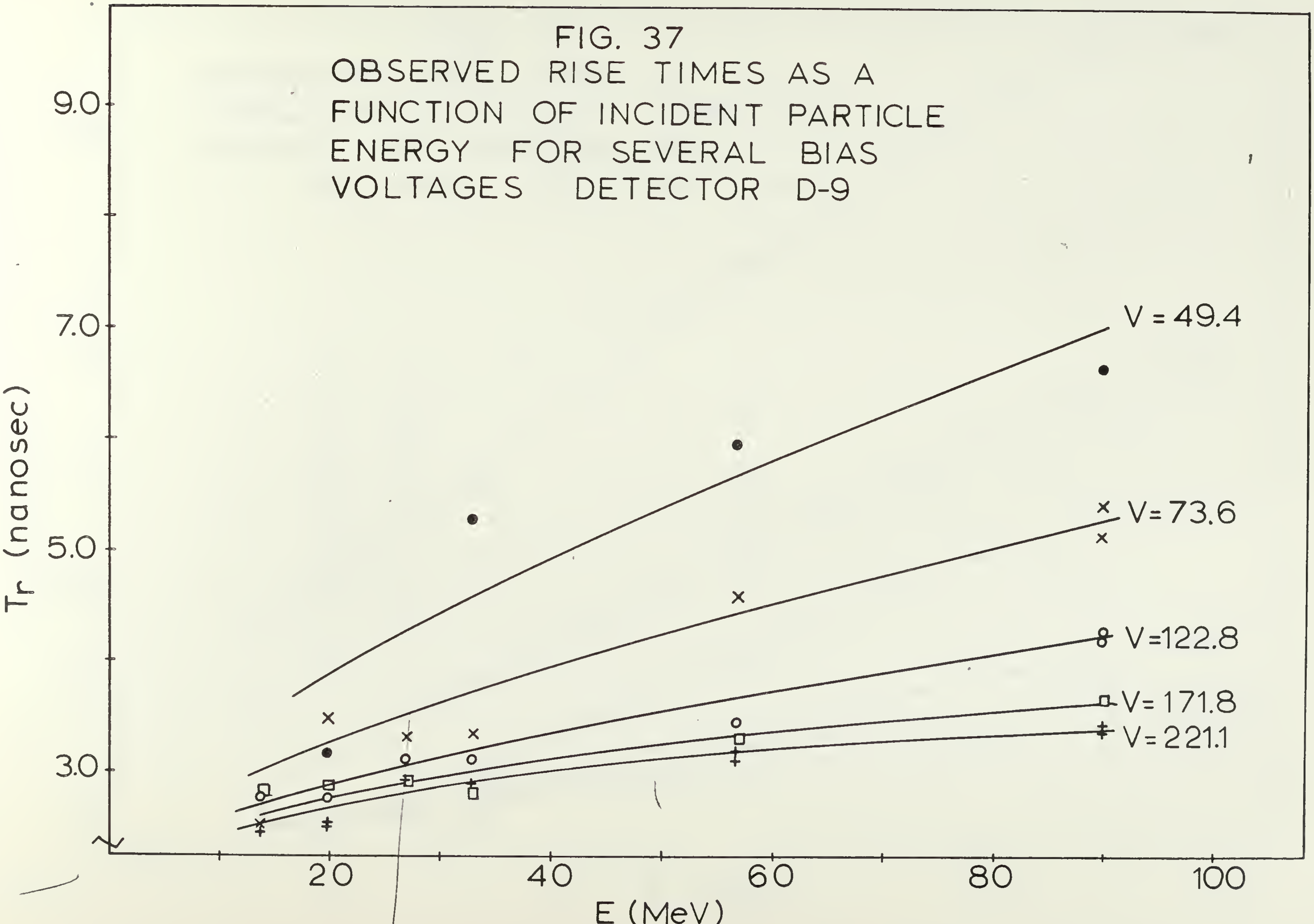

FIG. 37
OBSERVED RISE TIMES AS A FUNCTION OF INCIDENT PARTICLE ENERGY FOR SEVERAL BIAS VOLTAGES DETECTOR D-9

FIG. 38

OBSERVED RISE TIMES AS A FUNCTION OF INCIDENT PARTICLE ENERGY FOR SEVERAL BIAS VOLTAGES DETECTOR D-10

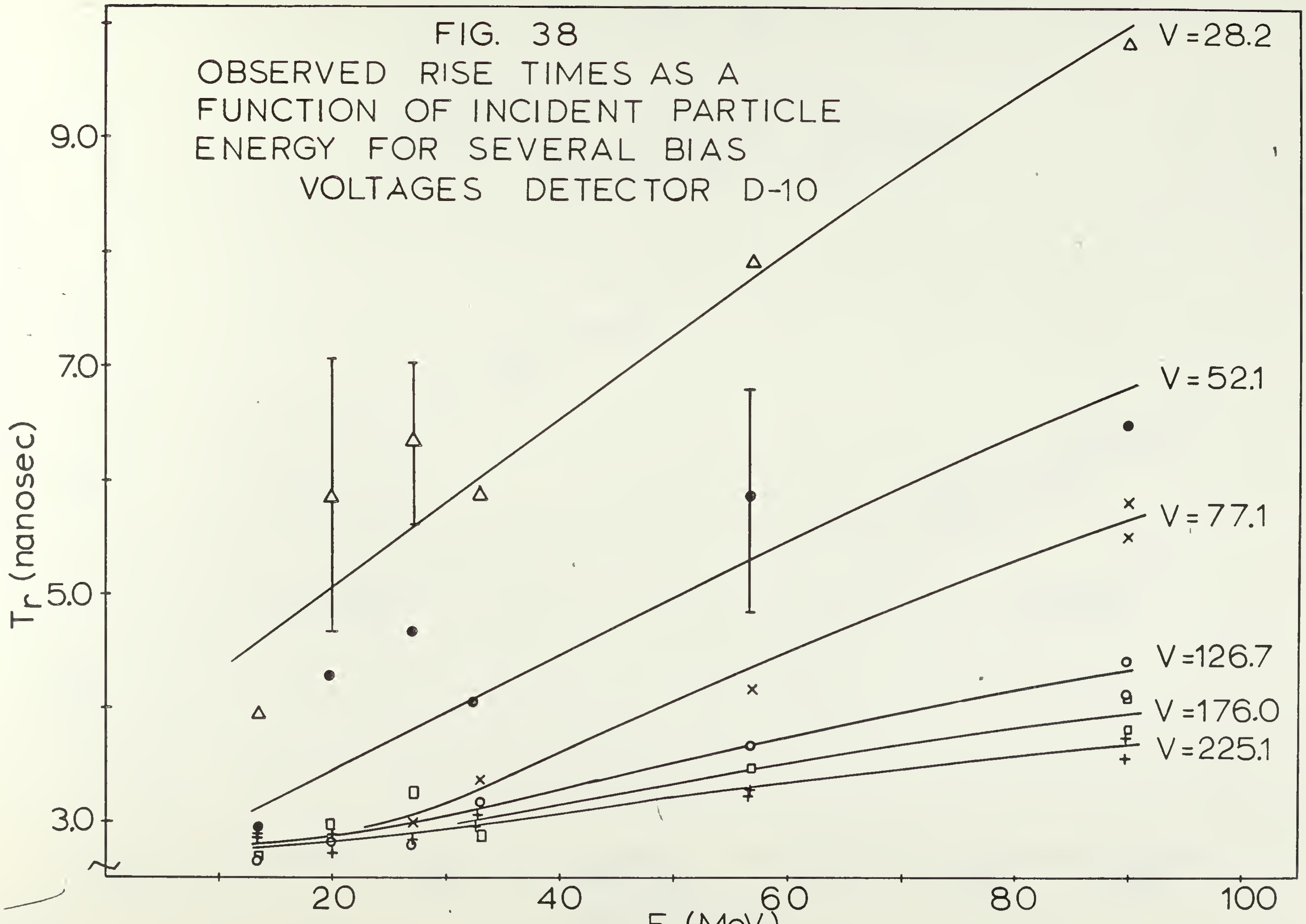

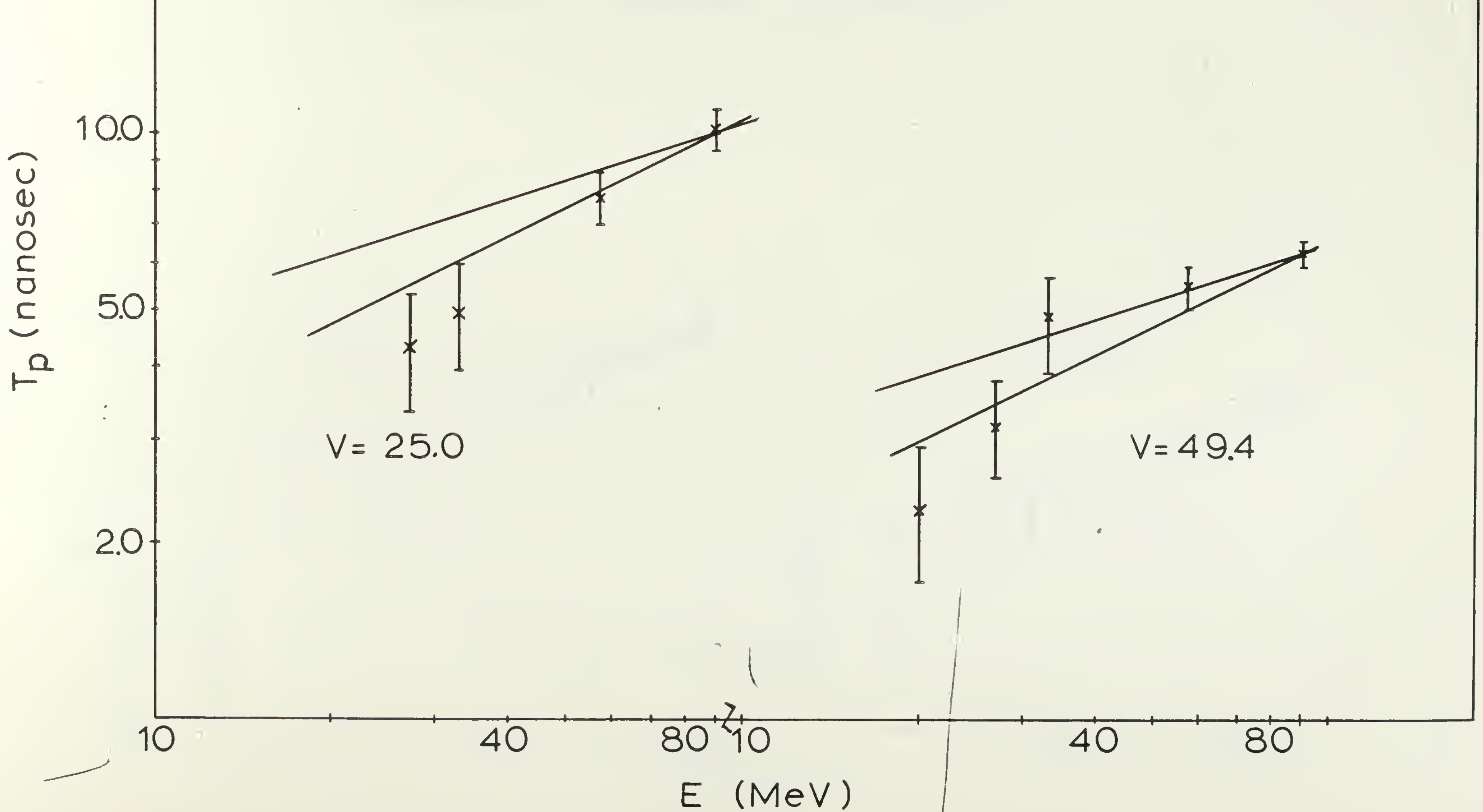

FIG. 39
CALCULATED PLASMA TIME AS
A FUNCTION OF INCIDENT
PARTICLE AVERAGE ENERGY
DETECTOR D-9

FIG. 40
CALCULATED PLASMA TIME AS A FUNCTION OF INCIDENT PARTICLE AVERAGE ENERGY DETECTOR D-9

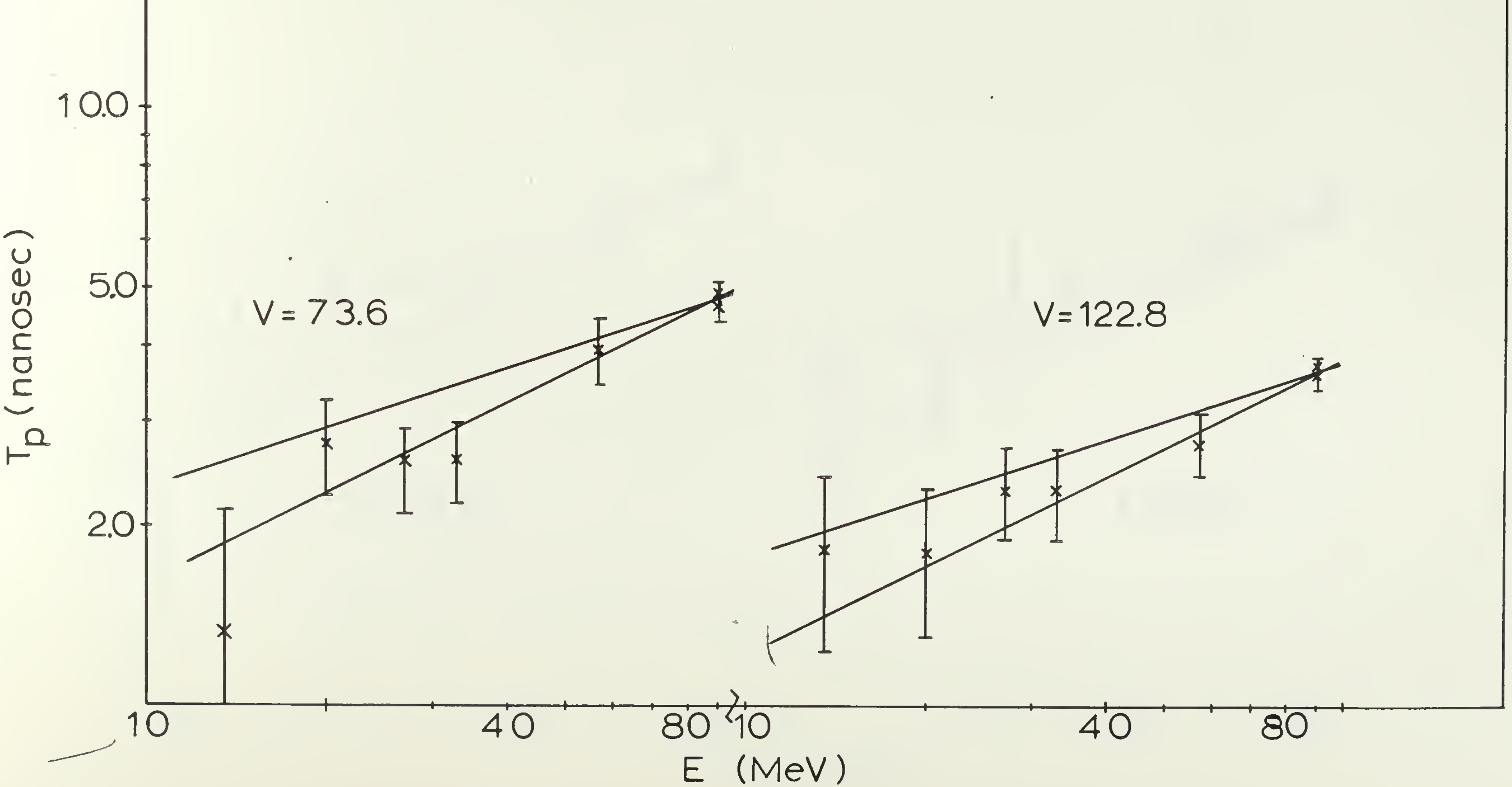

FIG. 41
CALCULATED PLASMA TIME AS A FUNCTION OF INCIDENT PARTICLE AVERAGE ENERGY
DETECTOR D-9

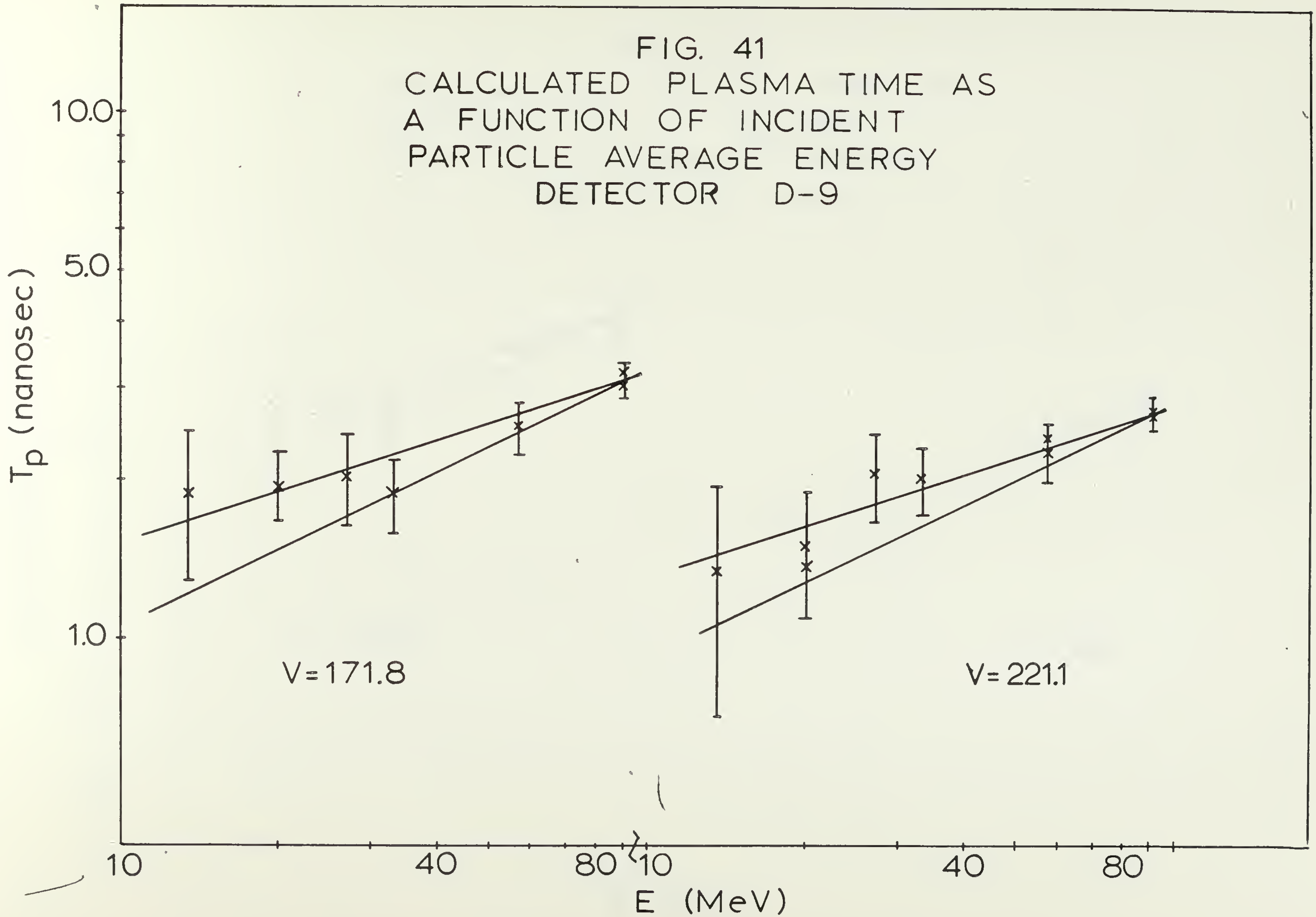

FIG. 42

CALCULATED PLASMA TIME AS A FUNCTION OF INCIDENT PARTICLE AVERAGE ENERGY

DETECTOR D-10

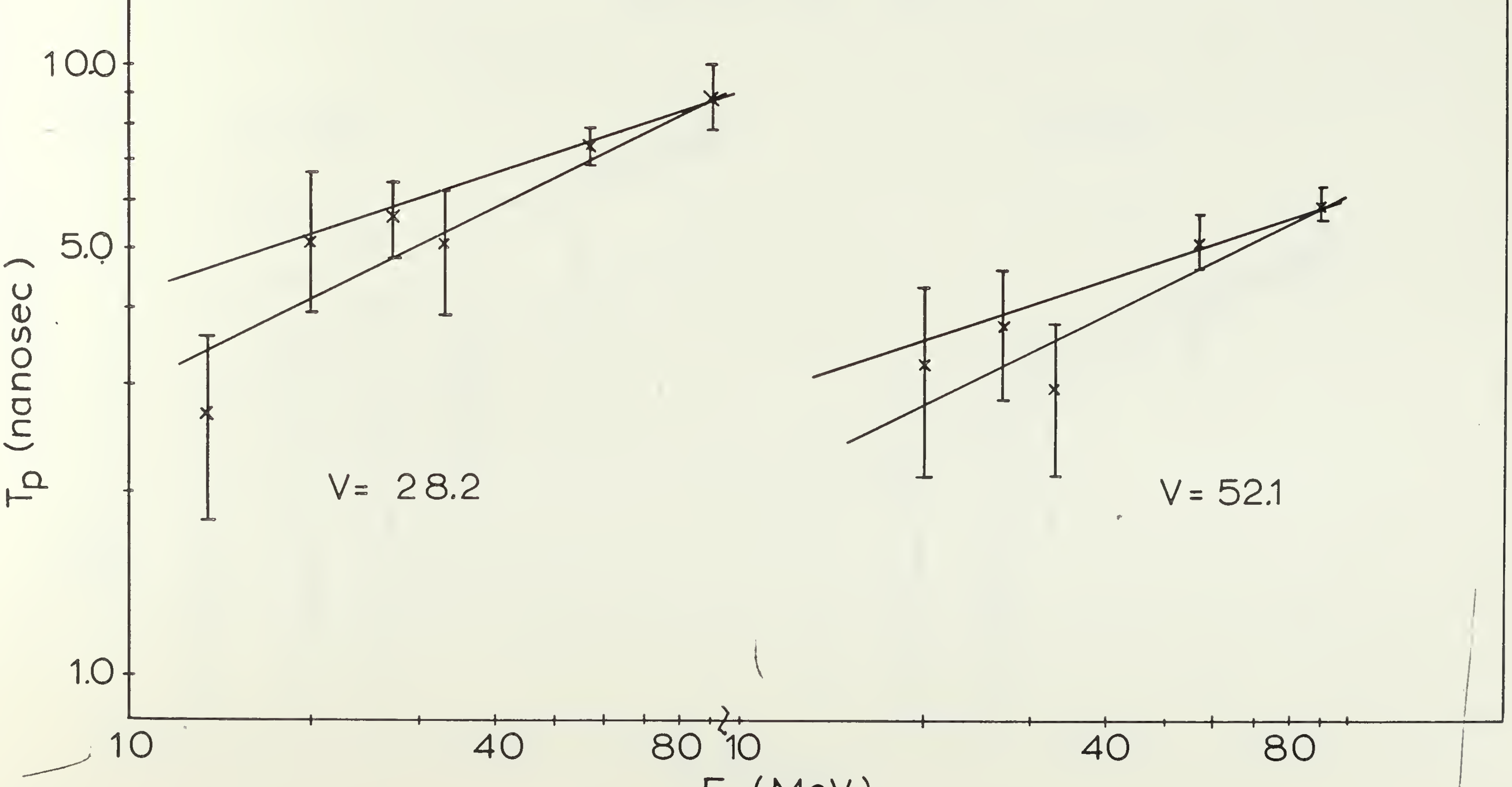

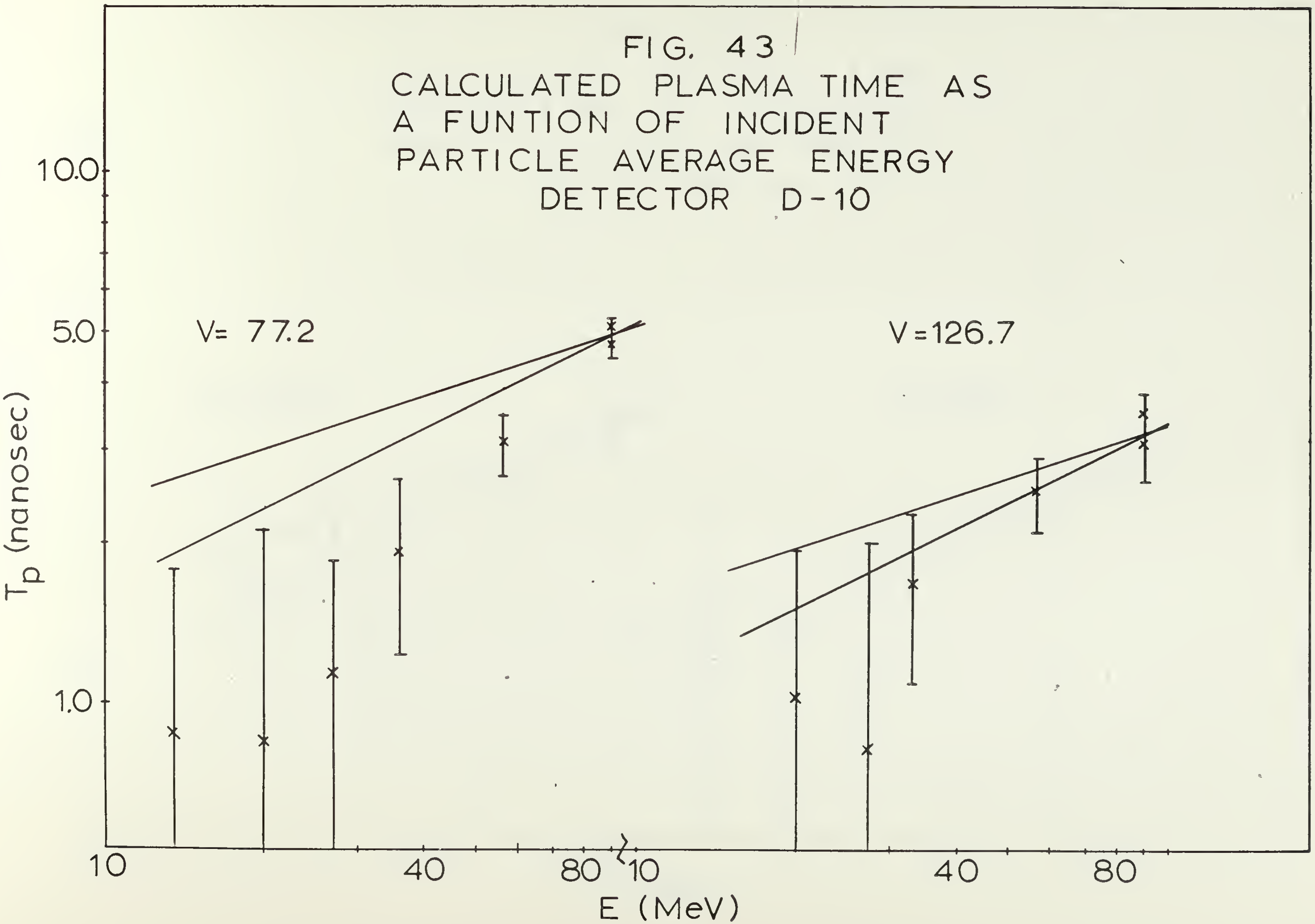

FIG. 43
CALCULATED PLASMA TIME AS A FUNTION OF INCIDENT PARTICLE AVERAGE ENERGY
DETECTOR D-10

FIG. 44

CALCULATED PLASMA TIME AS A FUNCTION OF INCIDENT PARTICLE AVERAGE ENERGY DETECTOR D-10

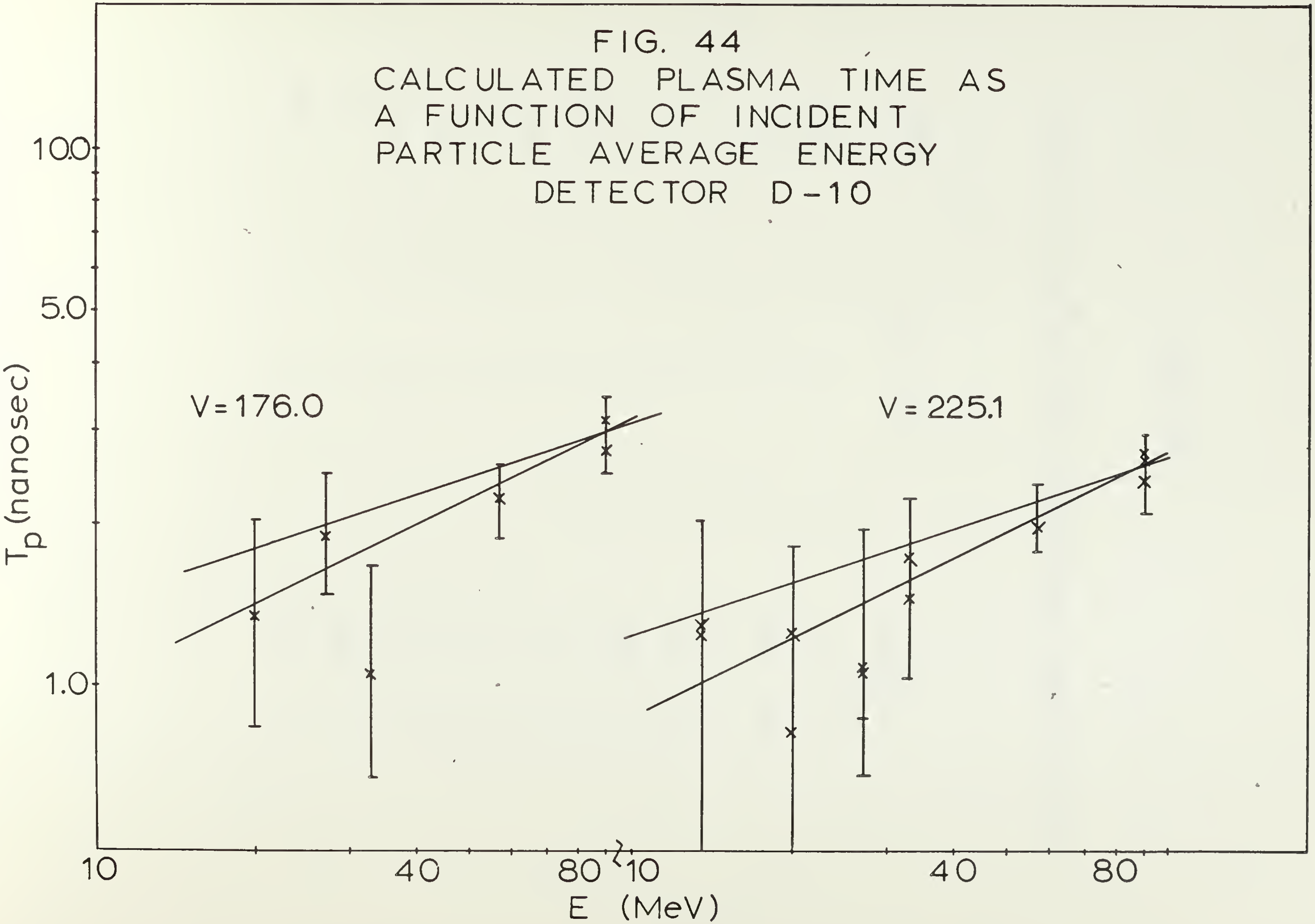

TABLE XIV

Results of the Tise Time Measurements with Coincidence

Film	Frag. Type	T_r (nanosec.)	$\pm$
15-1	L	3.24	0.3
15-1	H	3.44	0.4
25-1	L	2.70	0.4
25-1	H	3.18	0.6
30-1	L	2.88	0.5
30-1	H	1.94	0.5
35-1	L	2.91	0.6
35-1	H	2.54	0.6
40-1	L	2.77	0.9
40-1	H	2.93	0.7
NF	L	3.25	0.3
NF	H	3.20	0.4

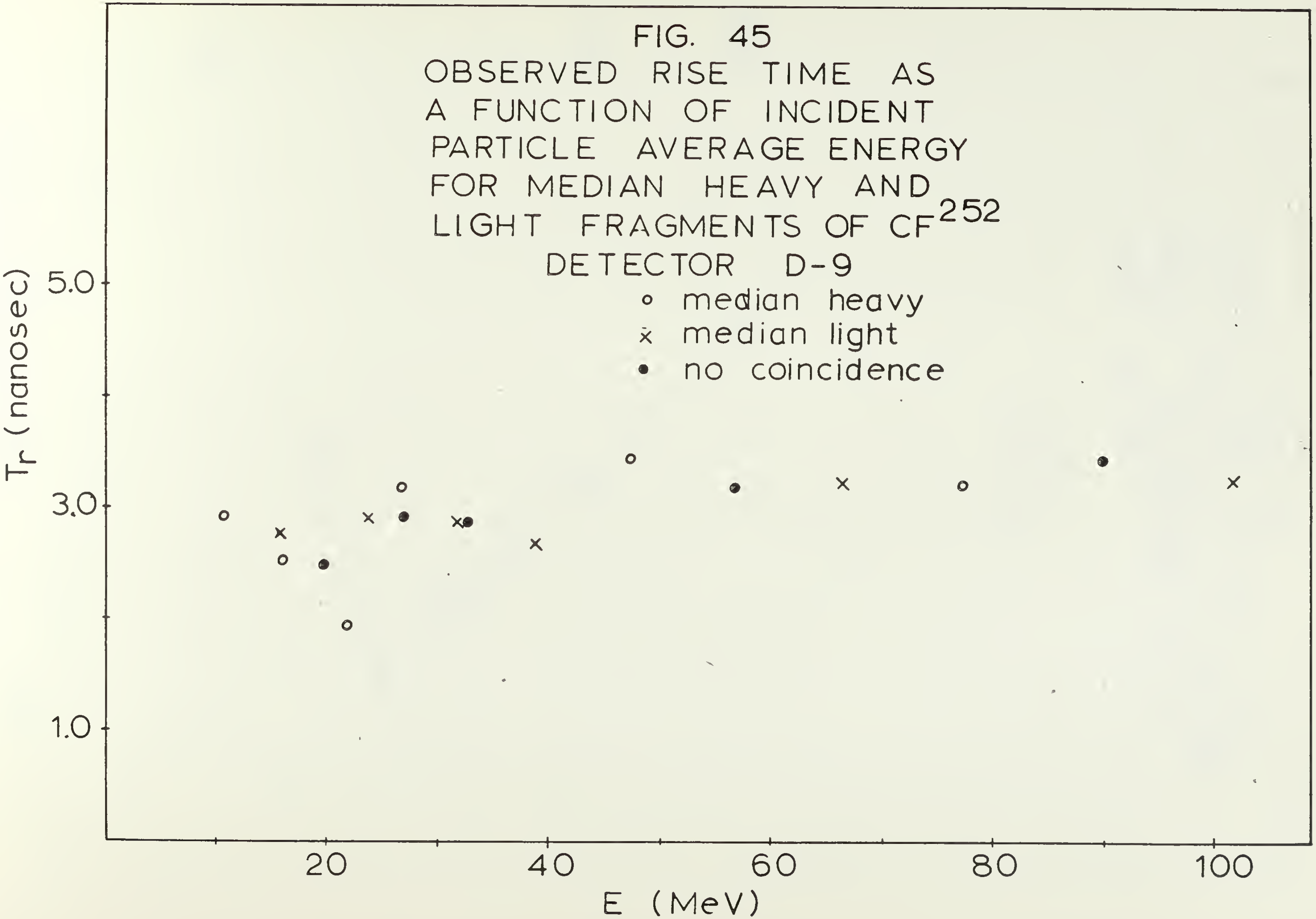

FIG. 45

OBSERVED RISE TIME AS A FUNCTION OF INCIDENT PARTICLE AVERAGE ENERGY FOR MEDIAN HEAVY AND LIGHT FRAGMENTS OF CF^{252}

DETECTOR D-9

FIG. 46
CALCULATED PLASMA TIME AS A FUNCTION OF APPLIED FIELD DETECTORS D-9 AND D-10

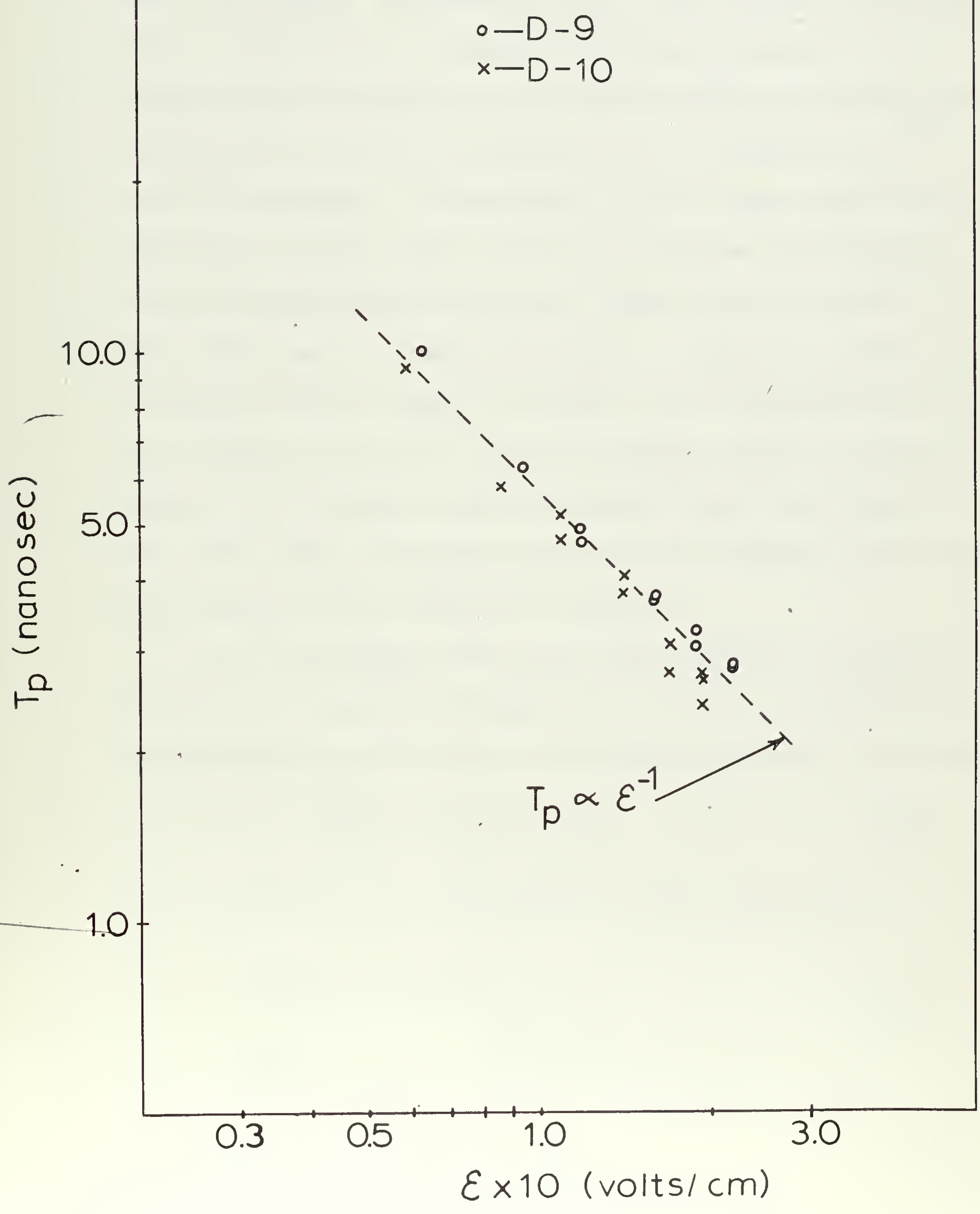

IV. Discussion and Conclusion

A. Pulse Height

Perhaps the most remarkable feature of the calibration curve, Figures 28-33, is the agreement obtained with the Schmitt calibration line. The Schmitt procedure (S3) is based upon a somewhat arbitrary assumption of a linear mass dependence of the pulse height defect and the observation of the two energy peaks of undegraded Cf^{252} fission fragments. Experiment (S3) has shown that such a calibration gives good results at energies encompassed by undegraded fission fragments but until the present work there was no data pertaining to degraded fission fragments and no reason to expect that extrapolation of the Schmitt line (S3) to lower energies would be valid. However, the present experiments show that the Schmitt line (S3) will give good results down to about 25 MeV for both median light and heavy fragments.

At lower energy the curve bends towards the origin as might be expected. This portion of the calibration curve can be represented by an empirical curve of the form

$$\overline{PH} = a_2E^2 + a_1E \qquad (68)$$

The coefficients are determined by the conditions

$$\begin{aligned} PH(E') &= PH(E')_{SCHMITT} \\ \left.\frac{dPH}{dE}\right|_{E = E'} &= \left.\frac{dPH_{SCMITT}}{dE}\right|_{E = E'} \end{aligned} \qquad (69)$$

E' is the energy at which the true calibration curve departs from the Schmitt line. Unfortunately the accuracy of the present experiments does not permit a general determination of E'. It is apparent from the figures that $20 \leq E' \leq 35$ MeV, so possibly a value of E' = 25 MeV will give fair results in the general case. Figures 47 and 48 show the curves calculated with this method along with the data points of the present experiment.

It is impossible to make a detailed quantatative discussion of the pulse height defect as a function of energy (Figure 34) because of the accuracy of the experiments, but some qualatative comments are appropriate.

Figure 34 which is a plot of the defect versus energy shows the same general shape for both detectors. Between undegraded energies and 25 MeV the defect decreases slowly with energy but breaks sharply downward at 25 MeV.

It is reasonable to expect the contribution of non-ionizing nuclear collisions to the defect to decrease very slowly for incident particle energies between the undegraded energy and 25 MeV (H1). Therefore, the major part of the slope of the curves in this region can be attributed to decreasing energy loss in the gold film and decreasing recombination losses. The data of Moak and Brown (M3) indicates that the gold film losses decrease by a factor of about two. Recombination losses, which

FIG. 47
COMPARISON OF EMPIRICAL CALIBRATION CURVE WITH EXPERIMENTAL DATA — D-1

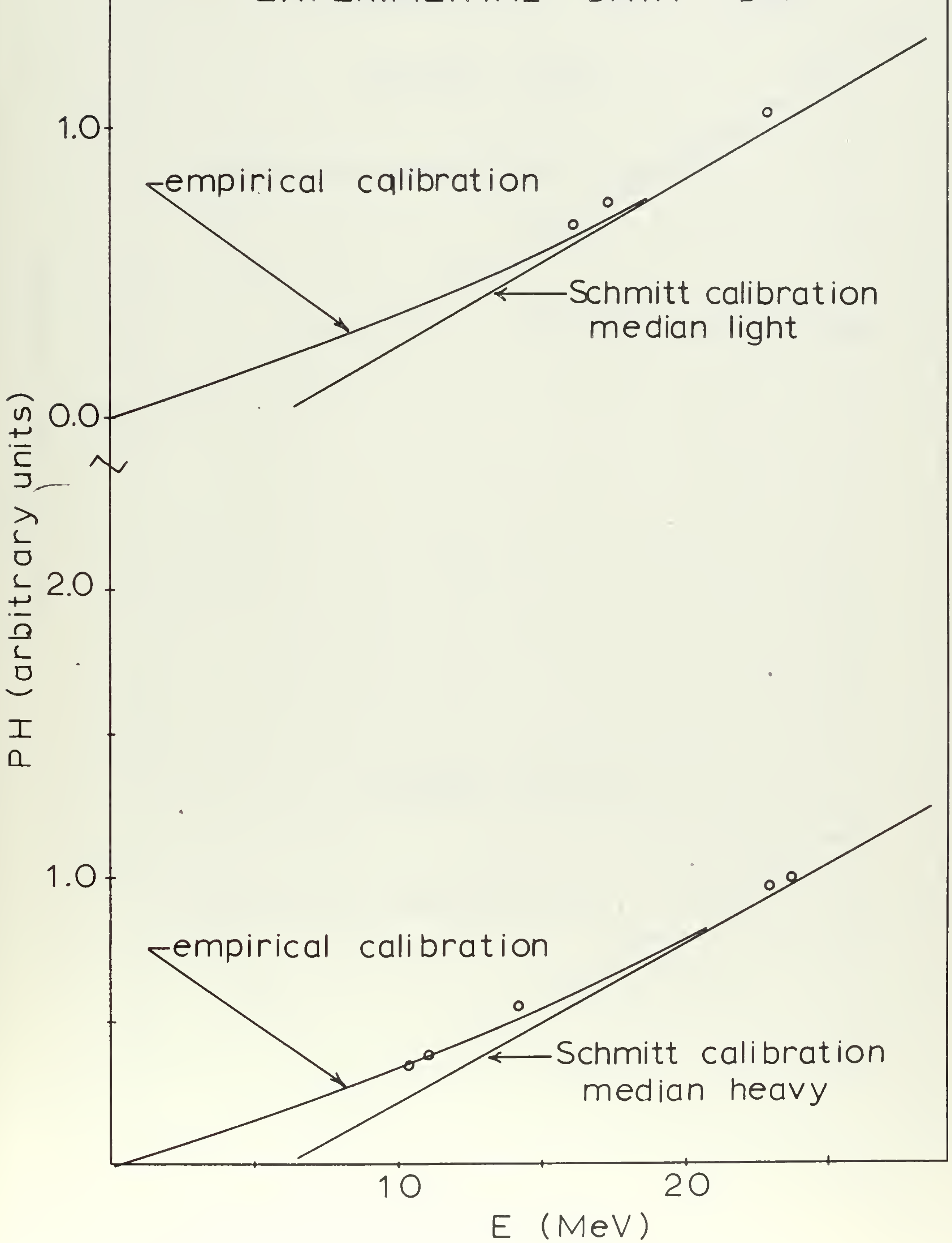

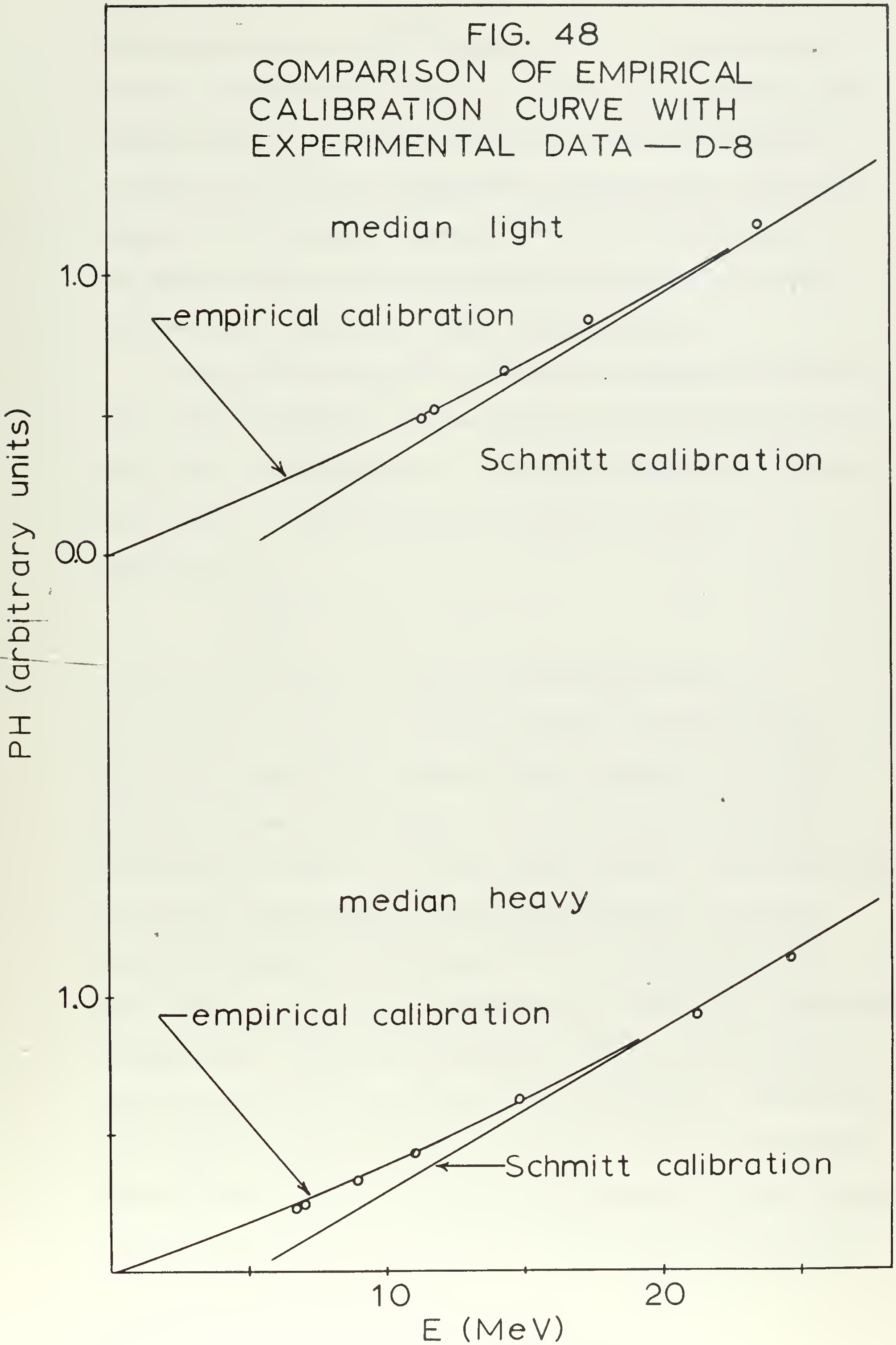

FIG. 48
COMPARISON OF EMPIRICAL CALIBRATION CURVE WITH EXPERIMENTAL DATA — D-8
median light
1.0
empirical calibration
Schmitt calibration
0.0
PH (arbitrary units)
median heavy
1.0
empirical calibration
Schmitt calibration
10
20
E (MeV)

are proportional to $E_o^{\frac{m+1}{m}}$ where $2 \leq m \leq 3$ (see Section IV-B3), decrease by a factor of about six over the same energy range. The gold film losses were estimated to be about 0.5 MeV for undegraded fragments but the total change in the defect above 25 MeV is greater than 0.5 MeV, which argues that decreasing recombination losses are the major source of slope above 25 MeV.

The greater slope for the heavy fragments indicates that these fragments suffer greater recombination losses than the light fragments. Miller and Gibson (M7) give a relation for the fractional carrier loss due to recombination.

$$\frac{\delta n}{n_T} = N_R \, v \, \sigma \, \delta t$$

δn is the change in free carrier density due to recombination; n_T is the free carrier concentration; N_R is the density of recombination centers; V is the carrier thermal velocity; σ is the cross section for recombination and δt is the plasma time. The coincidence rise time measurements (see Section III-B3) indicate that to within 10% the plasma time is independent of mass which argues that recombination losses are independent of mass too. However, the data of Moak and Brown (M3) for bromine and iodine ions imply that dE/dX, the energy loss per unit path length, is greater for an undegraded heavy fragment than dE/dX for an undegraded light fragment. Evidence that this is so is the fact that the valley of

the complete fission fragment spectrum becomes deeper as the fragments are slightly degraded. This means that the heavy fragment deposits more energy near the surface of the detector than a light fragment. According to Miller and Gibson (M7) the density of recombination centers is greatest near the surface of the detector. This fact and the fact that the heavy fragment creates more carriers near the surface than the light fragment results in a greater probability of recombination losses for the heavy fragment over the light fragment.

With regard to the two different detectors, the fact that both curves have the same general shape implies that the marked field dependence of the response of detector D-1 was not related to recombination losses. If the field dependence of the response of D-1 was related to recombination losses then the slope above 25 MeV should be much greater for detector D-1 than for detector D-8. The only alternative explanation for the field dependence in D-1 appears to be that of multiplication.

This notion could be checked experimentally by observing the field dependence of the response of the detectors to degraded fission fragments. One would expect the dependence of D-1 to be about the same while the response of D-8 should show even less dependence on field than the undegraded case.

The possibility was considered that the sharp break in the defect curve at 25 MeV was induced by the apparatus,

since as the limit of sensitivity was approached, the apparatus tended to discriminate against low energy, high mass fission fragments. In particular, the time pickoff unit used to start the time-to-pulse height converter was the limiting factor in extending the curves to lower energy for just this reason. If such discrimination did indeed take place, then the calculation of energy for that particular observation would employ an average mass that was greater than the average mass of the observed particles. Thus the apparent energy would be greater than the true value. An error of this sort would shift the calibration curves away from the alpha line so it cannot be an explanation for the break in the defect curves at 25 MeV.

The break in the curve at 25 MeV is in disagreement with the calculation of Haines and Whitehead (H1) which predicts that the greatest change in the defect takes place below 6 MeV. A second area of disagreement with their calculation is in the magnitude of the defect due to non-ionizing nuclear collisions. This portion of the defect was estimated from Figure 34 by extrapolating the curve between undegraded energy and 25 MeV to zero. This gave a defect of about 6 MeV for the median heavy fragment and about 5 MeV for the median light fragment. These values may be compared with the values of 3.5 MeV for the median heavy fragment and 2.2 MeV for the median

light fragment predicted by Haines and Whitehead (H1).

One difficulty in determining the magnitude is the accuracy with which the alpha line can be determined. Some authors (S1, K1) have employed only a single alpha source in determining the alpha line. The present experiments employed two different alpha sources which gave an alpha line with an error of ± 0.5 MeV at 100 MeV.

In spite of this inaccuracy and those in the time-of-flight experiments with fission fragments there seems to be a real discrepancy between the present results and the calculations of Haines and Whitehead. It is difficult to point out where the discrepancy arises since the details of the Lindhard theory are unpublished. It should be noted, however, that this is not the first discrepancy to be observed for heavy ions (M1, M3).

B. Rise Time

The plots of observed, rise time versus energy for various bias voltages (see Figure 45) show a definite dependence on both energy and bias voltage. The calculated plasma times are proportional to $E_o^{\frac{1}{m}}$ where $2 \leq m \leq 3$ with only one or two exceptions which are probably due to experimental error.

The value of $m = 2$ is in agreement with the diffusion model presented in Appendix A which gives

$$t_p = \left[\frac{2e\, t_t\, E_o}{\pi w D t \epsilon \mathcal{E}} \right]^{\frac{1}{2}} \qquad (70)$$

Additional evidence that $t_p \sim E^{\frac{1}{2}}$ comes from the experiments of Meyer (M5) with fission fragments and alpha particles from Cf^{252}. He reported that $(t_p)_{FF}/t_{p_\alpha} = 4 \pm 1$ for each detector tested. Substituting $\bar{E}_{FF} = 89.9$ MeV and $E_\alpha = 6.11$ MeV into equation (70) gives $(t_p)_{FF}/t_{p_\alpha} = 3.82$.

However, with values of $E_o = 90 \times 10^6$ eV, $t_t = 0.5 \times 10^{-9}$ sec., $e = 1.6 \times 10^{-19}$ coul., $w = 3.6$ eV/I.P., $\epsilon = (12)\ (8.85 \times 10^{-14})$ f/cm., $\mathcal{E} = 10^4$ V/cm. and $D = 30$ cm^2/sec. one obtains $t_p = 6 \times 10^{-8}$ seconds, indicating that diffusion alone is too slow a process to account for the observed plasma time.

In fact, the field dependence of equation (70) does not agree with experiment. The present experiments indicate that $t_p \sim \mathcal{E}^{-1}$.

This field dependence of t_p is stronger than that given by equation (70) so probably the effect of field erosion along the lateral surface of the ionization column should be included.

Case III of the Appendix A takes into account possible field erosion and gives

$$t_p = \left[\frac{3e \quad t_t \quad E_o}{\gamma^2 \mu^2 \epsilon\, w}\right]^{1/3} \frac{1}{\mathcal{E}} \quad . \tag{71}$$

This agrees remarkably well with experiment. The field dependence is correct and the dependence of $E_o^{1/3}$ falls within the limits of the observations. For $\gamma = 0.01$

and typical values for the other parameters, $t_p = 6 \times 10^{-8}$ sec. Larger values of γ would naturally reduce t_p.

Probably both diffusion and field erosion contribute to the spreading of the column. This can be considered as field enhanced diffusion with the field removing carriers from the fringes of the ionization column, thereby maintaining a sharp concentration gradient at the surface.

The original interest in the plasma time arose from attempts to explain the pulse height defect by recombination losses in the plasma. An estimate can be made of these losses based on the premise that $t_p \propto E_o^{\frac{1}{m}}$ where $2 \leq m \leq 3$. Miller and Gibson (M7) have treated the problem for the undegraded case and came to the conclusion that recombination via recombination centers in the forbidden gap is the most important mechanism. Following these authors the fractional carrier loss can be written as

$$\frac{\delta n}{n_T} = \frac{n\, N_R\, \sigma v}{n_T}\, \delta t \qquad (72)$$

δn is the carrier loss; n the free carrier density; N_R is the density of recombination centers; σ is the recombination cross section; v is the thermal velocity; n_T is the density of carriers created by the charged particle and δt is the plasma time. The energy dependence of the plasma time can be substituted into equation (72) to obtain

$$\frac{\delta n}{n_T} \propto \frac{n}{n_T} E_o^{1/m} \tag{73}$$

Miller and Gibson (M7) have estimated that $n \cong n_T$. Therefore, after converting to energy units one obtains a relation for the pulse height defect due to recombination losses.

$$\Delta_{\text{RECOMBINATION}} \propto E_o^{m+1/m} \qquad 2 \leq m \leq 3 \tag{74}$$

This shows that recombination losses fall off quite rapidly with incident particle energy.

Concerning the rise time measurements with coincidence, it had been hoped that they might reveal any difference between the light and heavy fragments but lack of precision made this impossible as shown in Figure 45. Possibly a lower bias voltage would have proved a more advantageous choice.

Appendix A

A Model for the Plasma Effect

As was discussed in the introduction the plasma effect and in particular the plasma time hold considerable interest because of the possible recombination effects within the plasma.

Initially there is a neutral column of ionization with length equal to the particle range and linear density proportional to the energy loss per unit distance for the particle. Dearnaley and Northrop (D1) made a crude estimate of the plasma time without solving the usual differential equations by assuming that the dispersal of the plasma was a diffusion controlled process. They considered the case where the particle track is perpendicular to the electric field and represented the track as a line of ionization with linear density λ. Their result can be obtained by assuming a parallel plate capacitor with electric field $\mathcal{E} = \sigma/\epsilon$ as a model for the detector. σ is the surface charge density and ϵ is the dielectric constant. Then it is assumed that collection is impeded while the radius, R, of the track increases by diffusion to a point where

$$\frac{e\lambda}{2\pi R} = \sigma = \epsilon\mathcal{E} \qquad (1)$$

and normal field collection proceeds. Characteristically, $R \approx \sqrt{Dt}$ where D is the ambipolar diffusion constant and t is time. Substituting into equation (1) for R and solving for t gives an estimate of the plasma time

$$t_p = \frac{e^2 \lambda^2}{D \epsilon^2 \mathcal{E}^2} \tag{2}$$

The case where the particle track is parallel to the field has never been treated but the same sort of reasoning can be applied with fruitful results. In this case, the electric field sees the end of the column of ionization with cross sectional area $A = \pi R^2$. The amount of charge which falls under the influence of the field is approximately $dN = \frac{\pi R^2 \epsilon \mathcal{E}}{e}$. This charge will be swept out in a time $dt \approx$ transit time, t_t, which leads to an expression for the collection rate.

$$\frac{dN}{dt} = \frac{\pi R^2 \epsilon \mathcal{E}}{e t_t} \tag{3}$$

Miller <u>et al</u> (M1) have shown that the transit time is essentially independent of the field.

$$t_t = 2.2 \rho/\mu \times 10^{-9} \text{ sec} \tag{4}$$

ρ is the resistivity in ohm-cm and μ is the mobility in cm^2/volt-sec. Integration of equation (3) yields

$$N_o = \frac{\epsilon \mathcal{E}}{e t_t} \int_o^{t_p} \pi R^2 dt \tag{5}$$

N_o is related to the incident particle energy E_o, by the relation $N_o = E_o/w$ where w is the energy expended per ion pair formed.

The integral in equation (5) can be evaluated for cases of special interest.

Case I: $R = a$ where a is a constant

$$N_o = \frac{\tau \mathcal{E} \pi a^2}{e t_t} t_P \tag{6}$$

$$t_P = \frac{e t_t E_o}{\pi a^2 w \tau \mathcal{E}} \tag{7}$$

Case II: $R = \sqrt{Dt}$

$$N_o = \frac{\tau \mathcal{E} \pi D t_P^2}{2 e t_t} \tag{8}$$

$$t_P = \left[\frac{2 e t_t E_o}{\pi w D \tau \mathcal{E}} \right]^{\frac{1}{2}} \tag{9}$$

Case III: $R = \gamma \mu \mathcal{E} t$

$$N_o = \frac{\gamma^2 \mu^2 \tau \mathcal{E}^3 t_P^3}{3 e t_t} \tag{10}$$

$$t_P = \left[\frac{3 e t_t E_o}{w \gamma^2 \mu^2 \tau} \right]^{1/3} \frac{1}{\mathcal{E}} \tag{11}$$

Case I corresponds to the case where a, the initial radius of the track is large compared with the change in R due to other effects, i.e. diffusion or field erosion. Case II corresponds to the situation where the initial radius can be neglected and diffusion dominates the spreading of the ionization column. Finally, Case III

represents the possibility that both the initial radius and diffusion may be neglected in comparison with the spreading of the column due to field erosion. Field erosion can be pictured as some small component of the field nibbling at the lateral surface of the ionization column.

Thus far the electric field has not been explicitly defined except with reference to a parallel plate capacitor. The field actually is a function of position across the depletion region. The model may be improved by taking this into account with an "effective field" defined as the average field over the length of the particle track and given by (M5)

$$\mathcal{E} = \frac{V_b}{d} \left[1 - L/d\right] \quad . \tag{12}$$

V_b denotes the bias voltage; d the width of the depletion region and L the length of the particle track.

Brown (B7) has estimated that the mean free path of a secondary electron in silicon is of the order of 0.1 microns, which should be a reasonable estimate of the initial radius of the track. The diffusion constant, $D \approx 30$ cm^2/sec., so over a period of a few nanoseconds diffusion increases the radius by about 2 microns. Based on these estimates it is likely that Case I has no applicability since $\frac{a}{\sqrt{Dt}} << 1$. Values of $\mathcal{E} = 10^4$ V/cm and $\mu = 1350$ cm^2/volt-sec give $\gamma \mathcal{E} \mu t = 1.38\gamma \times 10^{-2}$cm

over a few nanoseconds for Case III. Therefore, for $\gamma > 0.01$ the effect of field erosion is comparable with that of diffusion and must be taken into account.

The present experiments (see Section III-3) show an energy dependence of $t_p \propto E_o^{\frac{1}{m}}$ where $2 \leq m \leq 3$. The observations of Meyer (M5) that $(t_p)_{FF}/t_{p_\alpha} = 4 \pm 1$ are in general agreement with the present experiments for $E_\alpha = 6.11$ MeV and $E_{FF} = 89.9$ MeV. The observations of Meyer also showed the field dependence to be $t_p \propto \mathcal{E}^{-1}$ as given by Case III of the models.

It is difficult to choose between the diffusion model and field erosion model on the basis of the present experiments because of the general lack of precision. However, the evidence indicates that the models do have some validity and that probably both diffusion and field erosion contribute to the dispersal of the ionization column.

BIBLIOGRAPHY

A1. R. C. Axtmann and D. Kedem, Nucl. Instr. Meth., 32, 70-76 (1965).

B1. H. C. Britt and H. E. Wegner, Rev. Sci. Instr., 34, 274 (1963).

B2. H. C. Britt and G. C. Benson, Rev. Sci. Instr., 35, 843 (1964).

B3. K. A. Brownlee, Statistical Theory and Methodology in Science and Engineering, Chap. 11, p. 287 (Wiley and Sons, New York, 1960).

B4. J. L. Blankenship, IRE Trans NS-7, 190 (1960).

B5. T. Baumeister, III and D. W. Marquardt, IBM Share Program No. 1428.

B6 H. A. Bethe and J. Ashkin, Experimental Nuclear Physics, 1, Chap. 2, p. 228 (Segrè, E., Ed., Wiley, New York, 1953).

B7. Brown, W. L., IRE Trans. Nuc. Sci. NS-8, 2 (1961).

D1. G. Dearnaley and D. C. Northrop, Semiconductor Radiation Detectors, Chap. 2, p. 68 (E. and F. N. Spon Ltd., London, 1963).

E1. R. D. Evans, The Atomic Nucleus, Chap. 22, p. 669 (McGraw Hill, New York, 1955).

F1. J. S. Fraser, Phys. Rev. 88, 536 (1952).

F2. H. Flicker, Rev. Sci. Instr. 34, 882 (1963).

G1. L. E. Glendenin and J. P. Unik, Phys. Rev. 140, B1301 (1965).

G2. R. J. Grainger, J. W. Mayer, J. S. Wiggins, S. S. Friedland, Bull. Am. Phys. Soc. 5, 265 (1960).

H1. E. L. Haines and A. B. Whitehead, Rev. Sci. Instr. 37, 190 (1966).

K1. E. Konecny and K. Hetwer, Nuc. Instr. Meth., 36, 61 (1965).

L1. J. Lindhard, M. Scharff and H. E. Schiøtt, Kgl. Danske Videnskab Selskab., Mat-Fys. Medd., 33, No. 10 (1963).

M1. G. L. Miller, W. L. Brown, P. F. Donovan and I. M. Mackintosh, IRE Trans. Nuc. Sci. NS-7, No. 2-3, pp. 185-189 (June-Sept. 1960).

M2. P. M. Mulás and R. C. Axtmann, Phys. Rev. 146

M3. C. D. Moak and M. D. Brown, Phys. Rev. 149, 244 (1966).

M4. J. C. D. Milton and J. S. Fraser, Phys. Rev. 111, 877 (1958).

M5. H. Meyer, IEEE Trans. Nuc. Sci. NS-13, 180 (1966).

M6. H. Margenau and G. M. Murphy, The Mathematics of Physics and Chemistry, Chap. 13, p. 492 (Van Nostrand, New York, 1956).

M7. G. L. Miller and W. M. Gibson, Proceedings of the Conference on Nuclear Electronics, Vienna, 1962, Vol. I., p. 477.

M8. D. W. Marquardt, J. Soc. Indust. Appl. Math. 11, 431 (1963).

M9. C. D. Moak, J. W. T. Dobbs and W. W. Walker, Rev. Sci. Instr. 37, 1131 (1966).

M10. K. G. McKay, K. B. McAfee, Phys. Rev. 91, 1079 (1953).

S1. Shoji Shirata, Japan J. Appl. Phys. 3, 326 (1964).

S2. A. R. Sattler, Phys. Rev. 138, A 1815 (1965).

S3. H. W. Schmitt, W. E. Kiker and C. W. Williams, Phys. Rev. 137, B 837 (1965).

S4. H. W. Schmitt and Frances Pleasonton, Nucl. Instr. Meth. 40, 204-208 (1966).

S5. O. J. Steingraber and I. B. Berlman, Rev. Sci. Instr. 34, 524 (1963).

S6. E. Spenke, Electronic Semiconductors, Chap. VII, p. 248 (McGraw Hill, New York, 1958).

W1. S. L. Whetstone, Phys. Rev. 131, 1232 (1963).

W2. R. L. Williams and P.P. Webb, R.C.A. Review 23, (1962).

W3. F. J. Walter, IEEE Trans. Nucl. Sci. NS-11, No. 3, 232 (1964).